UNIVERSITÁ DEGLI STUDI DI CATANIA
FACOLTÁ DI SCIENZE MATEMATICHE, FISICHE E NATURALI
XXVII CICLO - DOTTORATO DI RICERCA IN FISICA

CRISTINA PUGLIATTI

PARTICLE SCINTILLATING TRACKERS: DESIGN AND READ-OUT OF REAL-TIME, LARGE-AREA, HIGHLY SEGMENTED DETECTORS

PHD THESIS

Tutor:
Chiar.mo Prof. Domenico Lo Presti
Supervisor:
Chiar.mo Prof. Giovanni Valerio Russo
PhD coordinator:
Chiar.mo Prof. Francesco Riggi

A C A D E M I C Y E A R 2 0 1 3 / 2 0 1 4

CONTENTS

INTRODUCTION

The scientific research has been always motivated by two strong reasons: the intrinsic curiosity in human nature to know himself and what surrounds and the desire to improve the quality of life by bridging as much as possible the needs of contemporary society.

Applied physics was born as a consequence of the second motivation. Being inspired by the knowledge of basic physics, it plays a key role in technological innovation and has the ability to apply the same developed technology to more areas of interest.

This PhD thesis aims to show as technological advances and suitable technical solutions make scintillation detectors for charged particles capable of being applied in two research areas completely different, but both of great interest for improving the quality of human life:

(1) Medical diagnostics, in particular before or during a tumour treatment with hadrons (**hadrontherapy**);

(2) Tomography by cosmic ray radiation ([1]**muon tomography**) applied to cargo containers for the identification and localization of potential radioactive substances that are illegally transported.

In the following, the structure of this thesis is illustrated, with the description, the characterization and the possible applications of a particular category of particle detectors of interest for these two research issues: large-area, highly segmented trackers, made of scintillating materials.

The detection principle underlying the functionality of every particle detector is the energy transfer of a crossing particle to the sensitive volume of the device and the conversion of this energy into a detectable electrical signal.

Charged particles lose their energy through electromagnetic collisions with electrons or atomic nuclei that compose the crossed material, causing its excitation or ionization. Instead, neutral particles must first generate intermediate reactions that allow the formation of charged particles that can, in turn, energize or ionize the atoms of the material that characterizes the detector itself.

[1] Muons are elementary particles belonging to the lepton family, which also consists of the electron, the tau and neutrinos particles. A muon is roughly 200 times more massive than an electron ($m_\mu = 105.7\ MeV/c^2$). It has a unitary negative electric charge −1 and a spin ½.

For example, gas detectors are able to directly detect charged particles by gas ionization phenomena and the consequent generation of a proportional electrical signal that is finally measured.

In case of the indirect detection, e.g. by using *scintillators*, the excitation and ionization of the detector atoms contribute to induce electronic transitions with a subsequent emission of light; the latter is successively converted into an electrical signal via electronics devices such as photodiodes and photomultiplier tubes.

Scintillation detectors are widely used in physical research, i.e. high-energy physics, spectroscopy, neutron detection, calorimetry, residual range measurements and Positron Emission Tomography (PET). If the scintillation detector is able to reconstruct the track of the particle, it is classified as scintillation particle tracker.

A *tracker detector* consists of at least two detector of position placed at a certain distance one from the other. In some cases each tracking plane is made of two physical layers, one for each spatial coordinate *X* or *Y*. The track of a particle that crossed a detector can be reconstructed from the measurement of the impact point position in each detection plane. 3D tracks can be reconstructed by using appropriate algorithms performing an off-line or a real-time software analysis.

*In **Chapter 1** an exhaustive description of scintillation detectors for charged particles in general that focuses in more detail on the trackers with large-area and highly segmented is addressed.*

The application fields for *large-area trackers with a high segmentation level* are multiple. For example, they could observe atmospheric showers by measuring coincident events with other detectors of the same type placed at a certain distance each other. Another important application field is in nuclear and particle physics. Indeed, the reaction products from the beams collision, or from a single particle source can be studied.

Considering the total number of readout channels of highly segmented trackers with large area, it could be too much large if the resolution were the one to read all of them individually. In Chapter 1, a *smart read-out channel reduction strategy* is proposed. It is very useful if applied to these types of detectors in order to give up real-time performances. This architecture reduces the number of read-out channels for a segmented linear detector.

In order to reach the required performances of high spatial/angular resolution, the proposed solution is the employment of scintillating trackers, which are an optimal quality/price compromise among the various models of detectors present in the market. Indeed, the relative reduced cost of plastic scintillators respect to other materials (e.g. Silicon, Germanium or Ceramics) and the possibility to modelling different shapes and sizes are of good advice for large-area detectors also to obtain a high segmentation. In particular, by using the scintillating fibers (Sci-Fis) it is possible to curve fibers in order to apply the compression channel technique at an optical level by routing the optical fibers in a suitable way. The described technique permits to achieve real-time performances for the read-out; lately, in the following sections, the properties of the scintillating materials are described in detail.

As mentioned in issue (1), a research field of great interest for *large-area trackers* with a *high segmentation level* is the *medical physics* with the specific following applications:

- Radiography and tomography of human tissues;
- Monitoring and imaging of a clinical beam;
- Positioning of a patient before a hadrontherapy treatment.

Because of the increasingly strong social demand, *hadrontherapy* for the cancer treatment is a research field that grows continuously up. During a cancer treatment, the advantage of employing charged particles such as proton or carbon ions is related to a better control of the amount of released dose compared to conventional radiotherapy, preserving the surrounding healthy organs and tissues. Furthermore, the direct knowledge of the energy loss by a particle that interacts with the tissue provides much more accurate information on the delivered dose than x-ray tomography and therefore allows to check the correct positioning of the patient. Starting from these considerations, the necessity to have a particle tracker able to provide real-time images of the area to be treated is essential.

With this purpose, the *OFFSET (Optical Fiber Folded Scintillating Extended Tracker)* Research Project (INFN, Nation Institute of Nuclear Physics - Italy) started in the year 2010 with the namesake tracker prototype. The aim of the project is to realize a detector for the real-time imaging and tracking of charged particles with high spatial resolution and low complexity to be applied in medical diagnostic, made of *water equivalent material* (this requirement is optimal for disturbing as least as possible a clinical beam).

*In **Chapter 2** of present thesis, the design and characterization of a charged particles tracker, the OFFSET3 detector are described and compared to the characteristics of the previous OFFSET prototype. The detector is suitably designed for medical physics diagnostics.*

After evaluating the good performances of the OFFSET prototype, it was decided to build an operating tracker that could harness the same technological innovations of the previous model. The sensitive areas of both detectors are made of 500 μm squared multi-cladding BCF-12 Sci-Fis provided in pre-glued and pre-aligned ribbons by the manufacturer (Saint-Gobain corporation). The resulting spatial resolution is 500 μm/$\sqrt{12}$ (calculated as for a segmented detector). The main designing difference is related to the number of tracking planes. While OFFSET is made of a single positioning plane X-Y, obtained as a superimposition of two Sci-Fi layers orthogonal to each other, OFFSET3 is a complete charged particle tracker made of two positioning planes X-Y spaced 100 mm. Hence, the latter detector is 2 mm water equivalent thick. In addition, the tracker sensitive area 288x288 mm^2 size, obtained by curving the ribbons (576 fibers each) with the optimal bending radius of about 5 cm is larger than the one of the OFFSET prototype (200x200 mm^2). This characteristic makes OFFSET3 more suitable for medical imaging application such as radiography or tomography. In fact, OFFSET3 could be applied for the characterization of a clinical beam, i.e. the

measurement of the beam specifications, such as uniformity and penumbra. This information is useful for an accurate tumor treatment or for an accurate positioning of the patient before a treatment.

In both detectors the smart read-out strategy introduced in Chapter 1, allowing a considerable reduction in the number of optical channels to be coupled to the photo-sensor is deeply described for the specific cases. The strategy allows to reconstruct the track of a charged particle that crosses the sensitive area of the detector by using a reduced number of read-out channels than other segmented detectors with the same initial number of channels, reducing also costs and complexity. I.e., the OFFSET3 planes are read with the same number of optical channels needed for a single one. The hit event is decoded by measuring the light output in bound coincidence at both edges of each fiber.

Moreover, the modularity and scalability of the associated electronics simplifies the integration of the detector in a treatment chamber for hadrontherapy. The read-out electronics is based on programmable logic FPGA boards achieving real-time acquisition performances (up to 5 MHz sampling rate).

Both the prototype and the tracker can be characterized exploiting different sources, such as cosmic rays, 90Sr and ion beams. The performances have been tested with 60 MeV, 250 MeV proton and 400 MeV/A clinical carbon beams available at the Center for Advanced Nuclear Applications and Hadrontherapy (CATANA) in the *Laboratori Nazionali del Sud* (LNS) in Catania (Italy) and at the *Centro Nazionale di Adroterapia Oncologica* (CNAO) in Pavia (Italy). The corresponding test descriptions and data analysis results are reported in Chapter 2.

The technological know-how acquired with the design, construction and characterization of the *OFFSET3* detector has been of great assistance for the construction of the *Muon Portal Detector (PORTAL).* The latter fits in the topic that was anticipated in issue (2): the muon tomography for the safety transport of goods inside containers.

*In **Chapter 3** the motivations for the Muon Portal Project (2011-2015 Italian national project with several partners, founded by National Operative Programme PON), other possible scanning techniques for security (container inspection) and additional applications of muon tomography are deeply described.*

At first, an introduction of the problem is necessary in order to understand in which way scintillator trackers can be useful. One of the most critical challenges remaining to the international security establishment is related with the effective detection of nuclear materials, also properly shielded. In 2008, the following note was written in a report by the US General Accounting Office: *"we found that a cargo container containing a radioactive source was not detected as it passed through radiation detection equipment that DOE had installed at a foreign seaport because the radiation emitted from the container was shielded by a large amount of scrap metal. Additionally, detecting actual cases of illicit trafficking in weapons-usable nuclear material is complicated: one of the materials of greatest concern in terms of proliferation - highly enriched uranium - is among the most difficult materials to detect because of its relatively low level of radioactivity".*

In this context, there is a clear necessity for a specific solution to overcome this highly dangerous threat. The requirements for a screening system are:

- Distinguish broad range of contraband cargo containers;
- Provide density, shape and composition images;
- Scan consolidated cargo without unpacking;
- Rapid scans (a few minutes/container) and short acquisition time;
- Minimum number of false indications;
- Comply with strict radiation safety requirements for both operating staff and cargo irradiation;
- Readily integrated with existing port/airport systems;
- Reasonable capital and operating costs.

Considering worldwide ports, the traffic of containers transported by cargo ships it is estimated in 200 Millions containers per year. Despite many of them could illegally transport nuclear weapons or material hidden inside, only the 1% of them is inspected because of the lack of appropriate scanning systems.

Nowadays, high-energy x-ray or γ-ray radiography and tomography are the most commonly used screening techniques, providing high-resolution images of shape and density. The x-ray radiography technique was pioneered in the 1930s and has become a cornerstone of modern diagnostic medicine and non-destructive industrial material analysis. Modern tomography systems came of age in 1972 and use computer to process the tomographic information to enhance the signal to noise ratio of the image, identify critical features in enhanced visualizations and to allowing multiple slices of the object to be assembled and analysed as a three-dimensional object. Further data processing algorithms have allowed the interpretation of scattering information as radiation passes through a material – versus attenuation information used in traditional x-ray tomography – as a means of studying the composition and structure of the internals of an object. These methodologies can be employed, with statistical analysis, to use the multi-path scattering of radiation to produce tomographic images that provide sufficient information about the energy and direction of the radiation as it enters and leaves the object.

In order to create the radiography image, a heterogeneous beam of x-rays is produced by an x-ray generator (energy range of 10-100 keV) and is projected toward the object. A certain amount of x-rays is absorbed by the crossed object, in correlation with the density and composition. Usually, x-rays that pass through the object are captured behind the object by a detector. For a more accurate resolution measurement, it has better to placing a detector plane also before the object to be studied in order to track each crossing particle before and after the collision with the object. Then, the detectors can provide a superimposed 2D representation of the object internal structures.

The application of alternative techniques, such as *directional gamma imaging* and *neutron radiography*, is complex and expensive, and the performances can be seriously degraded in presence of shielding materials.

PORTAL overcomes these limitations providing tomographic images by muon tomography. The muon flux at sea level is about 1 muon/(cm^2·min) considering an

energy and angular range useful for tomography. The detection principle is based on the detection of the scattering angle of each muon from cosmic ray radiation as a result of crossing a high-Z material (both nuclear material and high-Z shielding materials). Indeed, the angular and position deflections of the trajectory are very sensitive to the atomic number of the atomic nuclei. The scattering angle can be reconstructed by the incoming and outgoing tracks than respect to the inspected object.

Comparing the inspection techniques exploiting x-rays, γ-rays or other particle sources (neutron, ions) to muon tomography, the last presents some advantages.

Firstly, the scan is not invasive. Not only the technique does not require opening the container, but also the cargo content is not damaged because muons are Minimum Ionizing Particles (MIP).

Secondly, the acquisition time (3D image) is reduced to a few minutes, in contrast with the time required by x-ray radiography (about 60 s per a 2D slice, using the CT method).

Lastly, muon radiation is a natural source so that it is not required to introduce an external source that could be dangerous for the environment and for the operators.

*This thesis concludes with **Chapter 4** reporting the accurate descriptions of the PORTAL architecture, the characterization of each individual component, the experimental tests and the construction phase.*

The detector includes 8-position sensitive planes, 6 m long and 3 m wide, large enough for the inspection of standard containers ($244 \times 259 \times 610$ cm^3). Each plane is made of strips of plastic scintillators coupled with a very sensitive photon detector, the Silicon Photomultiplier (SiPM) described in Chapter 1. Detector components were chosen after the evaluation of appropriated test and simulation results. For the reconstruction of tomographic images, tracking algorithms and suitable imaging software were specifically developed.

The research program for the Muon Portal Project includes the development of simulation procedures, the choice of detector elements to be used, the characterization of the photosensors used for the detection apparatus, the read-out electronics, data acquisition software performing also control and visualization. A preliminary study consisting of a considerable amount of theoretical analysis, supported by GEANT4 simulations has been conducted. Simulation results demonstrate the possibility of reaching detection times of few minutes. They also shown that information provided by the scintillating detector after muon interrogation permits to identify and localize illicit high-Z material, even in the presence of shields designed to mask its existence.

As mentioned before, *PORTAL* is the result of a training program in the design, construction and test phases started with the OFFSET tracker. In Chapter 4, similarities between *OFFSET* and *PORTAL* are emphasized:

- Both detectors are highly segmented, with sensitive areas consisting of scintillating materials: Saint Gobain Sci-Fis for *PORTAL* and extruded plastic scintillator strips for *OFFSET*;

- The reduction channels strategy is applied to both described detectors, but in different ways: in the first case an optical reduction technique is used by properly grouping the fibers, while in *PORTAL* the reduction is applied to the analog signals;
- Both detectors have modular front-end and acquisition electronics, scalable and available as complete products in the specific market. In addition the electronics is programmable by LabVIEW software and the data read-out is real-time (average particle rate is lower than acquisition rate).

Even if the generic idea on their operating functionality is common, properly specifications fit with the required performances. For example, it is preferred to use SiPMs for the Muon Portal detector than PMTs as photosensors due to the huge amount of read-out channels (9600 channels without applying reduction). Indeed SiPMs have smaller sizes and don't require high voltage supplies.

Since the Muon Portal detector is a double tracker, the Muon Portal could be considered an OFFSET3-like double tracker.

In the concluding section, the improvements of this kind of detectors are summarized, demonstrating their possible effectiveness use in the two research fields mentioned.

Chapter 1
SCINTILLATING PARTICLE TRACKERS

1.1 Particle trackers

1.1.1 Detection principle

Particle detectors can be classified in relation to the physical magnitudes that they are able to measure such as the determination of the impact position, the measurement of the total energy, the arrival frequency of the particles, the identification of the mass, and so on, apart from the geometrical characteristics, materials, applied technology and so on.

Indeed, the detector is often a set of various nature detectors concatenated together so as to give the information you need to characterize the physical event [1].

A *tracker detector* consists of at least two position detectors placed at a certain distance between them. From the impact position in each detection plane it is possible to reconstruct the track of the particle that has crossed them. In some cases each tracking logical level is made of two physical planes, one for each spatial coordinate *X* or *Y*. By using appropriate algorithms, the 3D track can be reconstruct thanks to an off-line or a real-time software analysis.

The detection principle regarding all particle detectors is the transfer to the sensitive volume of the device of all or part of the energy of a particle that passes through the sensitive area of the detector, so that it is converted, directly or indirectly, into an electrical signal [2].

Charged particles lose energy through electromagnetic collisions with electrons or atomic nuclei that compose a solid material, causing its excitation or ionization. The created charges could be detected. E.g. *gas detectors* are able to directly detect charged particles by gas ionization and generate an electrical signal proportionally to the delivered energy.

Neutral particles must first undergo an intermediate reaction, which allow the formation of charges that can, then, energize or ionize the atoms of the material that characterizes the detector itself (indirect detection).

In the case of indirect detection, for example in the *scintillators*, the excitation and ionization of the atoms of the detector contribute to induce molecular electronic transitions whose effect is the emission of light: the latter is subsequently converted into an electrical signal via electronics devices such as photodiodes and photomultiplier tubes.

In modern detectors, in most cases, the signal generated by a particle, in a certain point on the path of revelation, is converted into an electrical signal and is then processed with electronic circuits. This constitutes an advantage, given that electronics

and computers are getting faster and accurate processing of information. This does not imply that there are only detectors of this type even though often the choice falls on the latter for the reasons set out above.

1.1.2 Detection characteristics

Some characteristics must be considered to define the quality of the measurements performed with any radiation detector, i.e. *spatial resolution*, *time resolution*, *energy resolution*, *detection efficiency* and *dead time*.

The discernible details detected are dependent on the *spatial resolution* of the sensor and refer to the size of the smallest possible feature that can be detected. In other words, it is the minimum distance at which it is possible to distinguish two close signals.

For a homogeneous feature to be detected, its size generally has to be equal to or larger than the size of the smallest element. In the case of imaging detectors, the sensing images are composed of a matrix of picture elements, or pixels, which are the smallest units of an image. Image pixels are usually squared and represent a certain area on an image. It is important to distinguish between pixel size and spatial resolution: they are not interchangeable. If a sensor has a spatial resolution of 20 meters and an image from that sensor is displayed at full resolution, each pixel represents an area of 20x20 m^2 on the ground. In this case the pixel size and resolution are the same.

Time resolution is the criterion for the quality of a time measurement. In general, the standard deviation is used to describe the resolution, i.e. the root of the variance. It plays a role in fast triggering, particularly for *Time Of Flight* (TOF) measurements. The time resolution can be influenced by the material, the size and the surface of the scintillation counter, the properties of the light guide, the fluctuation in gain and the spread in transit time of the light detector, and the threshold of the discriminator. In the case of large scintillation counters, a "mean-timer" circuit averaging over the arriving time of the light signals at either end of the scintillator can correct for the delay due to the distance the light has to travel in the scintillator. Typically the time resolution in TOF measurements varies from 0.1 to 1 ns for high-quality scintillators. For drift chambers, spatial resolution and time resolution are closely related in a drift chamber [3]. The term resolution is used in a double sense: it describes the effective resolution achieved on measuring points on an isolated track, and the resolution of two points from two nearby tracks.

Let us examine the response of the detector to a mono-energetic source of radiation. In the same conditions, different detectors might produce different pulse height distributions, called the *response function* of the detector for the energy used in the determination.

Figure 1.1 shows, for an initial particle energy, the distribution is centred around a common average value ε_0, but the standard deviation (σ) of the curves is different in relation with the performances: a minor σ regards a better energetic resolution detector.

The differential pulse height distribution for a hypothetical detector is shown under the same assumption that only radiation for a single energy is being recorded.

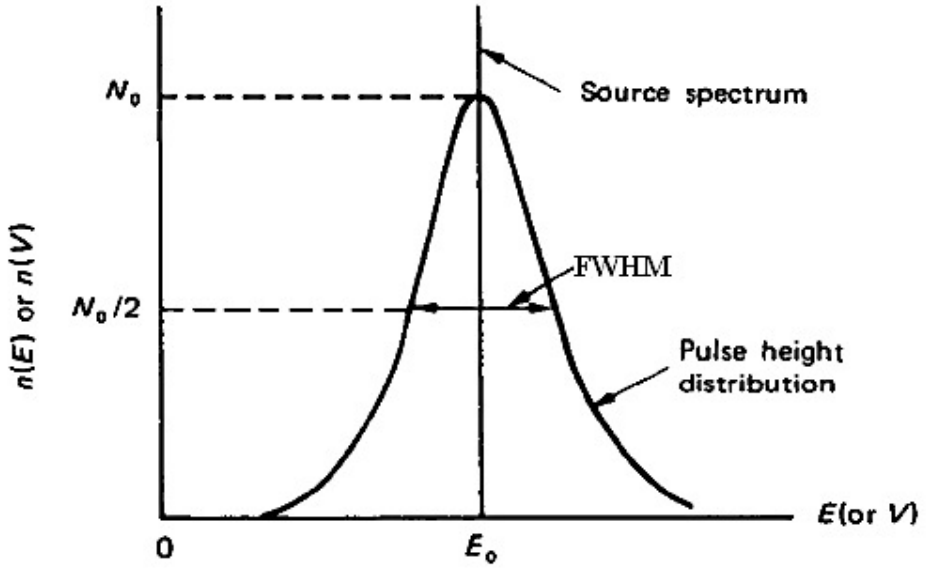

Figure 1.1 - Energy resolution of a detector in response to a mono-energetic particle.

The *Full Width at Half Maximum* (FWHM) is defined as the width of the distribution at a level that is just half the maximum ordinate of the peak. This definition assumes that any background or continuum on which the peak can be superimposed is negligible or has been subtracted away. The energy resolution of the detector R is conventionally defined by the FWHM divided by the location of the peak centroid ε_0, so it is a dimensionless fraction, conventionally expressed as a percentage. Scintillation detectors used in gamma-ray spectroscopy normally show an energy resolution R in the range of 5-10%.

An estimate of the amount of inherent fluctuation can be made by assuming that the formation of each carried charge is a Poisson process. Under this assumption, if a total number N of carried charges is generated on the average, one would expect a standard deviation of $\sqrt{N}$ to characterize the inherent statistic fluctuations in that number. If this were the only source of fluctuation in the signal, the response function should have a Gaussian shape, because N is typically a large number. The width parameter sigma determines the FWHM = 2.35σ. The response of many detectors is approximately linear, so that the average pulse amplitude is $\varepsilon_0 = KN$, where K is a proportionality constant. The FWHM is than $2.35K\sqrt{N}$. We then would calculate a limiting resolution R due only to statistical fluctuations in the number of charge carriers as:

$$R_{Poiss} = \frac{FWHM}{KN} = 2.35/\sqrt{N} \quad (1.1)$$

Considering the variation of the observed statistical fluctuations in the number of charge carriers from pure Poisson statistics we can introduce the *Fano factor* defined as:

$$F = \frac{observed\ variance\ in\ N}{Poisson\ predicted\ variance\ (=N)} \quad (1.2)$$

Because the variance is given by σ^2, the equivalent expression to the previous equation is:

$$\mathrm{R_{Statistical\ limit}} = \frac{\mathrm{FWHM}}{\mathrm{KN}} = \frac{2.35}{\sqrt{\mathrm{F/N}}} \quad (1.3)$$

It is convenient to distinguish between absolute and intrinsic efficiencies. Absolute efficiency E_{abs} is defined as the number of recorded pulses divided by the number of radiation quanta emitted by source. It depends on the detector properties and also on the detector geometry (also by its distance from the source). The intrinsic efficiency E_{int} is defined as the number of pulses recorded divided by the number of quanta radiation incident on the detector.

The two efficiencies are simply related for isotropic sources by $E_{int} = E_{abs}\,(4\pi/\Omega)$, where Ω is the solid angle of the detector seen from the actual source position.

In all detectors systems there is a minimum amount of time that must separate two events in order that they could be recorded as two separate pulses. This minimum time separation is usually called the *dead time* of the counting system. The limiting time is due to processes in the detector itself, and in other cases in the associated electronics. Two models of dead time behaviour of counting system have come into common usage: *paralyzable* and *non-paralyzable* response. The two models predict the same first-order losses and differ only when true event rates are high. They are in some sense two extremes of idealized system behaviour and real counting systems will often display an intermediate behaviour between them.

We adopt the following definitions:

n = true interaction rate
m = recorded count rate
T = system dead time

Assuming that the counting time is long so that both *m* and *n* may be regarded as average rates, we would like to obtain an expression for the true interaction rates as a function of the dead time *T*.

In the non-paralyzable case, the fraction of all time that the detector is dead is given simply by the product mT. Therefore, the rate at which true events are lost is simply nmT. Since n-m is another expression for the rate of losses:

$$n - m = nmT \quad (1.4)$$

Solving for n, we obtain:

$$N = m/(1 - mT) \quad (1.5)$$

In the paralyzed case, dead periods are not always of fixed length, so we cannot apply the same argument. Nevertheless, the rate m is identical to the rate of occurrences of time intervals between true events, which exceed T. The distribution of intervals between random events occurring at an average rate n is:

$$P_1(T)dT = ne^{-nT}dT \quad (1.6)$$

Where $P_1(T)dT$ is the probability of observing an interval whose length lies within dT about T. The probability of intervals larger than T can be obtained by integrating this distribution between T and ∞:

$$P_2(T) = \int_T^\infty P_1(T)\, dT = e^{-nT} \quad (1.7)$$

The rate of occurrence of such intervals is that obtained by simply multiplying the above expression by the true rate n:

$$M = ne^{-nT} \quad (1.8)$$

1.2 Large-area highly segmented detectors

1.2.1 Applications

In the previous section particle trackers have been discussed in general together with their characteristics. Apart from their properties, they can be distinguished for their sizes and for their spatial resolution, which is connected to the pixel/strip size in case of segmented detectors. Now a particular category of particle trackers interesting for our applications will be discussed: large-area highly segmented detectors.

The applications for large sensitive area detectors with a high segmentation are multiple. First of all, they could be applied in the field of *medical physics* for the detection of crossing charged particles. In fact, more and more frequently there are requests for large-area detectors, capable of real-time tracking the charged particles passing through them in order to perform:

- Radiography and tomography of human tissues;
- Monitoring and imaging of a clinical beam;
- Positioning of a patient before a hadronteraphic treatment.

Radiography is an imaging technique that uses electromagnetic radiation, especially X radiation to inspect and visualize the internal structure of a non-uniformly composed and opaque object (i.e. a non-transparent object of varying density and composition) such as the human body. To create the image, a heterogeneous beam of x-rays is produced by an x-ray generator and is projected toward the object. In correlation with the density and composition a certain amount of x-ray is absorbed by the crossed object. Usually, x-rays that pass through the object are captured behind the object by a detector. For a more accurate resolution measurement, it has better to placing a detector plane also before the object to be studied in order to track each crossing particle before and after the collision with the object. Then, the detectors can provide a superimposed 2D representation of the object's internal structures.

In tomography, the x-ray source and detector move to blur out structures not in the focal plane. Conventional tomography is rarely used now having been replaced by *Computed Tomography* (CT). Unlike plain-film tomography, CT scanning generates 3D representations used for computer-assisted reconstruction.

Another possible application is the detection of *cosmic radiation*, for making of radiography or tomography of an object to be inspected (for example, as will be shown in Chapter 3, to inspect the content of containers transported by ships goods) or area to control as in the case of volcanic tomography. These detectors could also observe the *atmospheric shower* [4], by measuring coincident events between several detectors of the same type placed at a certain distance each other.

Moreover, a big application field of these kinds of detectors is the research in *nuclear* and *particle physics*. Indeed the reaction products from beams collision, or from a single particle source can be studied.

1.2.2 Specifications for high spatial and angular resolutions

After a panoramic of the possible applications for large-area, highly segmented detectors, some important specifications for the evaluation of the detector performances are discussed.

Position accuracy refers to the precision with which an object can be localized in a space. For all the applications discussed in the previous section, good spatial and angular resolution optimize the ability to reconstruct faithfully the object under examination. For a segmented detector, in one direction it could be calculated as the pixel size divided by square root of twelve. As a result, a small strip size will correspond to a better image quality, e.g. the required spatial resolutions are less than 0.5 mm in case of human body radiography.

The *angular resolution* of a 3D detector (consisting of more layers placed at a certain distance) could be geometrically calculated from the spatial resolution, considering the distances between the tracker planes. Many other aspects have also to be considered for these calculations, such as the dead areas of the detector, so it has better to performing accurate simulations in order to have a more realistic idea of the detector response. For instance, in case of the detector that will be described in Chapter 3, as a result of a simple geometrical calculation the angular resolution is equal to 0.3 degree, but by the simulations this value seems to be bigger, with an addition of 0.2 degree.

Let us discuss about the detection efficiency for a segmented detector.

In many cases, it could be calculated as for a composite detector (a detector that is realised by the union of several independent detectors).

The *detection efficiency* of a composite detector is higher than the efficiency of a single crystal detector with the same volume. Indeed, the overall efficiency of a composite detector is a sum of two different primary factors:

- The direct detection efficiency ϵ_D is given by the photo-peak efficiencies of each crystal considered as a single detector. It is measured by recording, separately, the full radiation absorption in each of the individual crystals. For the case of a detector made of *n* crystals the direct efficiency is given by:

$$\epsilon_D = \sum_{i=1}^{n} \epsilon_{D,i} \quad (1.9)$$

- The coincidence detection efficiency, also called the add-back efficiency ϵ_{AB}, is measured by summing the energy deposited in the composite detector on an event by event basis. The total energy is then recovered by summing the partial energy deposited in the individual crystals.

Hence, the total detection efficiency can be written as:

$$\epsilon = \epsilon_{AB} + \epsilon_D \approx n\epsilon_{D,1} + \epsilon_{AB} \quad (1.10)$$

The approximation in eq. 1.10 is valid in the case that *n* crystals have all the same efficiency. The gain in efficiency obtained by adding coincidence signals together is given by the add-back factor *A*:

$$A = 1 + \epsilon_{AB}/\epsilon_D \quad (1.11)$$

However, it must be considered that coincidence events can also be due to multiple hits, i.e. two particles hitting the detector simultaneously. If energies of multiple hits are added together into the spectrum, they would contribute to the background signal. An additional advantage is provided by the segmentation of a composite detector like the gamma ray detector shown in Figure 1.2. It enables one to distinguish between multiple hit events and gamma ray Compton scattering between two adjacent crystals [5].

Other advantages due to segmentation are the minimization of dead material budget between *scatterer* (the detector itself) and *analyzer* (the read-out electronics is dedicated for each segment). Moreover, the sum signal is detected at a common electrode of segments, so that the resolution is improved as only the noise of one electronics channel contributes.

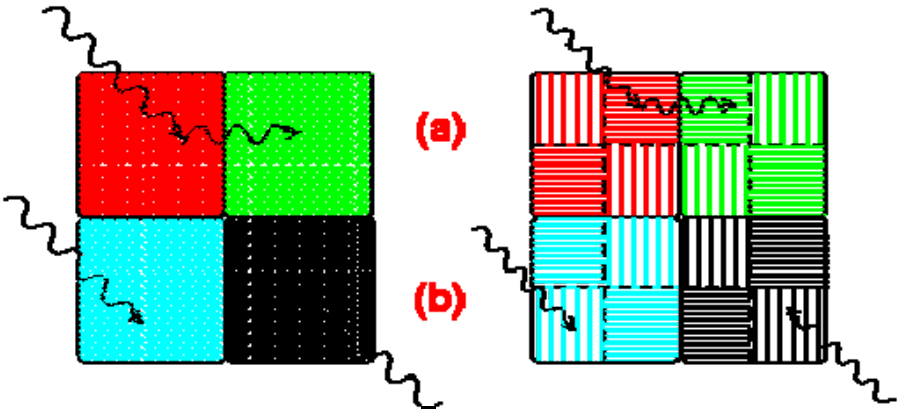

Figure 1.2 - A segmented detector enables one to distinguish between secondary scattering particles (a) and multiple hit events (b) in two adjacent crystals.

1.2.3 Smart read-out strategies to give up real-time performances

Considering the total number of read-out channels of highly segmented trackers with large area, it could be too much large if you had to read all of them individually. In this section, a smart read-out channel reduction strategy is described [6]. It is very useful if applied to these types of detectors in order to give up real-time performances. This architecture reduces the number of read-out channels for a linearly segmented detector.

The operating principle of the channel reduction is explained below. We can consider a strip detector. It detects one particle at a time. Each strip is read from both ends and the signals are grouped in a special way, which results in a significant lower number of read-out channels compared to those when each strip is read-out at one end with a dedicated read-out channel. All strips on one end are read-out in groups of n neighboring strips, named *NeigSet*, while at the other end the first strips of each group are grouped in *StripSet* 1, the second strips of each group in *StripSet 2*, and so on to n (Figure 1.3). This implies that the number of read-out channels on the second side is equal to the number of fibers per channel on the first side. A particle crossing one strip generates a signal at both ends of the fiber. Then we have a signal from the i^{th} *NeigSet* group and another from the j^{th} StripSet that univocally identifies the hit strip ($Strip_{hit}$) according to equation (1).

$$Strip_{hit} = (i - 1)\, n + j \quad (1.12)$$

An X-Y strip detector with 16 strips for each plane is shown in Figure 1.3, as an example of a two-dimensional strip detector where the channel reduction system is applied. In a classical read-out scheme of a two-dimensional strip detector with 16 strips in each dimension, there would be 16 read-out channels for the *X* direction and 16 for the *Y* direction, making a total of 32 channels.

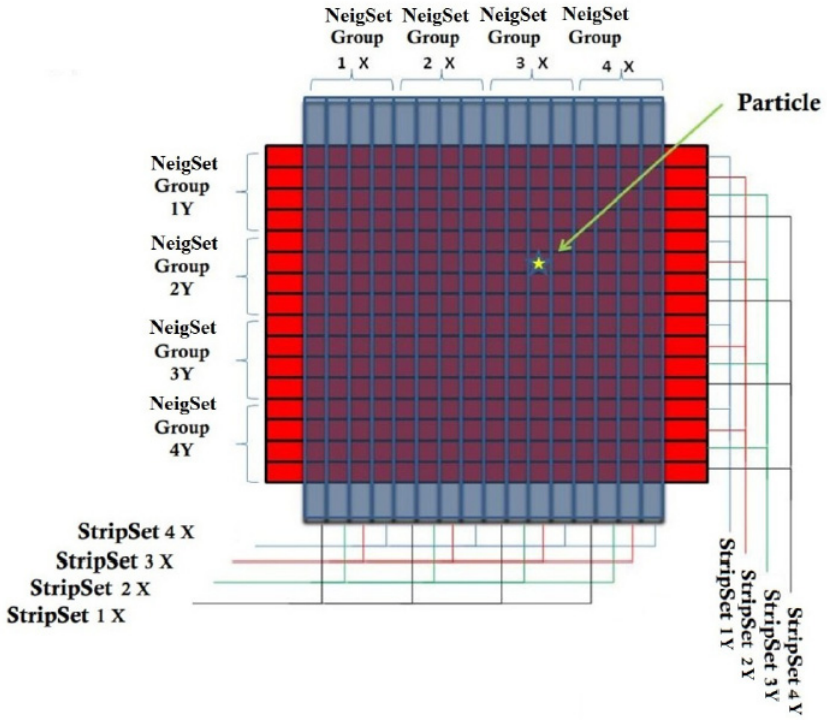

Figure 1.3 - Scheme of a segmented X-Y detector useful to clarify the application of compression channel technique.

The proposed read-out scheme reduces the number of read-out channels to 16. In general the number of read-out channels needed to read-out both dimensions with this scheme is $4\sqrt{N}$, where N is the total number of strips per layer, X or Y. When N is large the reduction factor becomes important, in order to achieve real-time acquisition. An additional advantage of this read-out scheme is that the required read-out of the signal at both ends of a fiber significantly reduces accidental triggers due to noise, crosstalk, dark counts, etc. Notice that to reconstruct the point where the particle crosses the detector (event), we need an energy release in both planes. The characteristics required for each application depends on the particular application desired. For example, in the case of medical applications, the spatial resolution offered by the detectors of the latest generation is less than 0.5 mm. The reduction strategy has been patented by the *National Institute of Nuclear Physics* (INFN) [7].

1.3 Scintillating trackers as a good compromise for the selected applications

1.3.1 Introduction

In order to reach the required performances of high spatial/angular resolution, the solution that we have chosen is the employment of scintillating trackers, which are an optimal compromise among the various models of detectors in the specific market. Indeed, the relative reduced cost of plastic scintillators respect to other materials (e.g. Silicon, Germanium or Ceramics) and the possibility to modelling different shapes and sizes is of good advice for large-area detectors and also to obtain the high segmentation. In particular, by using the scintillating fibers it is possible to curve fiber in order to apply the compression channel technique described in the section 1.3.3 at an optical level, by routing the optical fibers in a suitable way. It leads to real-time performances for the read-out. In the following sections the properties of the scintillating materials are described in detail.

1.3.2 Scintillating materials

Scintillators are detectors that emit a light signal when they are hit by a particle. They are usually coupled to a device sensitive to the light emitted giving an electrical signal as a response.

Often, the coupling is made by an unconventional light-guide. It is able to shift the wavelength of the photons to improve their read-out by the photomultiplier and to channel them towards the guide.

Some materials absorb and re-emit the energy in the form of visible light when exposed to ionizing radiation or a particles beam. When this phenomenon, called *luminescence*, occurs after a period of 10-8 s it is called *phosphorescence* or *afterglow*, while if it occurs in a lower time interval it is called *fluorescence*. The fluorescence process is the prompt emission of visible radiation from a substance following its excitation by some means. Phosphorescence corresponds to the emission of longer wavelength light than fluorescence, and with a characteristic time that is generally much slower. Delayed fluorescence results in the same emission spectrum as prompt fluorescence, but again is characterized by a much longer emission time following excitation. To be a good scintillator, a material should convert as large a fraction as possible of the incident radiation energy to prompt fluorescence, while minimizing the generally undesirable contributions for phosphorescence and delay fluorescence.

The scintillators are both *organic* and *inorganic*, depending on the used glittering material; the mechanism of light emission is also different. The most widely applied scintillators include the inorganic *alkali halide* crystals (*sodium iodide* is the favourite among them) and organic based liquids and plastics.

The desired application also has a major influence on scintillator choice.

The inorganic scintillators tend to have the best light output and linearity, but they are generally slow in their response time. Organic scintillators are usually faster but yield less light. The high Z-value of constituents and high density of inorganic crystals favour their choice for gamma-ray spectroscopy, whereas organics are often preferred for beta spectroscopy and fast neutron detection.

The properties of organic scintillators can be summarized as follows:

- The emission of light radiation occurs in a very short time, less than 10 ns [2], which makes the organic scintillating detectors the fastest in emission of light;
- The bright response is less than the best inorganic scintillators and, therefore, amplifiers are necessary for higher acquisition performances in light emission;
- Thanks to their plasticity, several geometric configurations not permitted with the rigid crystal structures of inorganic scintillators can be realized.

In organic scintillators, in general, the luminescence is due to individual molecules [8], typically placed in a solution where the solvent is also consisting of an organic substance in solid or liquid form. In the case of solid, e.g. in the scintillating fibers, a polymer (polystyrene, polyvinyltoluene, PolyMethylMethAcrylate or abbreviated PMMA) or a crystal is usually used.

The molecule responsible for the scintillation (or fluorescence) is called primary fluorine. Typically, the attenuation length of the light emitted from this molecule is very small and the radiation is re-absorbed by the same primary fluorine after a few centimeters. For this reason it is often inserted into a scintillating second molecule, called secondary fluorine. This second element has the task of absorbing the light emitted by the primary fluorine and re-emit at a longer wavelength, in such a way as to ensure the transmission until end of the scintillator.

Both *phosphorescence* and *fluorescence* follow an exponential law. Therefore, since both of them are present in the mechanism of scintillation, the simplest way to describe the signal of the scintillator is the following:

$$N(t) = Ae^{(-t/t_f)} + Be^{(-t/t_s)} \quad (1.13)$$

where $N(t)$ is the number of photons emitted at time t, while t_f and t_s are the decay constants of the fast and the slow component, respectively. The constants A and B vary for different materials, however, the fast component is the dominant one, as shown in Figure 1.4.

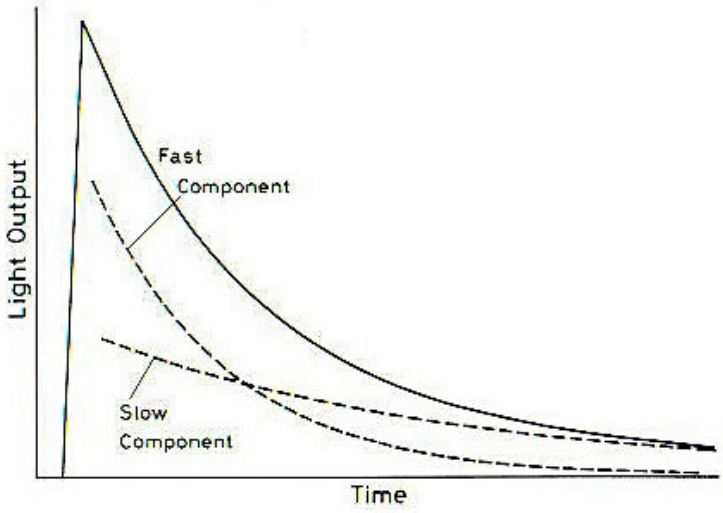

Figure 1.4 - Representation of the exponential emission trend of the emission light by a photomultiplier into its two components, the fast and slow and their sum.

A good scintillator must meet some basic requirements such as high efficiency and a small decay constant, it must also issue a wavelength that is compatible with the photomultipliers used and must be as transparent as possible to the radiation it emits.

1.3.3 Plastic scintillators

Plastic scintillators are a special type of organic scintillators. They can be produced dissolving a solvent in an organic scintillator so that it can be subsequently polymerized. Usually fluorspar, which acts as a wavelength shifter, is added to expand the attenuation length of the photons.

In this case the mechanism of scintillation is due to the excitation and the subsequent return to the ground state of the valence electrons of the free molecules, located in the orbital molecular π.

The scintillation process remains one of the most useful methods available for the detection and spectroscopy of a wide assortment of radiations [2]. A good scintillation material should be a good compromise among the following properties:

- It should convert the kinetic energy of charged particles into detectable light with a high scintillation efficiency;
- This conversion should be linear. The light yield should be proportional to deposited energy over as wide a range as possible;
- The medium should be transparent to the wavelength of its own emission for good light collection;
- The decay time of the induced luminescence should be short so that fast signal pulses can be generated;

- The material should be of good optical quality and subject to manufacture in sizes large enough to be of interest as a practical detector;
- The index of refraction should be near that of glass (about 1.5) to permit efficient coupling of the scintillation light to a photomultiplier tube or other light sensors.

A better understanding of the mechanism of scintillation is explained in Figure 1.5, where the energy levels of the singlet and triplet of a molecule were separated.

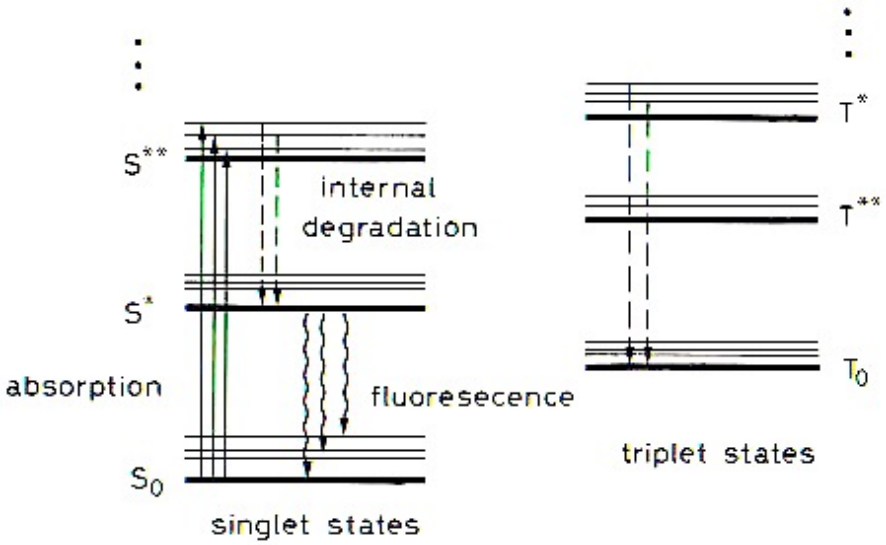

Figure 1.5 - Energy levels within a molecule of a plastic scintillator.

S_0 indicates the ground state, while *S**, *S***, etc. are the singlet excited states; T_0 is the first level of the triplet and *T**, *T***, etc. are its excited levels; the energy is of a few eV. The thin lines indicate a split in the vibrational levels, involving a jump of a few tenths of eV from the ground state.

When an electron in the single state is excited, it decays in a very short time (<10 ps) into the state *S** without the emission of radiation, then decay into one of the vibrational states of S_0 in a few ns with emission of light, typically in the range of UV. Transparency to its radiation was due to the decay in a vibrational state: in this way the emitted photons do not have sufficient energy to excite the other scintillator molecules (known as quenching effect). As you can guess from the typical times, this phenomenon explains the fast component of the emitted light.

The delayed component is explained instead by the decay of the triplet state. To reach the state T_0, decays occur without emission of light and the direct decay from this state to S_0 is strongly prohibited by the selection rules.

The emission of radiation is permitted following the interaction

$$T_0 + T_0 = S^* + S_0 + {}^2phonons \quad (1.14)$$

from which the state S^* repeats the pattern described above. The typical time depends on the interactions of states T_0 and will be generally delayed with respect the fast component.

Other characteristics of a scintillator are the linearity compared to the energy deposited and the rapid time response.

As regards the first point it is necessary to emphasize that the scintillators give a linear response to energy storage only as a first approximation, for a more complete treatment is necessary to use the *Birks formula:*

$$dL \cdot dx = A \cdot dE/dx \cdot l + k_B \cdot dE/dx \quad (1.15)$$

where *dE/dx* is the energy deposited per unit length and *dL/dx* is the response in light per unit length.

The linear approximation is obtained for large *dE/dx* where $dL/dx \approx A/k_B$. Integrating on the distance travelled by the particle in the scintillator, it results:

$$L = A \cdot R(E)/k_B \quad (1.16)$$

In these conditions, if the photomultiplier has a linear response, the electrical output signal will be proportional to the energy deposited by the particle.

The scintillators are very fast tools with small dead times. The first feature allows their use in detectors that require a very good temporal resolution, such as systems to measure the TOF, while the second makes them suitable for experiments, which involve high counting rates.

Plastic scintillator generally emits UV radiation characterized by a short attenuation length: despite the considerations made above, in fact, one cannot overlook the phenomenon of self-absorption caused by the superposition of the absorption band with that issue; the difference between the wavelengths of the emission peak and the absorption peak is called *Stokes' shift*. In order to have a good scintillator, a large *Stokes' shift* is required. Fluorite is added to move wavelengths towards a region with greater attenuation length, in such a way the efficiency of the scintillator is increased. In fact, fluorite absorbs the light emitted from the scintillator and re-emits light in the blue region [9].

Plastics have become an extremely useful form of organic scintillator because of its ease to be shaped (as roads, cylinders or flat sheets as shown in Figure 1.6) and realized. Moreover, they are relative inexpensive, so that plastics are often employed as large-volume solid detectors. In this case the self-absorption of the scintillator light may no longer be negligible and some attention should be given to the attenuation properties

[2] Acoustic phonons are quanta of radiation; the distribution of elastic vibrations due to thermal excitation of a solid can be determined by applying the duality particle-wave the acoustic radiation. The concept is similar to that of photon seen as the electromagnetic radiation.

of the material. The distance in which the light intensity will be attenuated by a factor 2 can be as much as several meters.

Figure 1.6 - Plastic scintillators of different shapes, colours and sizes.

1.3.4 Scintillating fibers

Scintillating fibers are optical fibers doped with molecules of sparkling substances. They consist of a transparent inner part, said *core*, covered by another transparent material, labelled *cladding*.

In the most common scintillating fibers, the core is made of polystyrene doped with organic molecules, usually benzene, while the exterior cladding is made of PMMA. In some fibers, then, a further outer coating is also present, called *Extra Mural Absorber* (EMA), which acts as protective sheath and limits the effects of cross talk between adjacent fibers.

The two interior materials are coaxial and have different refractive indexes (polystyrene n = 1.60, PMMA n = 1.49). The clad has a refractive index lower than the core to allow the transport of light inside the fibers and prevent loss along the walls. Finally, some types of fibers are equipped with an additional cladding layer, said multi-cladding, with refractive index lower than the first cladding, the function of which is to increase the efficiency of light transport in the fiber itself [10]. A scheme for cross-section of Kuraray fibers is shown in Figure 1.7 [11].

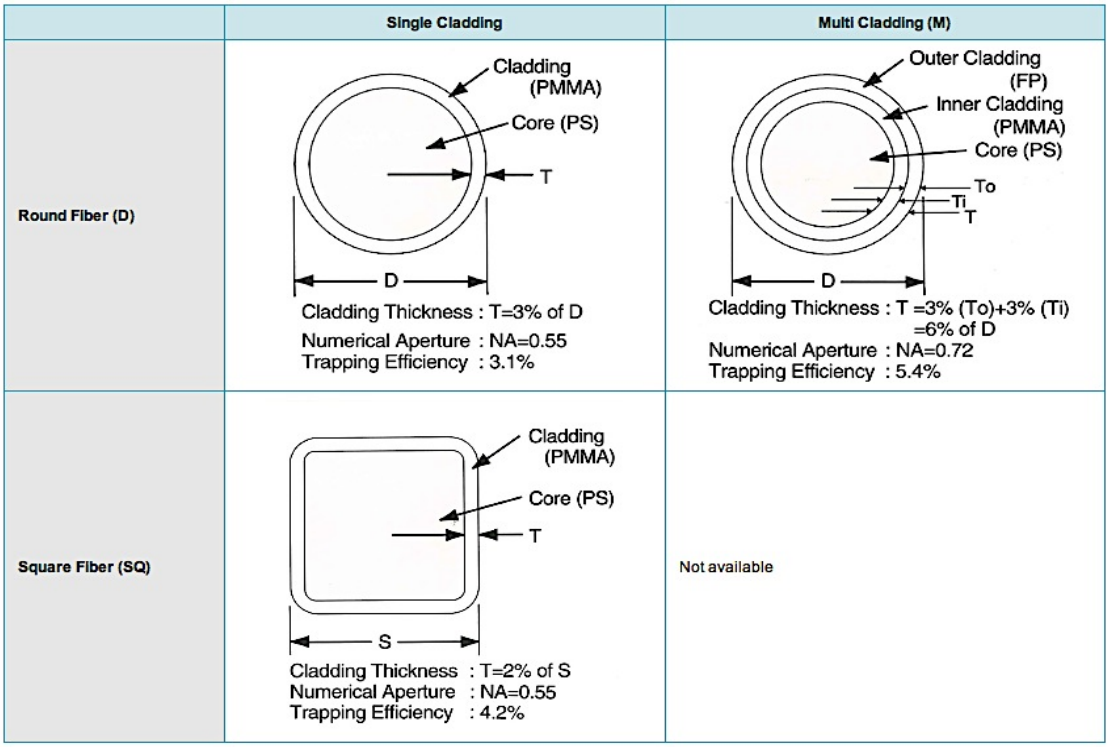

Figure 1.7 - Scheme for cross-section of Kuraray fibers.

The light emitted from the primary fluorine remains inside the fibers due to total reflection on the surface of separation between the inner core and cladding outside. Whereas isotropic emission of light, the limit angle θ_C for which you has total reflection is obtained from *Snell's law* and is:

$$\Theta_C = arcsin(n_{core}/n_{clad}) \quad (1.16)$$

in which n_{core} and n_{clad} are the refractive index of the core and of the clad, respectively.

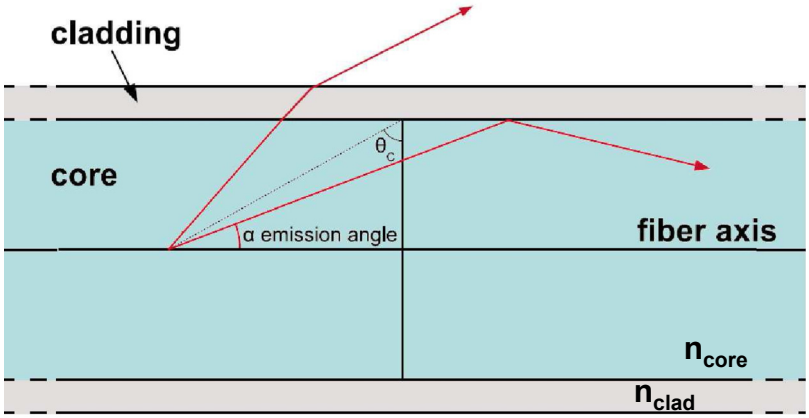

Figure 1.8 - Scintillating fiber longitudinal section. Reflection principle on which is based the transport of the light signal into the fibers is shown. The emission angle is α and the limit angle is θ_C [12].

If the angle of emission ($\alpha = \pi/2 - \theta_C$ in Figure 1.8) is smaller than the limit angle, the transmission of light along the fiber occurs [12]. Therefore, the fraction of light that reaches one end of the fiber depends on the solid angle defined by the emission angle α. In the limiting case of $\alpha = \theta_C$ the portion of light transmitted □ is given by:

$$\varepsilon = \left(1 - (n_{clad}/n_{core})\right)/2 \quad (1.17)$$

However, equation 1.17 is valid if it is only considered light emission along the fiber axis, otherwise it depends on the distance with respect to the fiber axis; typical values range from a minimum of 3.4% near the axis up to a maximum of 7 % in the proximity of the cladding.

1.4 Conversion of the light signal into an electrical signal

1.4.1 Photo-sensors

If the number of photons arriving at the ends of the fibers is small, it is necessary to apply a suitable system capable of generating a signal large enough to be read. The devices usually used for this purpose are photomultipliers (PMT). PMT are able to convert a light signal into an electrical signal.

In today's scenario there are different types of photomultipliers; they differ for the principles of operation, construction and size, and then each of them have characteristics that guide the selection on the basis of detection to be made.

As an example in this work, two types of photomultiplier are used: the *position sensitive PhotoMultiplier* (psPM) and arrays of *Silicon PhotoMultipliers* (SiPM).

A psPM is a matrix of common photomultipliers. For this reason, a simple photomultiplier and its functional principal is summarily described in the following.

A photomultiplier tube consists of a photocathode, made of a material photosensitive that, in general, is an alkali metal, followed by a system of focusing and collection of electrons, a system of multiplication of electrons constituted by dynodes and, also, from an anode from which the signal can be extract, all contained in a glass tube under vacuum.

When photons (coming for example from the scintillator) affect the photocathode, electrons are emitted because of the photoelectric effect. These photoelectrons, accelerated by an applied potential difference, are pushed towards the first dynode where they transfer their energy to the electrons of the material and cause the light emission. They are, thus, the products of secondary electrons, which in turn are pushed on the next dynode creating further electron emission. This process is repeated for the following dynodes, thus creating a "cascade" of electrons, until reaching the anode where the current signal is finally collected to be eventually amplified and

analysed through a proper electronics chain. At the end of the multiplication a current signal proportional to the number of photons incident on the PMT is created.

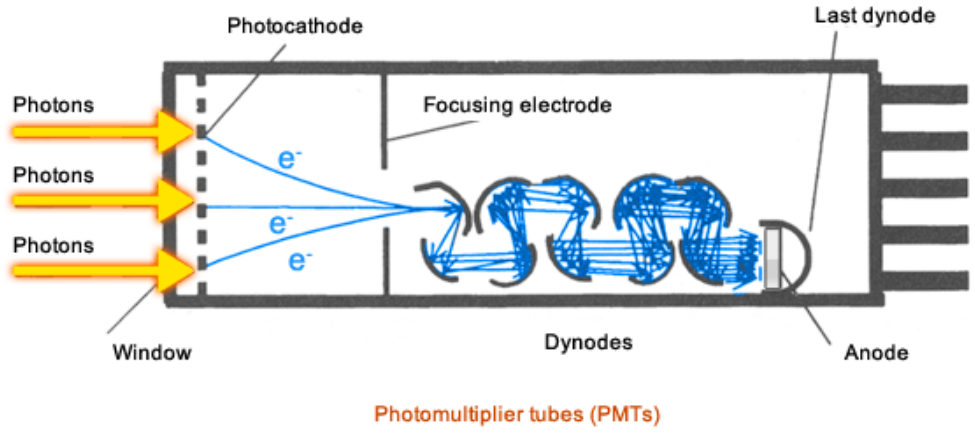

Figure 1.9 - Scheme of the function principle of a photomultiplier.

This process is possible only by increasing the voltage between successive dynodes.

Figure 1.9 shows the scheme of the internal structure of a common photomultiplier and its operation principle, highlighting the following main parts:

- The photocathode, which converts the light photons into electrons (photoelectrons), by means of photoemission;
- Focusing electrodes, which collect and push photoelectrons on the first dynode by a suitable electric field;
- A system of dynodes or electrodes that multiply the charge through the emission of secondary electrons;
- The anode, which collects the electrons flow after the process of charge multiplication and provides the output signal.

As discussed before, each photomultiplier has some features that diversify it from the others and it can be chosen on the basis of these characteristics. Certainly, a photomultiplier is not able to detect photons at any wavelengths. According to the material of which the photocathode is made, it has different filtering windows and therefore it is necessary to choose a suitable PMT for the wavelength you want to reveal. In the choice of a PMT, hence, the primary consideration must be the evaluation of the response to the wavelength of the incident radiation. It must be verified, i.e., the good agreement between the [3]*quantum efficiency* curve of the photocathode as a function of

[3] Quantum efficiency is the ratio of the number of carriers collected by the solar cell to the number of photons of a given energy incident on the solar cell. The quantum efficiency may be given either as a function of wavelength or as energy. If all photons of a certain wavelength are absorbed and the resulting minority carriers are collected, then the quantum efficiency at that particular wavelength is unity.

the wavelength of the incident radiation and the emission spectrum of the source you want to reveal, in order to maximize the number of photoelectrons generated by the photons that strike the emitting material.

Either way, more than 50 types of light emitting materials are in use, with spectral responses ranging from infrared to ultraviolet. In Table 1 there is a brief list of the most common types of photocathodes with their spectral response peak and quantum efficiency peak.

Photocathode material	**Chemical composition**	**Wavelength peak [nm]**	**Quantum efficiency peak**
S1 (C)	Ag-O-Cs	800	0.36
S4	SbCs	400	16
S11 (A)	SbCs	440	17
Super A	SbCs	440	22
S13 (U)	SbCS	440	17
S20 (T)	SbNa- KCs	420	20
S20R	SbNa- KCs	550	8
TU	SbNa- KCs	420	20
Bialkali	SbRb-Cs	420	26
Bialkali D	SbNa-KCs	400	26
Bialkali DU	SbNa-KCs	400	26
BU	Cs-Te	235	10

Table 1 - Spectral response and quantum efficiency peak of some common photocathodes.

A SiPM consists of a planar array of single-photon avalanche photodiodes or SPAD (Single Photon Avalanche Detector), operating in the Geiger regime, and whose anodes are connected in common.

In literature SPAD is indicated as a device capable of providing in output current signals directly amplified in response to a single photoelectron product [13].

A SPAD does not differ from other devices such as photodiodes, what changes is the operating system.

While the term APD indicates an avalanche photodiode operating in linear regime with fixed voltage at its ends, a SPAD is an array of photodiodes and it has in addition a particular circuit, called quenching circuit. The coupling with the quenching allows the photodiode to operate in a condition of digital on-off with a single photoelectron, the so-called *Geiger Mode*.

Each SPAD is essentially made of a p-n junction with high dopant concentration to work in avalanche regime.

We define *Overvoltage* (hereafter named V_{OV} or O_V) as the difference between the voltage bias applied and the breakdown voltage derived from a I-V measurement.

The photodiode is reverse biased at a voltage *Va*, higher than the nominal value of breakdown *BV,* with an Overvoltage value that, in general, is chosen between 10% and 30% of *BV*. With the use of the quenching circuit, the diode is maintained in a state of quiescence forced to the value of voltage *Va*. Hence, this circuit has the task to stop the process of avalanche, lowering the value of supply voltage below *BV*, following the production of the avalanche, with its consequent shutdown.

When a photon is absorbed by the photodiode, the photo-generated electron-hole pair is separated and carriers move to the areas of majority for them due to the electrical field generated in the space charge zone. In this area the carriers, said "primary", are rapidly accelerated by a high electric field triggering quickly an avalanche of charge carriers. A voltage greater than the *BV* gives rise to a gain which depending on the specific case arrives up to 10^6 carriers. The junction capacitance at this point will discharge towards outside, producing a macroscopic current and, by the contrast the voltage on the diode is lowered instantly to the value of breakdown, switching off the current in the diode.

After a certain time interval, the circuit moves the quenching voltage to the nominal value *Va*, so that the photodiode is ready to reveal another photon.

Figure 1.10 shows the I-V current-voltage characteristic of a photodiode. While the voltage moves from *Vc* to *Va*, the current I_A assumes a value several orders higher than I_C. These configurations describe the off-on condition of a photodiode operating in Geiger Mode.

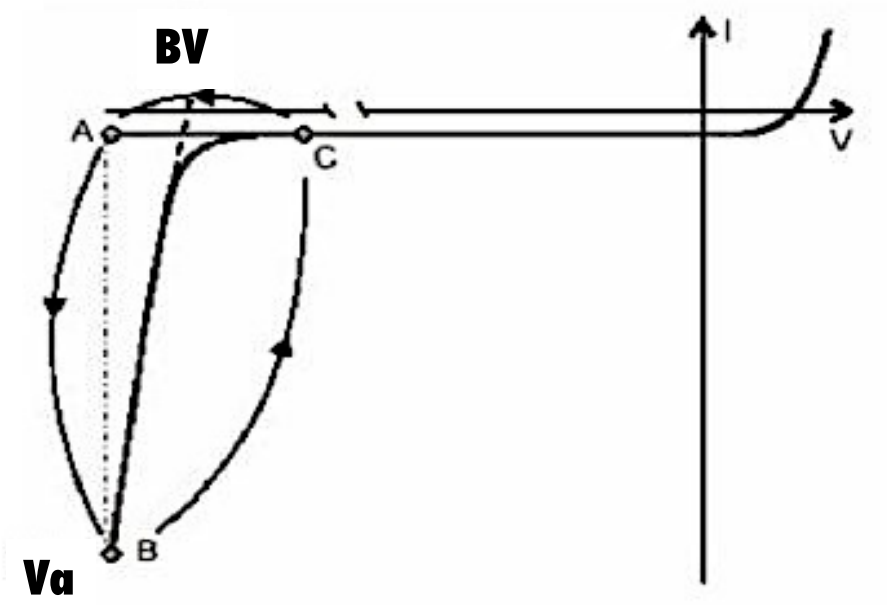

Figure 1.10 - Characteristic I-V of a photo-diode operating in Geiger Mode [12].

The transition B→C represents the step of quenching or avalanche off, while the intermediate step between points C and A is said "hold off", in which in the voltage value is not sufficient to produce a carriers avalanche and the final transition A→B, the step of *hold on*, restores the voltage on the diode to the value *Va*; at this point the SPAD is ready to reveal another photon. This operating condition is obtained with the circuits labelled quenching. The output current from an APD is of the order of few nA and a duration pulse is of the order of hundreds ps. The output signal is closely linked temporally at the arrival of the photon that starts the avalanche in the sensitive zone due to such a prompt response. The Geiger Mode does not allow the avalanche count of the incident photons simultaneously in the APD and, also, until the quenching circuit does not restore the operating voltage of the device, it is insensitive to further incident photons. The need to create arrays of APD allows to count simultaneously more incident photons.

The switching times of the current and voltage are influenced both from some parameters of the photodiode and from the quenching circuit, such as the junction capacitance and the internal resistance. Figure 1.11 shows a circuit diagram of an SiPM where APDs with related quenching circuits constitute the SPAD and that are also called cells or pixels in the SiPM.

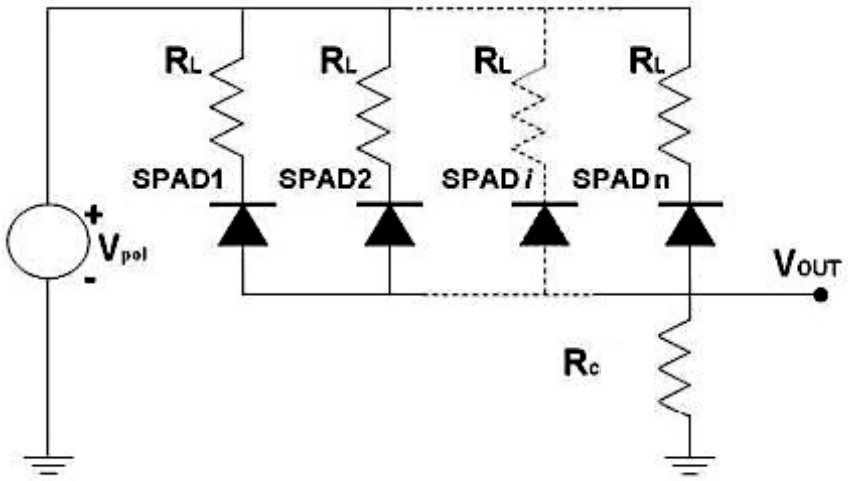

Figure 1.11 - Scheme of a SiPM circuit, seen as a matrix of SPAD [12].

Each SPAD has a quenching resistance R_L connected in series that lowers the value of reverse voltage when the diode is crossed by the impulse current related to the avalanche and decouples SPAD between them. *Rc* is a common load resistance. If all the cells are identical and each emits the same amount of charge when a photon is absorbed, by measuring the total charge output, it can be traced back to the number of hit cells and, consequently, to the number of incident photons. From here, the necessity to realize matrices of APD is evident to allow to count more incident photons simultaneously.

In the latter case, the linear correlation between intensity and amplitude of the output signal is manifested if the possibility to have more photons from a single cell is negligible.

When photons interact with the cell, it generates an electrical pulse. The device remains inactive for the duration of the discharge time of the cell capacity (dead time). Pulses will present a final structure in which single photons are clearly distinguishable.

The main features that have made SiPM objects of considerable interest for many applications are the single photon resolution, high temporal resolution, high gain, low working voltage, small size and insensitivity to magnetic fields. In some cases SiPMs are considered the possible substitutes to ordinary photomultipliers (Figure 1.12).

Figure 1.12 - Picture of a Silicon Photomultiplier inside its socket.

1.4.2 SiPM characteristics

It is important to define some physical quantities that characterize a SiPM.

The gain for a single cell G_{cell} is defined as the ratio between the charge quantity Q_{cell} passing through the cell when the avalanche occurs and the elementary charge of electrons:

$$G_{cell} = \frac{Q_{cell}}{e} = \frac{C_{cell}(V_{pol} - BV)}{e} \quad (1.18)$$

In which C_{cell} is the capacity of each pixel, V_{pol} the supply voltage and BV is the break down voltage. G_{cell} is therefore a macroscopic characteristic depending on the supply voltage and the intrinsic capacity of the cell and it represents the average number of carriers produced during the avalanche.

To estimate the gain of the entire SiPM is necessary to assume that G_{cell} is the same for all cells. Therefore, the breakdown voltage and the intrinsic capacity must be

the more uniform possible in the device. Moreover, G_{cell} depends on the temperature (through *BV*).

If the amount of the total charge Q_{tot} collected to the output of SiPM is known, then it is possible to calculate the total gain G from the equation:

$$G = \frac{Q_{tot}}{n_f e} \quad (1.19)$$

where n_f is the number of incident photons on the SiPM when each cell involved is hit by a single photon. Typically the gain value for a SiPM is of the order of $10^5 \div 10^7$.

The quantum efficiency (*QE)* of a SiPM is the probability that an incident photon is absorbed and generates an electron-hole pair in the active thickness of the device. It is determined by the contribution of various factors and can be expressed as:

$$QE = \varepsilon_G P_V (1 - R)(1 - \varepsilon^{-\eta x}) \quad (1.20)$$

The term ε_G is the geometric efficiency of the SiPM, defined as the ratio between the sensitive area and the total area of the device, also called the fill factor; P_v is the probability that a carrier enters the depletion region and gives rise the avalanche; *R* is the reflection coefficient of the entrance window of the device; η is the linear attenuation coefficient of photons in the silicon and *x* is the thickness traversed.

The ε_G expressed as an active area of the SiPM is not equal to its total area, since each cell is surrounded by a dead region. Among the cells, in fact, aluminium tracks, resistors and channels are present both for physical and for structural reason, preventing the cross-talk, a phenomenon that will be shortly described in the following. Although the area of a cell is very small, of the order of tens μm^2, even of a few microns dead area around the cell can cause a considerable loss of efficiency.

Typically, the fill factor is of the order of 50% in cells of 50x50 μm^2.

The third factor concerns the revelation of QE that is the probability that a photon is absorbed in the silicon. In silicon η plays a crucial role because it depends on the wavelength of the photon and its reciprocal value expresses the mean free path, i.e. the average distance travelled by a photon in a medium without suffering interactions.

Anyway, all the magnitudes of *QE* depend on the wavelength λ of the incident radiation therefore the *QE* is a function of such magnitude.

Briefly, the *QE* is expressed as:

$$QE = T(1 - \varepsilon^{-\eta x}) \quad (1.21)$$

where *T* is called the coefficient of transmission for the system air-oxidation-Silicon. The *QE* is usually expressed as a percentage.

PDE is the ratio between the number of photons detected and the number of incident photons and can be expressed as the product of three factors:

$$PDE = \varepsilon_G \cdot \varepsilon_{geiger} \cdot QE \quad (1.22)$$

where ε_G is the geometric efficiency of the SiPM, ε_{geiger} is the probability of producing an avalanche when a photoelectron impacts the detector. This term depends strongly on the voltage.

Not all the charges generated by the incident photons will create a detectable signal. That's why the *PDE* is lower than the *QE*. Also this magnitude is usually expressed as a percentage.

Dynamic of a SiPM is the maximum number of photons that can be simultaneously detected. This number is limited by the number of cells whose is composed the device. Indeed each cell emits the same amount of charge even if it absorbs at the same time more photons. Moreover, each hit cell has a "dead time" necessary for the recharge of the RC circuit made by the resistance of the quenching circuit and the capacity of the cell.

The SiPM, like all solid-state devices, have an intrinsic noise that depends on the temperature and is not due to photo-generated charges that produce the avalanche in the cells. The intrinsic noise is distinct in *dark count* and *after-pulse*.

Dark count rate is defined as the number of pulses per unit of time in absence of light. In silicon, various random statistical processes related to the temperature cause the spontaneous production of carriers. They can give rise to an avalanche crossing the multiplication area. Unfortunately, this effect cannot be distinguished from the effects produced by the events of revelation.

After-pulse is defined as the probability that a carrier is trapped in an avalanche and then is released after a certain time. The presence of impurities within the semiconductor may, in fact, produces additional levels between the bands, which constitute traps for the charge carriers, capturing and releasing them at different time. If a carrier is released from these trap level, a voltage drop sufficient to trigger the avalanche again takes place producing a phenomenon of after-pulsing after a time more or less short compared the primary avalanche.

The intrinsic noise in these devices is primarily of thermal origin.

Cross talk is the effect for which the detection of a photon by a cell causes the avalanche effect in an adjacent cell.

We have two types of cross talk.

Optical cross talk occurs during the photo-detection, when carriers forming the reverse current due to avalanche generated by the incident photon emit photons in the visible due to Bremsstrahlung, which propagate along the silicon isotropically as along the waveguides. If one of these photons reaches the active area of other pixels of the sensor and it is absorbed, it can trigger in this one an avalanche multiplication generating a spurious pulse strongly related to the absorption of the primary photon. The number of photons emitted by Bremsstrahlung effect is not very high, about 1 for 10^5 electric charges produced, but considering the proximity between the cells, the

phenomenon has a certain weight (for example, a SiPM Hamamatsu^{TM} l0xl0 μm^2 is estimated to generate 16% of measured events). This source of noise can be reduced by optically isolation of the the cells; for example, etching a channel on the border of the cell and covering it with a layer of aluminium

Electronic cross talk occurs when an electron in an avalanche spreads in a neighbouring cell through the common substrate triggering, in this one, another phenomenon of avalanche multiplication. It generates, thus, a noise spike. Also this type of cross talk can be reduced with the physical trench between cells.

The main difference between these two cross talks is observed in the case of the spurious avalanche, that in the first case generates photons and in the other electrons.

Temporal resolution is defined as the FWHM of the distribution of the time jitter (variation of temporal characteristic of a signal) with Gaussian function.

In each cell of a SiPM three parameters affect the performance time and they are:

- Collection time of the carriers in the drift region;
- Propagation time of the avalanche;
- Drift time of the electrons through the depleted region.

Among these three parameters, the second is of the order of hundreds ps and has the greatest impact. Therefore, the only limit to temporal resolution of a SiPM is given by the electronics read-out.

As for a common photomultiplier, *energy resolution* is defined by:

$$RE = \frac{\Delta q}{\bar{q}} \quad (1.23)$$

where Δq is the FWHM of the anodic charge distribution and $\bar{q}$ is the mean value of the charge itself.

The commercial SiPM, like other types of photomultipliers, are distinguishable each other by functional characteristics which can be identified by various abbreviations. The covered devices [14], for example, are identified by the abbreviation MPPC, stands for Multi-Pixel Photon Counter. The characteristics of psPM and SiPM in question are in many ways superimposed. For the benefit of SiPM should be mentioned the low voltage polarization, high PDE and the increased resolution in charge. However, in order to get the best performances the bias voltage of the devices have to be higher (OverVoltage) than that breakdown value, but this involves a drastic increase of the dark current that makes unusable devices. Among other things, the *fill factor* different from 100% is strongly limiting when a fiber is coupled to the SiPM.

This added to the property of the pixels to give the same response to a number of incident photons greater than one makes preferable the use of psPM, even more if you use devices with high quantum efficiency. A final point in favour of psPM lies in the lower cost for the same total number of channels.

1.5 Processing of the electrical signal

1.5.1 Analog to Digital converter, comparator and read-out electronics

As described in the previous paragraph, a light signal generated by a scintillator arrives on a light sensor then an electrical signal proportional to the light intensity is produced. This electrical signal needs, in turn, of a suitable electronics chain to be processed.

The read-out electronics consists of comparators to let pass signals only above a selected threshold followed by an *Analog-to-Digital Converter* (ADC), which converts the amplitude or the charge of each signal into a digital one. ADC conversion is an electronic process in which a continuously variable (analog) signal is changed, without altering its essential content, into a multi-level (digital) signal.

The input to an ADC consists of a voltage signal (i.e. the detector response) that varies among a theoretically infinite number of values. In contrast, the output of the ADC has defined levels or states. The number of states is almost always a power of two (2, 4, 8, 16, etc). The simplest digital signals have only two states and are called binary. All whole numbers can be represented in binary form as strings of ones and zeros.

Digital signals propagate more efficiently than analog signals, largely because digital impulses, which are well defined and orderly, are easier for electronic circuits to distinguish from noise, which is chaotic. This is the main advantage of digital modes in communications. Computers "talk" and "think" in terms of binary digital data; while a microprocessor can analyze analog data, it must be converted into digital form for the computer to make sense of it.

After a selected trigger signal to start the acquisition, ADC begins to collect data from each channel in an appropriate integration period. The data collected for each channel are then stored into a data acquisition PC by appropriate software, performing also the data triggering and a pre-analysis. Considering a tracking detector made of planes of scintillating fibers (such as the one described in Chapter 2), as a trigger condition you can require, for example, the coincidence of the signals in both ends of a fiber and, in a defined gate, all the coincidences for all the detector planes.

1.6 Tracks reconstruction

1.6.1 Reconstruction algorithms

After acquiring data on the impact points of a particle on tracker plans, it is necessary to use some algorithm to reconstruct the particle tracks.

The task of track reconstruction is traditionally divided into two different subtasks: *track finding* and *track fitting*.

Track finding is a pattern-recognition or a classification problem and aims at dividing the set of measurements in a tracking detector into subsets. Each subset contains measurements that may be originated by the same particle. These subsets are called track candidates. An additional subset contains measurements believed not to come from any of the interesting tracks, but for instance from noise in the electronics or from low-energy particles spiraling inside the tracking detector. Track finding should be conservative and keep a track candidate in case of doubt rather than discarding it, because it is impossible to recover a track candidate discarded at this stage at any following stage.

The track fit takes the set of measurements in a track candidate as a starting point. The goal is to estimate as accurately as possible a set of parameters describing the state of the particle somewhere in the tracking detector, often at a reference surface close to the particle beam. With very few exceptions [15], the estimation is based on least-squares methods. The track fit should be as computationally fast as possible, it should be robust against mistakes made during the track finding procedure, and it should be numerically stable.

The track fit is also used to decide whether the track candidate hypothesis is valid. Such a test can be based on the value of the χ^2 statistic, i.e. the sum of the squared standardized differences between the measured positions in the track candidate and the estimated positions of the track at the points of intersection of the detector devices. If the value of such a statistic is too high, the set of measurements is not statistically compatible with the hypothesis of having been created by a single particle. The reason for this incompatibility could be a single or a few measurements in a track candidate misclassified by the track finding, or a track candidate being completely wrong in the sense that it is a random collection of measurements originating from several other particles, so-called ghost tracks. The track fit, in this testing phase, should be able to remove wrong or outlying measurements in the track candidates and suppress the ghost tracks completely.

In experimental conditions such as those found in the LHC experiments, many of the measurements are either noise or belonging to particles with too low energy to be interesting from a physics point of view. Therefore, many hypotheses have to be explored in order to find the set of interesting track candidates, and track finding can in general be a cumbersome and time-consuming procedure. Computational speed is an important issue, and the choice of algorithms may be dictated by this fact. Track finding often uses the knowledge of how a charged particle moves inside the bulk of the detector, the so-called track model, but can resort to a simplified version if time consumption is critical. The use of simplified track models is particularly important for triggering applications, where track finding is part of the strategy applied in the online selection procedure of interesting events.

CHAPTER 2
THE OFFSET3 TRACKER

2.1 Introduction

Research and development of hadrontherapy for the cancer treatment is continuously growing, because of the increasingly strong social needs. In the treatment of cancer, the advantage of employing charged particles, such as protons or carbon ions, is related with a better control of the amount of released energy compared to conventional radiotherapy, while preserving the surrounding healthy organs and tissues. Furthermore, the direct knowledge of the energy loss by a particle that interacts with the tissue, said *stopping power* of the particle, provides much more accurate information on the delivered dose than X-ray tomography and allows to check the correct positioning of the patient too. Starting from these considerations, the necessity to use detectors capable of providing real-time images of the area to be treated is crucial.

In this chapter, the design and characterization of a charged particles tracker, the *OFFSET3* detector *(Optical Fiber Folded Scintillating Extended Tracker)* are presented, compared with the characteristics of a previous prototype *OFFSET* [16].

The main goals of *OFFSET3* are to obtain the images and the tracks of charged particles in real-time with high spatial resolution and low complexity in order to apply it in medical imaging.

It can be used, for example, for an accurate positioning of the patient and for the characterization of the beam, i.e. the measurement of the beam specifications, such as uniformity and penumbra, useful for an accurate treatment of tumors.

OFFSET3 was created using basically the same operation principles of the previous model, but refining the technology applied, the details of design and expanding the possible applications. The main difference consists in the number of tracking planes. In fact, while *OFFSET* is made from a single tracking plane X-Y, *OFFSET3* is a complete tracker of charged particles, with a greater sensitive area (288x288 mm^2) larger than the one of OFFSET (200x200 mm^2) making the former detector suitable for several applications in medical imaging.

In addition, the innovative read-out strategy allows a considerable reduction in the number of optical channels to be coupled to the photo-sensor. The two *OFFSET3* tracking planes are made using only two ribbons of scintillating fibers and then the signals are decoded in an appropriate way. Thanks to this mechanism of reading, it is possible to reconstruct the track of a particle that crosses the sensitive area of *OFFSET3* in real-time, to the benefit of cost and complexity.

Moreover, the small size of the associated electronics facilitates the integration of the detector in a treatment chamber for hadrontherapy.

Another great advantage is the ability to test the *OFFSET3* detector with various sources, such as cosmic rays and ^{90}Sr and ions beams.

The measurement of the performances in a real testing environment have been done with 60 MeV and 250 MeV protons and 400 MeV/A clinical carbon beam, available at the *Center for Advanced Nuclear Applications and Hadrontherapy* (CATANA) in the *Laboratori Nazionali del Sud* (LNS) of Catania (Italy) [17] and at the *Centro Nazionale di Adroterapia Oncologica (*CNAO) of Pavia (Italy) [18].

2.2 The first OFFSET prototype

2.2.1 Architecture

The design of the *OFFSET* detector started in the year 2010 with the namesake research program *OFFSET*. The detector is made of one single tracker plane X-Y, obtained as a superimposition of two layers of Sci-Fis orthogonal one to each other. The fibers are pre-glued and aligned in ribbons by the producers. The sensitive area of 20x20 cm^2 was built employing 500 μm squared multi-cladding BCF-12 Sci-Fis, manufactured by Saint-Gobain [19]. When a particle hits a fiber, an isotropic emission of scintillation light is produced inside due to the energy released by the particle. A part of this light remains inside the fiber, which guides it toward the ends, thanks to a mechanism of total internal reflection.

Several studies have been carried out on the fibers properties, i.e. the attenuation length in function of the cross section, optical properties, etc. The attenuation length function has two exponential decay components, as shown in eq. 2.1 [20-21].

$$I(x) = Ae^{-\frac{x}{\lambda_1}} + Be^{-\frac{x}{\lambda_2}} \quad (2.1)$$

in which x is the distance traveled within the material, I is the intensity of the scintillating light produced by a crossing particle, λ_1 and λ_2 are respectively the short and long attenuation lengths, characteristics of each fiber.

Typical values for λ_1 are of the order of tens of centimeters and for λ_2 of about one meter. Starting from these quantities, the position where the light has been produced in the fiber can be determined measuring the light output at the opposite edges of one fiber.

Many technical constraints limit the maximum reachable dimensions of the sensitive area. As reported in [22], the attenuation length measured for the BCF12 fibers, with a squared cross section and 500 μm thick, is about one meter. λ_1 is the dominant component for our application.

Choosing a maximum length of the Sci-Fi equal to the attenuation length of one meter, one can evaluate the maximal possible dimensions of the sensitive area, taking also into account the length of scintillating fiber needed for routing to the optical sensor. The optimal scintillating fiber length can be estimated fixing the bending radius and

considering the path from the last fiber of the ribbon to the opposite edge of the sensitive area (see Fig. 2.1). The maximum possible size for the sensitive area, calculated in this way, is about 45x45 cm^2. The dimensions of the *OFFSET* tracker are well below these limits.

We have arranged two ribbons of 400 fibers each into orthogonal layers, one above the other, kept in position by the pressure of two square aluminium frames delimiting the sensitive area of the detector. Figure 2.1 shows a picture of the final detector without cover. Routed clear fibers are also visible outside the sensitive area. The total size of the device, including the mechanical structure, is 70x100 cm^2 while the sensitive area is only 20x20 cm^2.

Considering a classical read-out scenario, every Sci-Fi has to be optically coupled to a light sensor and the signal is recorded by a single channel of the front-end electronics. In *OFFSET* prototype there are 800+800 channels (800 for each layer), considering the coincidence between the signals coming from both edges of each Sci-Fi. A suitable read-out system would not only be complex but also expensive. Instead, we plan a read-out solution that is a good compromise between cost and dead time.

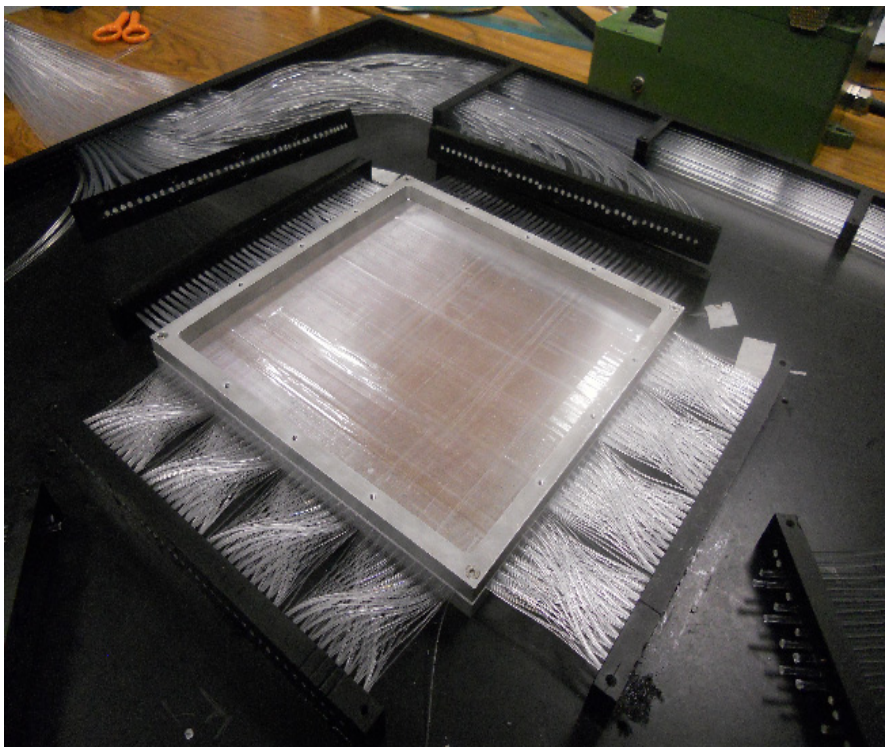

Figure 2.1 - The OFFSET tracker sensitive area is shown, without the cover. The whole dimension is 20x20 cm^2 and it's made of Sci-Fis. The clear fibers routing, out of the aluminum frame, are also shown.

2.2.2 Collection of the Scintillation Light: the Photosensor

In order to collect the scintillating light from the fibers, a single multianode photomultiplier (PSPM) was chosen as a light sensor: the 16x16 pixels H9500 PSPM Hamamatsu photomultiplier [23]. It needs only a single high voltage power supply to

provide a signal for each pixel, and one additional signal, called the dynode signal, obtained by adding all the signals of the last dynodes of all the PSPM channels. Groups of ten Sci-Fis are coupled to a clear fiber one meter long, which in turn is directly coupled in front of a PSPM pixel. Optical gel between the Sci-Fis and clear fibers assures a good optical coupling. The number of Sci-Fis coupled to one clear fiber is determined by the pixel size of the selected photomultiplier, which is about 2.8x2.8 mm^2. This limits the maximum possible cross section of the selected clear fibers.

2.2.3 Front-end and read-out electronics

Thanks to a simple digital acquisition system, the signals from the detector are processed. The PSPM is accommodated into a front-end board and each anode is directly connected to one of the four inputs of a MAX964 comparator [24] shunted by a suitable resistor. The value of its resistance was selected for all channels as a good compromise between the amplitude and timing characteristics of the anode voltage signal [25]. The selected value was 200 Ω.

As a consequence, a single signal of photoelectrons with a gain of $2x10^6$ has an amplitude of 5 mV and about 8 ns Full Width Half Maximum (FWHM). The output signal from each comparator is then sent to a monostable, which gives 100 ns stretched logical output. The signal from the monostable influences the efficiency of the detector for events with a rate greater than 10 MHz. Each of the 160 outputs of the front-end board is then transmitted to a data acquisition board by shielded cables. A common threshold for the comparators is set at about a third of the single photoelectron mean peak amplitude.

A customized board was realized to perform shaping, pre-analysis and storage on a PC of the comparator signals. Then, they are sent to a real-time data acquisition module, the FPGA PXI-7813R [26] with 160 digital inputs/outputs. The signals can be sampled up to 40 MHz and the module supports real-time analysis and Direct Memory Access (DMA) transfer to mass storage. Thanks to the real-time analysis it is possible to distinguish between single and multi hits events and identify the X-Y position. The chosen 25 MHz sampling rate justify the stretched comparator outputs of 100 ns. In addition, this sampling frequency allows to distinguish two events whose arrival time differs more than 40 ns. The jitter of the arrival time due to the PSPM, fibers and noise, gives a negligible contribution (< 1 ns). A goal for our system is the achievement of an acquisition rate of 1 million of events per second so it must be found a compromise between the average particles rate and the acquisition rate [6]. From the calculations, taking into account the Poisson distribution of the arrival times of particles, at an average rate of 1 MHz rate the acquisition efficiency is about 90%. However, the data acquisition board, PXI-7813R, has a limitation in the data transfer bandwidth and as a consequence it was decided to work at 300 kHz average event rate. A real-time module, a PXIe-8102, is interfaced to the PXI-7813R through the PXI bus. The PXIe-8102 manages the DMA and the PXI bus, the Ethernet communication for the remote host control and data processing thanks to its real-time operating system. Finally, the PXIe-8102 stores data to a solid-state hard disk. The PXI-7813R monitors continuously the 160 digital input lines. The trigger condition consists in the identification of a pattern of

at least 4 coincident high logic signals. A firmware and suitable data acquisition programs for the *OFFSET* tracker read-out, analysis, display and control by LabVIEW platform, are developed for our purposes.

Using a better performing data acquisition module and eliminating the 100 ns signal stretching, it would be possible to increase the acquisition rate up to 100 MHz, which is the rate when significant overlaps between the PSPM signals of different events would occur.

2.3 The new OFFSET3 detector

2.3.1 New Detector Design Idea

After evaluating the good performances of the *OFFSET* prototype, it was decided to build a real tracker that could harness the same technological innovations of the previous model: *OFFSET3*. The Sci-Fis are provided by the manufacturer in pre-glued and pre-aligned ribbons of 576 fiber, each 1300 mm long.

Two tracking planes are obtained by curving the ribbons, with the suitable bending radius as shown in Figure 2.2. The curved portion of the ribbon must guarantee a simple discrimination between the signals at the edges. The length of the curved portion of the ribbon is fixed by the bending radius as the result of the comparison between the first exponential decay component (λ_1 of about 10 cm) and the optimal bending radius (about 5 cm).

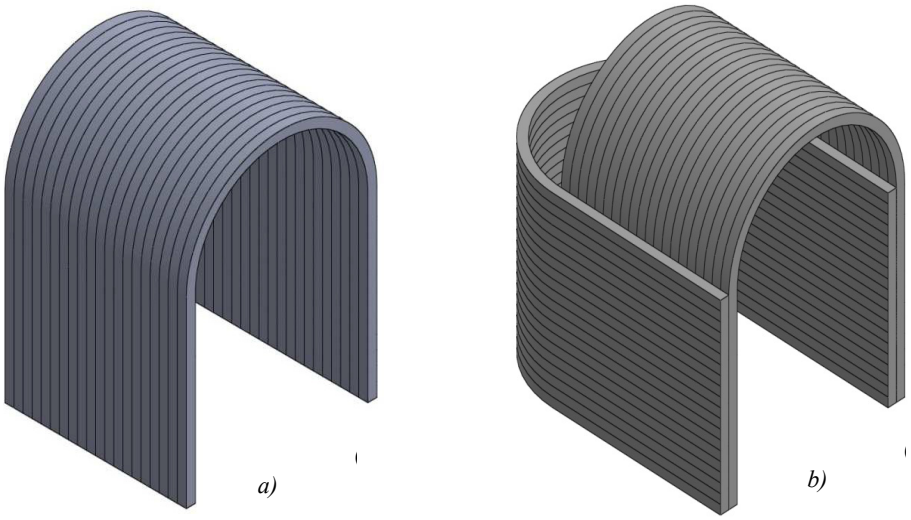

Figure 2.2 - Tracker layout, made by using two suitably folded tapes, as shown in (a) and rotated 90° as shown in (b), in order to obtain a 2D tracker.

In this way, these two tracking planes (the front and back planes) have the same number of optical channels needed for a single one. The hit is decoded by measuring the light output in bound coincidence at both edges of each fiber.

If a particle crossing the two Sci-Fis ribbons hits two different fibers, one per plane, four signals in a very small time interval are produced and arrive at the end of the fibers in a bound coincidence. The arrival time interval is due to the propagation time of scintillation light along the fiber, and it is typically 5 ns per meter of fiber.

A picture of the final detector is shown in Figure 2.3.

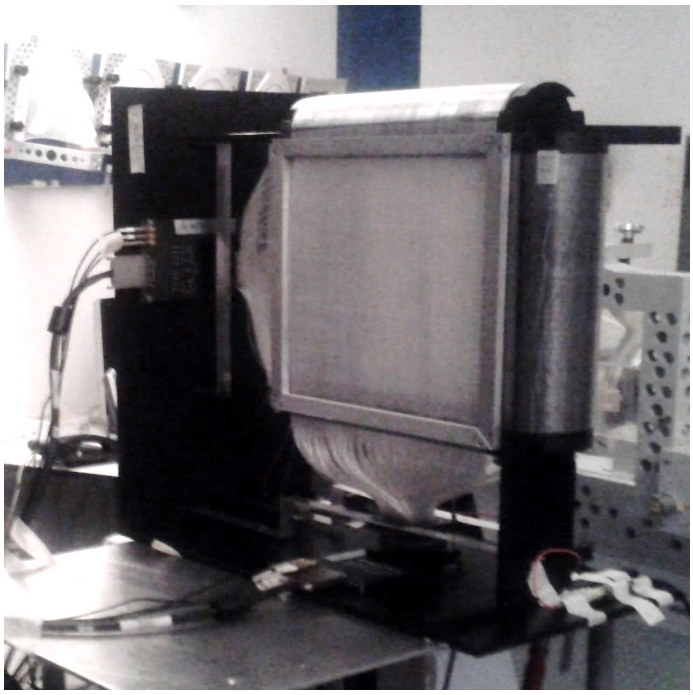

Figure 2.3 - Picture of the OFFSET3 detector.

The two mutually orthogonal X-Y layers of one plane, with the 288x288 mm^2 sensitive area, spaced by 100 mm are clearly visible. The resulting spatial resolution is of 500 μm/$\sqrt{12}$ (calculated as for a segmented detector). The tracker corresponds to 2 mm water equivalent thickness and the maximum acquisition rate of 5 MHz is limited by the read-out electronics sampling frequency.

2.3.2 Application of The Smart Read-out Strategy

A further reduction of the optical signal number to be read is given by the application of the read-out channel reduction system to the ribbon edges [6].

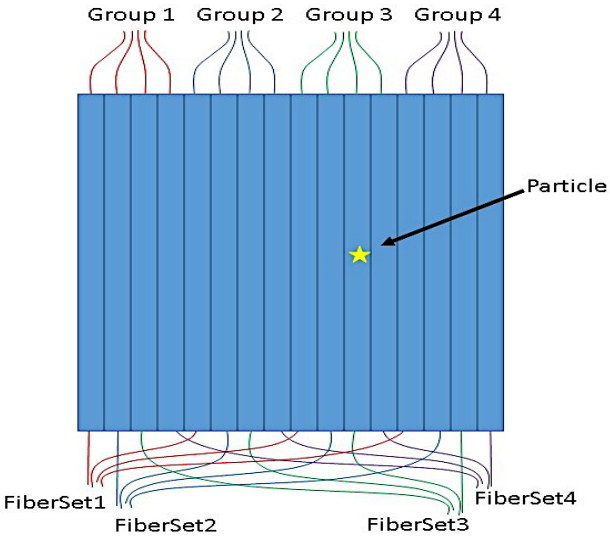

Figure 2.4 - Scheme of the channel reduction system.

This system, already described in Section 1.2.3 can be reassumed as follows.

Each fiber is read from both ends, but the meaning of the two signals is differently interpreted, as a result of different groupings, from the two edges.

At one end, the fibers are read together in *Groups* of *n* contiguous fibers, while at the other end the first fibers of each group are grouped in *FiberSet1*, the second fibers of each group in *FiberSet2*, and so on. A particle crossing one fiber generates two signals at both ends, one from the i^{th} *Group* and another from the j^{th} *FiberSet.* Their combination can uniquely identify the fiber hit by the particle ($Fiber_{hit}$), according to eq. 2.2:

$$Fiber_{hit} = (i-1) \times n + j \quad (2.2)$$

In the example shown in Fig. 2.4, the fiber at the point of impact, marked with a star, is the 11^{th} fiber.

Using a simple calculation the final number of channels to be read-out in the general case without reduction is equal to $4\sqrt{N}$, where N is the total number of fibers in the ribbon. When N is large, the reduction factor becomes significant, especially in favour of real-time applications.

The bound coincidence between the ends of each strip, not present in a simple read-out system, allows spurious signals (noise, crosstalk, dark current, etc.) to be automatically filtered.

The fibers, grouped as in the scheme of Figure 2.4, can be directly coupled to a suitable photo-sensor, and the current pulse, which corresponds to scintillation light, will be proportional.

The maximum reduction factor of the read-out channels is obtained with the number of fibers in the Groups equal to the number of fibers in the *FiberSet*, given by the square root (n_{opt}) of the total number of fiber in the ribbon.

The number of fibers in the ribbon is fixed once the size of the sensitive area and the size of the fiber section have been chosen.

The coupling of the group of fibers to the photo-sensor implies that the sensitive surface of the single photo-sensor must be greater than the surface of the grouped fibers, which is n_{opt} times the section of the fibers.

Following the read-out channel reduction scheme reported in the Figure 2.4, for a particle crossing one fiber in the front plane and one different fiber in the back plane, two signals will be measured at each edge. To decode this information at each edge, the signal coming from the front plane must be discriminated by the signal of the back plane. But it is important to consider the different amplitudes of the two signals.

For example, the fiber hit in the front plane will produce a higher *Group* signal than the rear one, due to the lower distance from the edge, while the fiber hit in the back plane will produce a higher *FiberSet* signal respect to the front one.

The application of the reduction channel technique doesn't involve any loss of information and in addition provides a mechanism of coincidence that makes the detector substantially immune to noise.

2.3.3 Collection and Detection the Scintillation Light

A. Photosensor

Two *Position Sensitive Photo-Multipliers* (PSPM) are used for the collection of the scintillation light.

The chosen type is the multi-anode photomultiplier H8500 with 64 anodes, manufactured by Hamamatsu. A picture is shown in Figure 2.5.

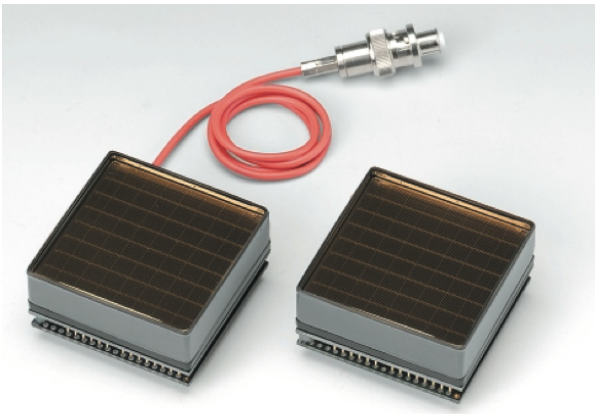

Figure 2.5 - PSPM H8500 by Hamamatsu. The device has 64 anodes.

B. Front-end electronics

The front-end electronics consists, for each direction, of a full-custom board (FEB). In each FEB are located the photosensors H8500 PSPM and an array of fast comparators; the 64 analog PSPM outputs are compared to a single settable threshold generating logical signals from which it is possible to determine the fibers crossed by particles.

Then, the 64 digital signals are sampled at 200 MHz by an acquisition board, based on FPGA manufactured by National Instruments [26]. As for the *OFFSET* prototype, the comparators threshold is set at about the third of the mean amplitude of the single photoelectron.

The hit fiber is identified in a few tens of nanoseconds and the hit point position can be displayed in real-time on the screen of a PC.

Two FEB, one for each direction, are read-out simultaneously by the data acquisition board which stores data only for quadruple coincidences in each plane, remove the dark current signals produced by the PSPMs, and send them to a real-time system where they will be processed, stored and displayed. The resolution target is the capability to distinguish between the greater and the lower signals, with the technique Time Over Threshold (TOT). It consists in comparing the analog signals (for our purpose the 64 PSPM outputs) to a suitable threshold and counting the number of clock cycles for which the comparators outputs have a high level.

As mentioned before, the lower attenuation length is dominant in the range of lengths of interest for the construction of detectors. For example, the optimal bending radius for scintillating fibers with circular cross-section and diameter 0.5 mm is 50 mm (100x). The bent portion of the ribbon is long π times the bending radius. This value corresponds to about three times the lower attenuation length, and therefore the attenuation introduced by the bending will be larger than 1/e.

Since the output signals at the two ribbon ends are different in amplitude, because of the scintillation light attenuation in the path inside the fibers, it is possible to reconstruct the x and y coordinates of the impact point just associating the fiber *Group* and *FiberSet* to each hit.

C. Read-out electronics

The read-out system uses the National Instruments LabVIEW platform [27].
A crate, model NI PXIe-1062q, houses the NI PXIe-8135 real-time module and the PXIe-7962R, a fast read-out board based on programmable logic FPGA.

In addition, a full custom adapter module, which acts as an interface between the read-out FPGA board and the fast comparators array in the FEB is developed.

It is a simple printed circuit board (PCB) and the connection is performed by a National Instruments cable. Gigabit Ethernet communication connects the system to a PC for visualization.

2.4 Detectors tests with Cosmic rays and Beta Sources

2.4.1 OFFSET

Performances were studied thanks to intensive experimental tests by using different sources, such as cosmic rays, beta sources and a 62 MeV proton beam.

Particles employed to study the detector response were firstly beta sources and cosmic rays, which, as Minimum Ionizing Particles (MIP), produce a low level of scintillation light.

Measurements confirm that the detector is sensitive to beta particles and then it could be used for the characterization of *OFFSET* if no ion beam is available.

The exposure of *OFFSET* to cosmic rays is uniform over the entire sensitive area of the detector. Notice that a 250 MeV proton beam for medical imaging deposits an equivalent energy of 2 MIP in *OFFSET*. Figure 2.6 shows the *x* and *y* projections of the cosmic rays image acquired in 47 hours. The histograms provide information about the uniformity in the detector response.

Four groups of ten Sci-Fis are absent in the image. This is due to the failure of the corresponding front-end channels. Some lines in the *x* and *y* directions are also missing for the same reason as in the case of the test with beta sources. Standard deviations of hits on single fiber respect to the average value are 27.2 % for *x* projection and 27.0 % for *y* projection. The non-uniformity in the detector response is mainly due to the different optical coupling between the fibers and the PSPM and also to the different gains of the PSPM channels.

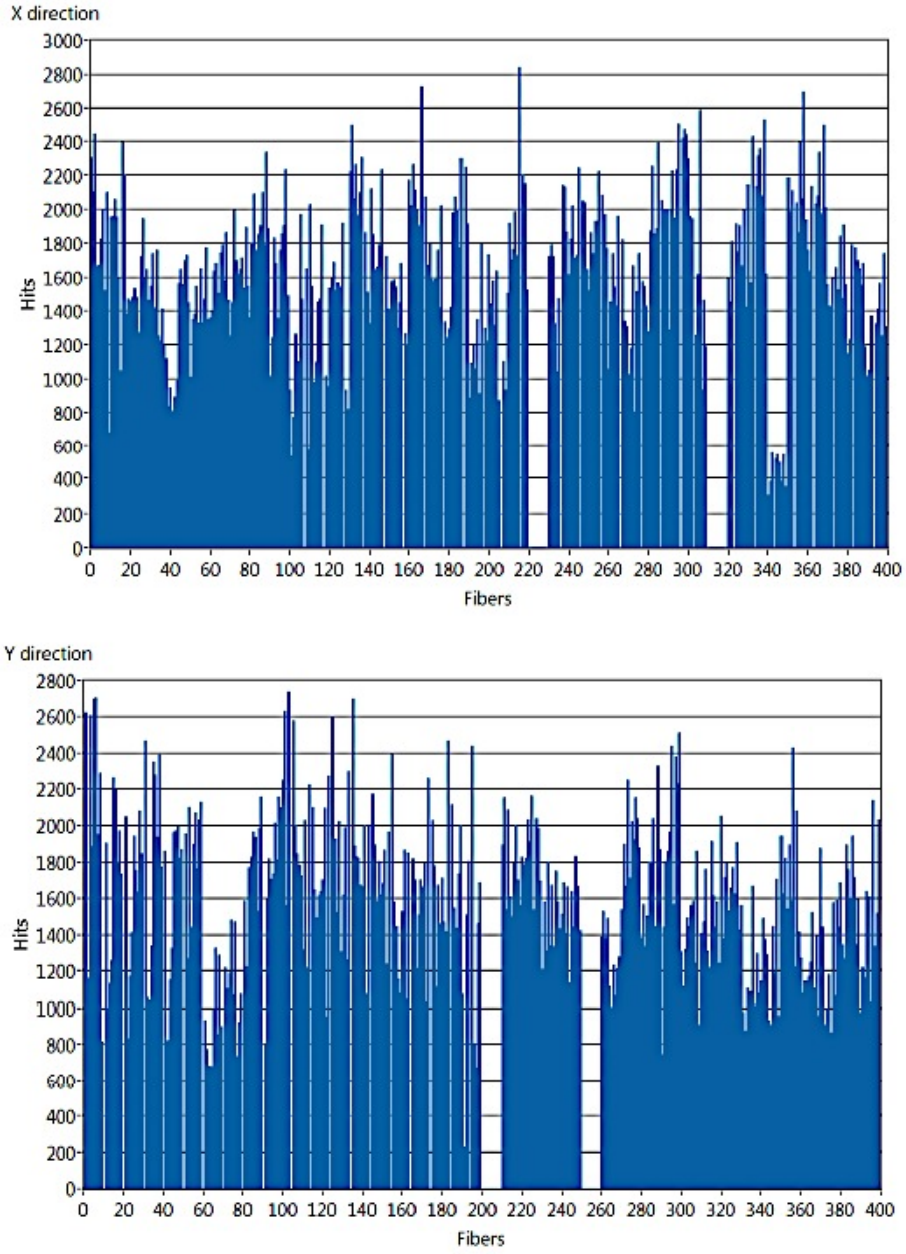

Figure 2.6 - Histograms for the *X* and *Y* directions of cosmic rays acquired by the OFFSET tracker.

2.4.2 OFFSET3

As for *OFFSET*, also the *OFFSET3* detector was tested with β sources and cosmic rays. It is important to remember that β particles produce a low level of scintillation light. Figure 2.7 shows the images of a ^{90}Sr β source with an activity of 3 kBq and a diameter of about 2 cm. It was obtained by moving the source, placed closely in front of the sensitive area of the front detection plane, in three different positions.

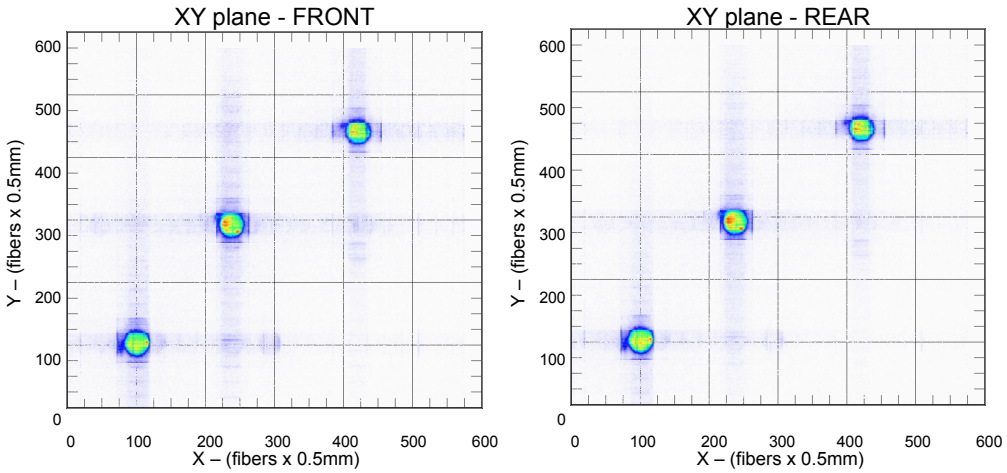

Figure 2.7 - Images of a ^{90}Sr β source by the OFFSET3 detector.

Another important test is the one with MIP cosmic rays because they irradiate uniformly over the entire sensitive area of the detector, but delivering a small amount of energy. Figure 2.8 shows a map of cosmic rays acquired by the detector.

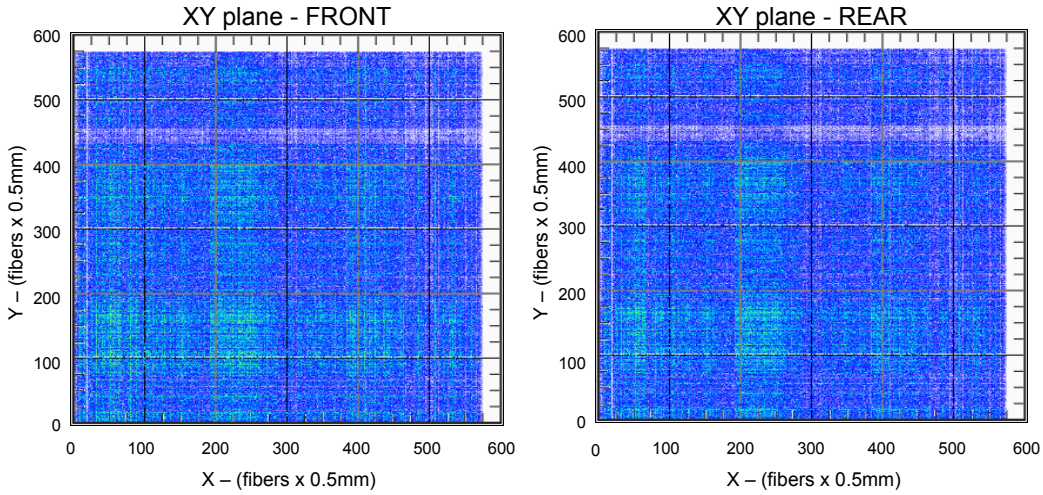

Figure 2.8 - Images of a map of cosmic rays.

The map in Figure 2.8 also provides an estimation of the uniformity of response of the detector, and was used to calibrate the images obtained with the beta source shown in Figure 2.7. The calibrated beta images are shown in Figure 2.9.

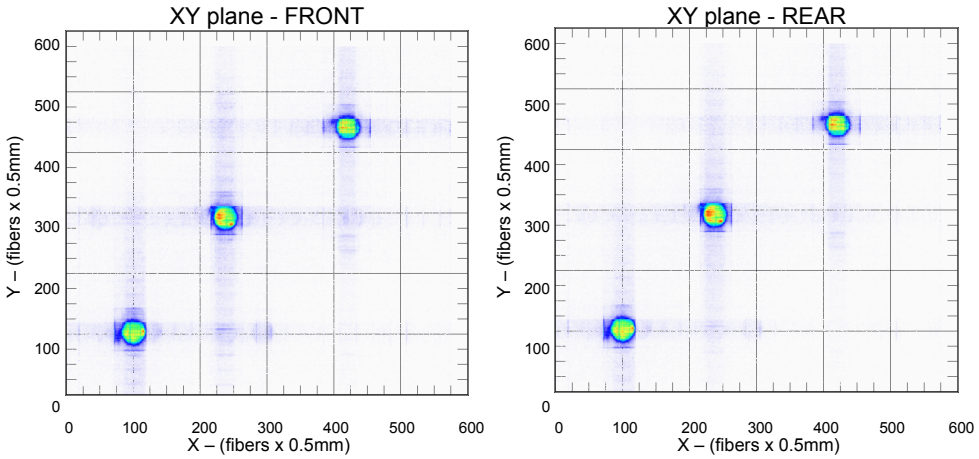

Figure 2.9 - Calibrated images of a ^{90}Sr β source by the OFFSET3 detector.

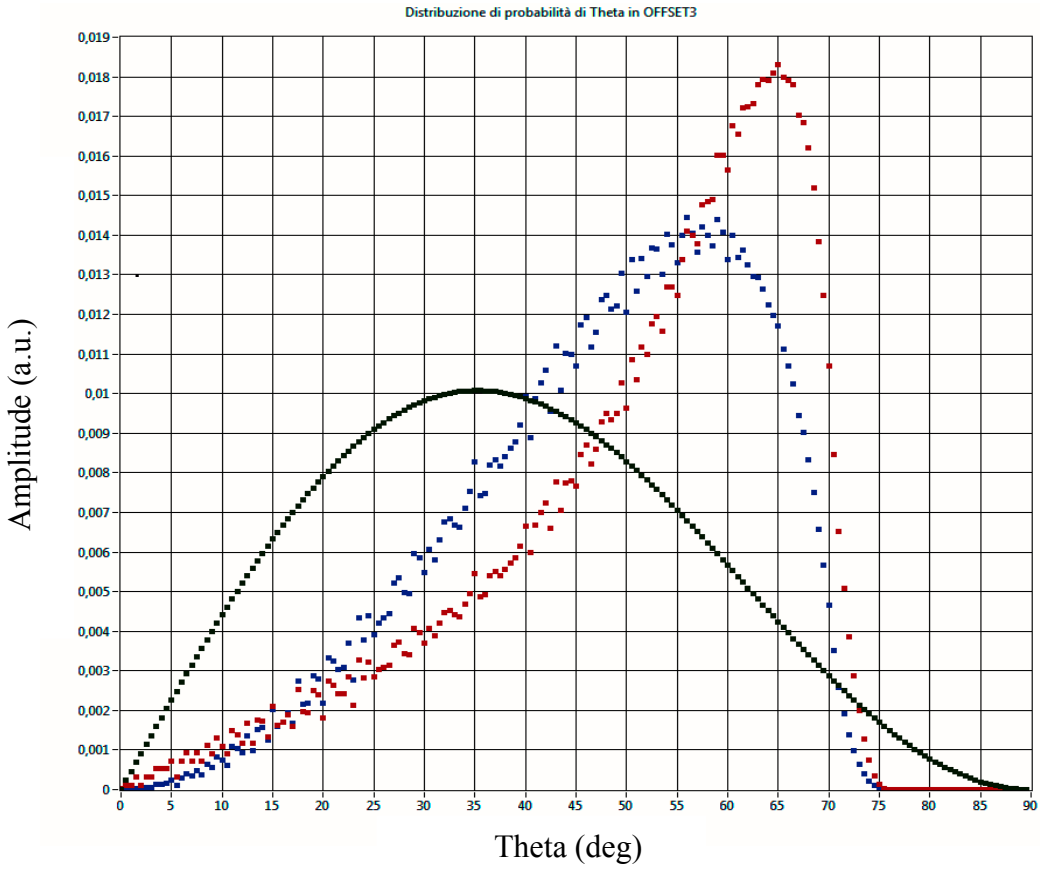

Figure 2.10 - Normalized angular probability distributions of cosmic rays (green dots) and of the angular acceptance of the detector (red dots). The probability to detect cosmic muons by the detector is also shown (blue dots).

We can employ beta particles and cosmic muons for the characterization of the *OFFSET3* detector in absence of a beam. Considering that 250 MeV proton beam for medical imaging deposits an energy equivalent of about 2 MIP in *OFFSET3*.

The maximum detection angle calculated from the *OFFSET3* dimensions is about 76°, with respect to the normal to the detection planes.

From literature [28], the angular distribution of cosmic rays crossing a spherical surface, shown in the green dotted curve in Figure 2.10, is given by the eq. 2.3:

$$D_{\mu}(\theta) = cos^2(\theta)sin(\theta) \quad (2.3)$$

However, the real detector has not a spherical shape and the number of detectable corners, given by the combination of each crossed pixel of the front plane with each pixel of the rear plane is calculable. Considering the single pixel side of 0.5 mm, each XY plane contains the number of pixels resulting from eq. 2.4.

$$Npixel_{sp} = 576\text{x}576 = 331776 \quad (2.4)$$

As a consequence, the permits combinations of angles, of the order of 10^{11}, have the angular distribution shown by the red dotted curve in Figure 2.10 *(D_{O3} (θ))*.

Both the green and the red dotted curves have normalized area: the green curve represents the probability for a muon to pass through the detector at a certain angle, and the red one shows the probability for a particle crossing the detector, to provide a track with a certain angle.

Consequently, the probability for a muon, crossing the plains with a certain angle, to provide a detectable track, is influenced by both curves mentioned above. The final trend is shown by the blue curve in Figure 2.10, obtained from the product of the two distributions, normalized in area, eq. 2.5.

$$D_{O3\mu}(\theta) = D_{O3}(\theta) * D_{\mu}(\theta) \quad (2.5)$$

Do not taking into account the dead space due to the cladding, non-uniformity due to optical couplings and the response of front-end electronics the curve represents the ideal response of the *OFFSET3* detector to the cosmic rays.

A measurement campaign of about three weeks was carried out in order to calculate all the particles tracks angles with respect to the normal to the detector planes. The obtained distribution, normalized area, is shown by the red curve in Figure 2.11.

The repetitions, i.e. data concerning the same ribbon for the upper and lower plane, were removed to avoid misinterpretations of a strongly angled track (without one of the two *Groups* information) and almost vertical tracks (where the *Group* information is usually only one). In any case, usually, it is a negligible number. The data of the red curve of the histogram below 10° shows this cut. The blue curve represents the ideal response of the *OFFSET3* detector to the cosmic rays.

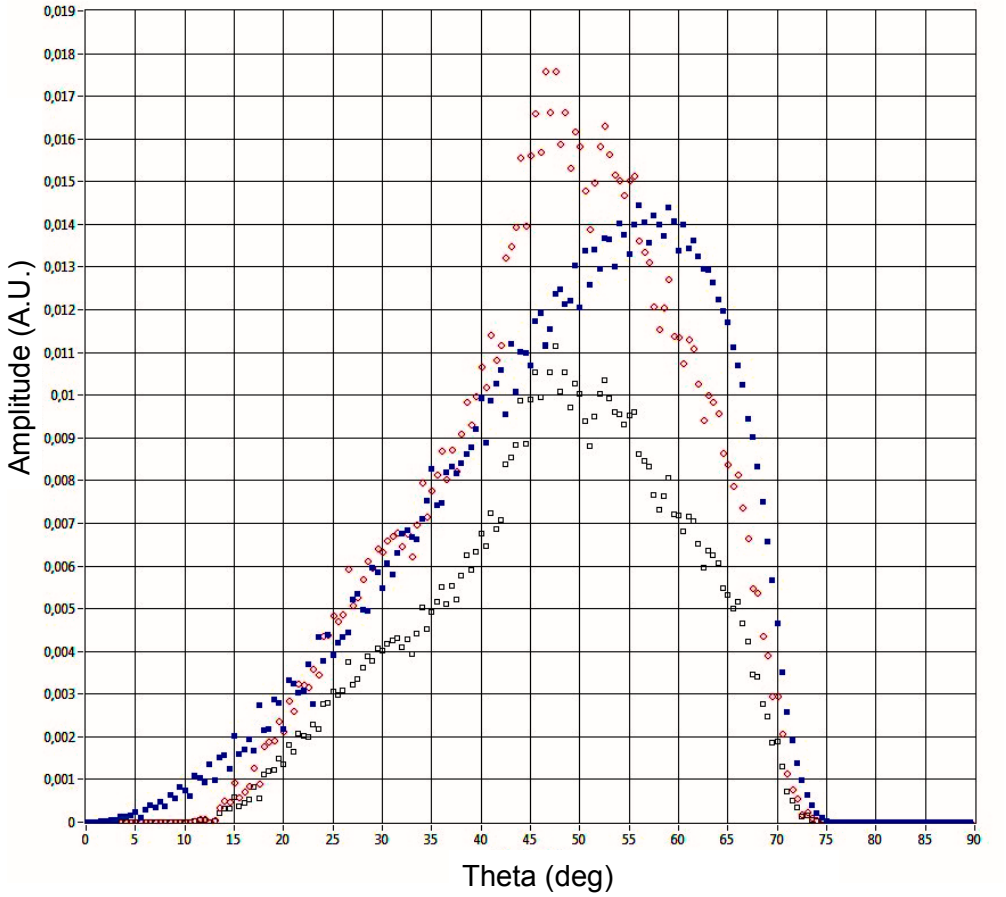

Figure 2.11 - Normalized distribution of all the experimental angles with respect to the normal to the planes (red dots), The probability to detect cosmic muons by the detector (blue curve), scaled red data (green curve).

As it is clearly visible from the Figure 2.11, despite the shape of the two curves is quite similar, if the detector efficiency is unitary, there are some angles in which the normalized responses of the real detector is more than the ideal one (blue dots). It is realistically expected that for each considerable angle, the detector could response, at most, as the ideal model. Then, the plot (red curve) was scaled by an additional factor, so that this condition is satisfied (green curve).

It's possible to estimate the detector efficiency for muons by calculating the ratio of the areas under the two curves that is equal to about 64%. This value seems quite reasonable considering that the detector efficiency would be about 85% of the real total muon rate, due to the presence of the cladding on the fibers. An additional difference may be due to non-uniformities of the optical couplings and gain of the PSPM anodes. A new FEB under construction will give the possibility to correct some dis-homogeneity by varying the threshold for each FEB channel individually.

2.5 Tests with 62-250 MeV protons and 400 MeV/A CNAO clinical beams

2.5.1 OFFSET

Both detectors were tested with 62 MeV proton beam in the CATANA facility at the LNS in Catania.

During an experimental run on March 2013, the CATANA staff performed a beam profile characterization (Figure 2.1) along both the *x* and *y* directions with calibrated diodes, before starting the measurement with the OFFSET tracker. Then, during a run of about 60 min performed applying a 1.5 cm diameter hole calibrated collimator, a total dose of 1.2 Gy was accumulated. The target was to acquire in real-time an image for each minute of the beam after the collimator, and accumulating a 2D histogram the occurrences of reconstructed tracks over the considered time. Having a proton rate of about 300 kHz, an image with sufficient statistics, about 1 million of events, was acquired in 3 seconds. A gafchromic EBT3 film [29] was placed in front of the sensitive area crossed by the proton beam to calibrate the detector. Figure 2.12 shows a sketch of the experimental setup.

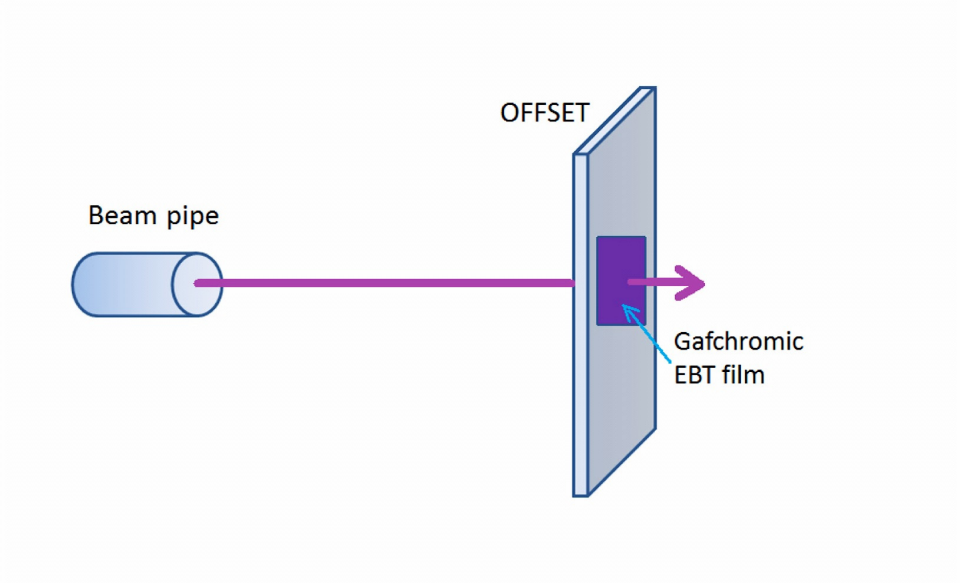

Figure 2.12 - Sketch of the experimental setup.

In detail, the calibrated gafchromic EBT3 film was digitized by a scanner and the final dose distribution was used to calibrate the region of the *OFFSET* sensitive area that intersected with the beam. For the calibration of the images acquired by the *OFFSET* detector two assumptions have been done: a linear response of the scintillating fiber with respect to the delivered dose in the selected dose range and the same efficiency of each detector pixel.

The calibration was performed by summing, for each pixel, all the images

acquired with *OFFSET*, supposing that a non-uniformity in pixels response of the sensitive area is time invariant. In this way a calibration matrix is obtained and provides relative correction factors for each pixel of the *OFFSET* tracker.

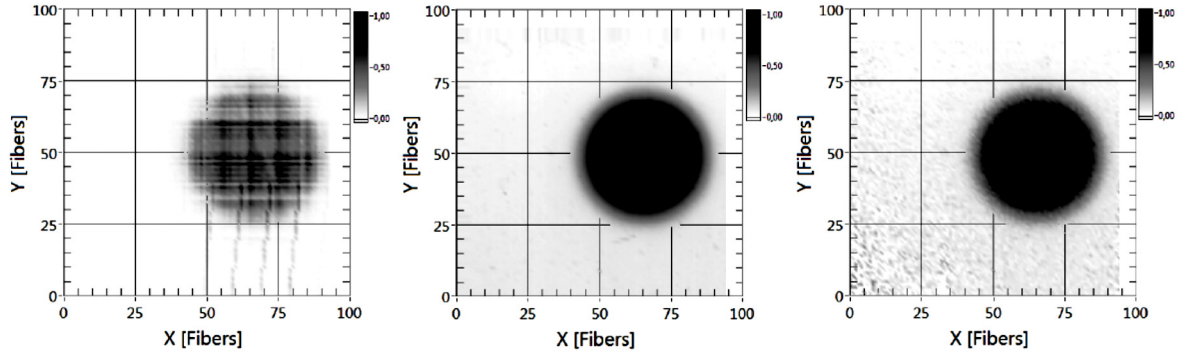

Figure 2.13 - Images obtained with a 62 MeV proton beam: (left) the raw sum of all the images recorded with OFFSET; (center) the gafchromic EBT3 film image; (right) the sum of all the frames acquired by OFFSET, after calibration. Axes are in fiber number (one fiber has a diameter of 500 μm).

Non-uniformities in detector response are corrected by mean of the calibration matrix. They are due to in-homogeneities in the optical coupling between the fibers and the PSPM and non-uniformity of the PSPM gain. Thanks to the repair of the front-end board, there aren't missing fibers groups, despite of the measurements with beta particles. The results of the test with protons are shown in Figure 2.13. It's evident the improvement in uniformity with respect to the measurements with cosmic rays and the beta source. The two profiles of the beam after the collimator, in the *x* and *y* direction, are extracted from the *OFFSET* calibrated frames and the gafchromic image. The profiles are normalized to the center axis and interpolated with a linear function. Penumbra and field size are calculated on the profiles. The penumbra is defined as the distance in mm between the points corresponding to 20% and 80% of the dose value on the central axis, while the size of the field is defined as the distance in mm between the points corresponding to 50% of the dose values. Further analysis is in progress to characterize uniformity and symmetry of the image. After calibration, each one-minute frame recorded with *OFFSET* was analyzed in order to perform a beam profile characterization as a function of time. In order to verify the reliability of the calibration, an additional run of measurements has been carried out. The delivered dose was about 1.6 Gy and it was used an eye-shaped collimator (usually employed during a proton therapy treatment, according to a tumor shape).

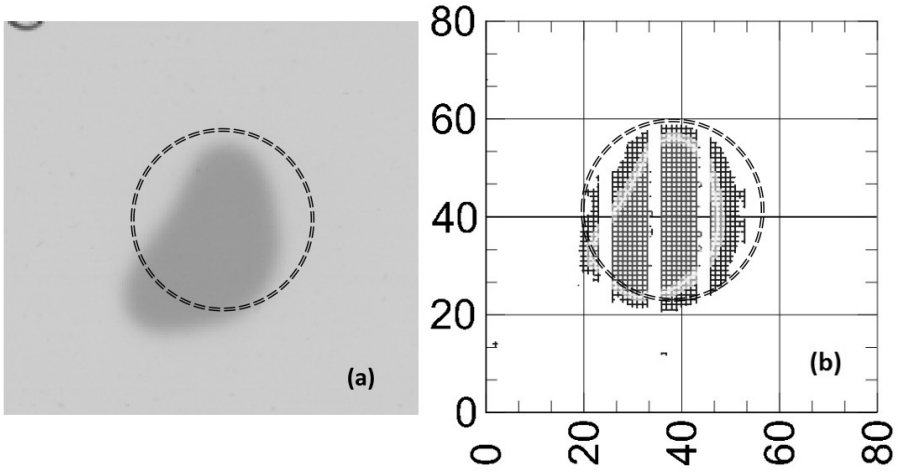

Figure 2.14 - Gafchromic EBT film image, (b) the eye-shaped image, calibrated. Axes report the fibers number (fiber size 500 μm).

The same calibration matrix obtained in the previous measurement with the proton beam was used to correct the image of the eye-shaped collimator. The results are shown in Figure 2.14. It was extract the imaging performance of the tracker by comparing the beam profile measured by the film with the one acquired with OFFSET.

2.5.2 OFFSET3

The detector has also been tested with a 62 MeV proton beam in the CATANA facility at the LNS in Catania (Italy). A long run of about 60 minutes with a beam rate of 3 MHz was performed, in which an image of the beam spot was recorded with the *OFFSET3* detector in real-time every minute, integrating the occurrences of reconstructed tracks over the time interval. In order to perform a precise calibration of the detector, a GAF-Chromic EBT3 film was placed in front of each sensitive plane crossed by the proton beam.

The calibrated GAF-Chromic EBT3 film was digitized with a scanner and the final dose distribution was used to calibrate the region of the *OFFSET3* sensitive area intercepted by the beam. For the calibration of the images acquired by the detector, the same two assumptions for the *OFFSET* detector have been done: a linear response of the scintillating fiber with respect to the received dose in the selected dose range and the same efficiency of each detector pixel. The calibration was performed summing all the images acquired with OFFSET3, pixel by pixel. It was assumed that any non-uniformity in the pixel response in the sensitive area is time invariant. In this way a calibration matrix that provides relative correction factors for each pixel of the detector, is obtained. As already mentioned in the previous section, the calibration matrix is used to correct non-uniformities in the detector response due to in-homogeneities in the optical coupling between the fibers and the PSPM and non-uniformity of the PSPM gain. The resulting images are shown in Figure 2.15.

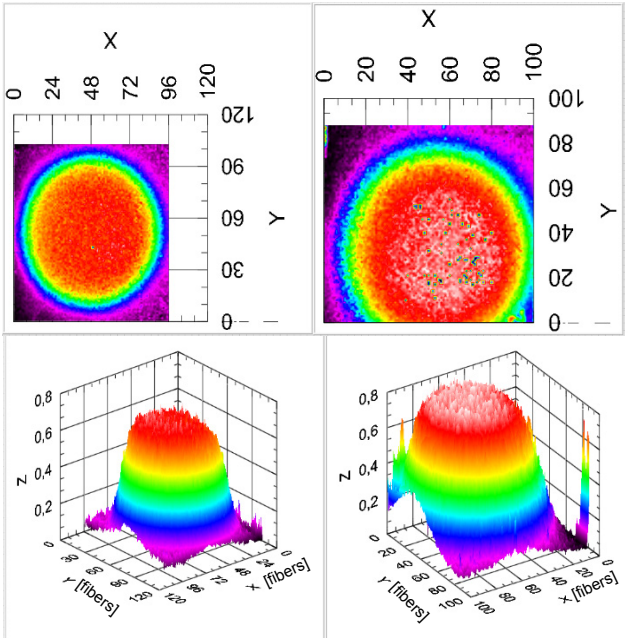

Figure 2.15 - Images obtained with a 62 MeV proton beam for the front (left) and rear (right) planes of the *OFFSET3* tracker, after the calibration performed with a GAF-Chromic film. Axes report the fiber number (one fiber has a diameter of 500 µm).

By comparing the beam profile measured with the GAF-Chromic film with the one acquired with *OFFSET3*, we verified that the expected imaging performances (500 µm/$\sqrt{12}$ spatial resolution, 5 MHz maximum acquisition rate, etc.) are actually reached by the tracker. The trajectories of each crossing particle have also been evaluated and they are shown in Figure 2.16.

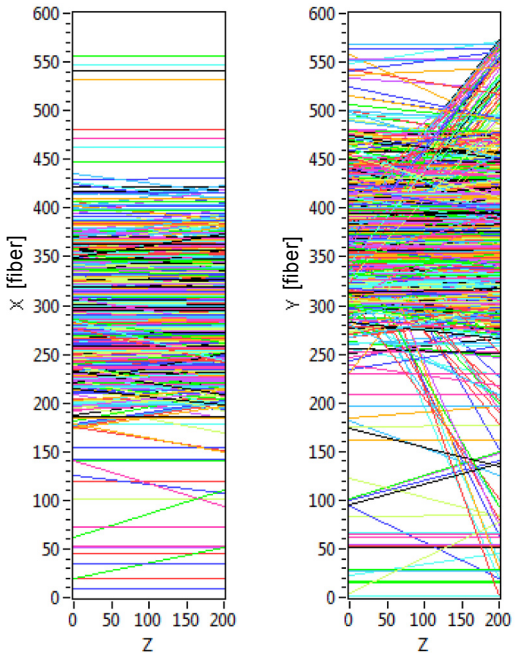

Figure 2.16 - Particle tracks obtained with the 62 MeV LNS proton beam for the two planes of the *OFFSET3* tracker, in the XZ and YZ planes. The Z direction is along the beam axis. Axes are in fiber number (one fiber has a diameter of 500 µm).

Other tests have been carried out at CNAO in Pavia (Italy) by 226 MeV protons and with 400 MeV/A carbon ions. While the CATANA beam is continuous, the CNAO beam is generated by two Electron Cyclotron Resonance (ECR) sources, able to produce both particle species, and transferred to a Radio Frequency Quadrupole (RFQ) LINAC through a Low Energy Beam Transfer line (LEBT) at 8 keV/A The ions are then accelerated up to 7 MeV/A before being injected in the synchrotron ring [18]. Placing the *OFFSET3* tracker in front of the beam, it was irradiated in different point of the sensitive area. The test results are shown in Figures 2.17 - 2.18.

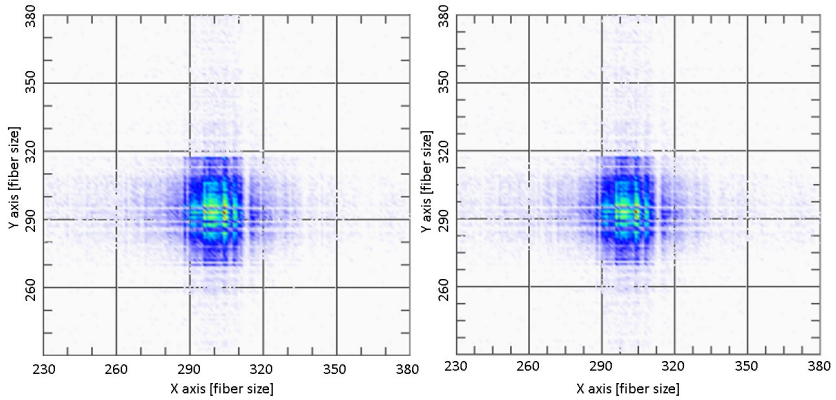

Figure 2.17 - Front (left) and rear (right) images obtained with a 226 MeV proton beam at the CNAO facility.

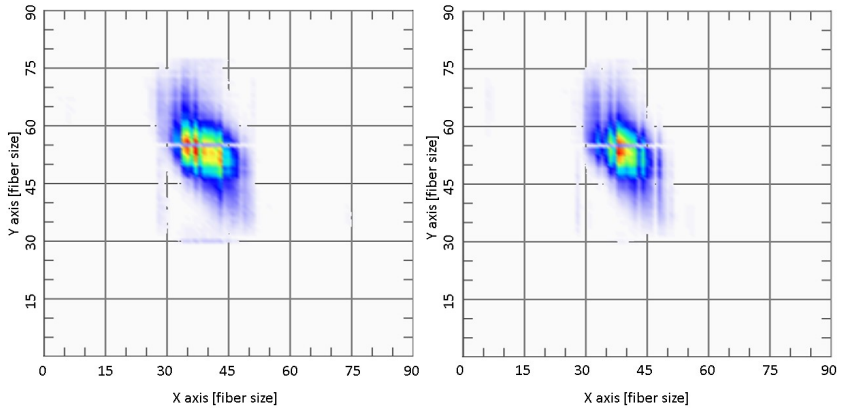

Figure 2.18 - Front (left) and rear (right) images obtained with a 400 MeV carbon beam at CNAO facility.

CHAPTER 3
THE MUON PORTAL PROJECT: GENERAL FEATURES

3.1 Motivation for the project

The traffic of containers, used in all ports around the world for the safe storage and transport of materials by cargo ships, is constantly rising; it is estimated in 200 millions containers per year. However, the content verification is reserved just to about 1% of them because of the long time required for the inspection, the complexity of positioning during a scanning phase and the related costs.

Generally speaking, the most common scanning technique is the X-ray radiography. This technique uses x-rays or other penetrating radiation such as gamma rays to image the insides of objects. It was pioneered in the 1930s and has become a cornerstone of modern diagnostic medicine and a non-destructive industrial material analysis. Modern tomography systems have come of age from 1972 and use computing tools to process the tomographic information to enhance the signal-to-noise ratio of the image, to identify critical features in enhanced visualizations, and to allow multiple slices of the object to be assembled and analyzed as a three-dimensional object. Further data processing algorithms have allowed the interpretation of scattering information as radiation passes through a material as a means of studying the composition and structure of the internals of an object. Statistical analysis applied to these methodologies can now be employed to use the multi-path scattering of radiation to produce tomographic images that provide sufficient information about the energy and direction of the radiation as it enters and leaves an object.

Because x-ray radiography requires an external source, it introduces radioactivity in the environment and is ineffective in crossing very dense objects, due to the absorption of the radiation.

The application of alternative techniques, such as directional gamma imaging and neutron radiography, is complex and expensive, and the performances can be seriously degraded in presence of shielding materials.

The increasing demand for security, however, requires scanning of all transiting containers around the world.

The Muon Portal Project [30] (2011 - 2015) proposes an alternative technique to the previous one, elaborated over the last years, based on tomography with cosmic muons.

The aim of the project is the building of a complete tomograph prototype for the identification and localization of materials hidden inside cargo containers, principally elements with high atomic number Z. Further applications could be related with its use in airports, landfills or for the characterization of air showers (primary vertex, energy,

etc...), by combining data with information from other scintillation detectors in coincidence

Worldwide, several projects have been proposed with the aim of building prototype detectors for muon tomography [31-34].

With respect to the inspection techniques exploiting x-rays, gamma rays or other particle sources (neutron, ions), muon tomography has some advantages.

Firstly, the scan is non invasive (the container remains close); in addition the use of cosmic rays does not require radiation sources dangerous for the environment and the content is not damaged because muons are Minimum Ionizing Particles (MIP). Secondly, the acquisition time is reduced to a few minutes, in contrast with the time needed by x-ray radiography (about 60 s per slice, using the Computed Tomography CT method [35]).

Lastly, the irradiation is uniform over all the surface of detector planes.

The detection technique is based on the determination of the scattering angle of each cosmic muon crossing the tracker, induced by the presence of heavy materials. Indeed, the scattering angle is particularly sensitive to the atomic number Z of the crossed material. Hence, it is necessary to reconstruct the ingoing and outgoing tracks: a system for muon tomography requires two tracking detectors, above and below the volume to be inspected.

3.2 Spectrum of secondary cosmic rays radiation

Cosmic rays are high-energy particles travelling throughout the Milky Way Galaxy, including the Solar System. Some of these particles come from the Sun, but most arrive from sources outside the Solar System and are known as *Galactic Cosmic Rays* (GCRs). Cosmic-ray particles that arrive at the top of the Earth's atmosphere are named primaries; their collisions with atmospheric nuclei give rise to secondary particles. At first cosmic rays were discovered by Victor Hess in 1912. Hess observed ion production in an electrometer carried on a manned balloon. He found that ion production doubled as the balloon rose from 1000 to 4000 meters above the sea level, indicating the presence of some kind of ionizing radiation penetrating the atmosphere.

As regards the composition of the primaries, about 85 % of the GCRs are protons, while approximately 12 % are alpha particles (helium nuclei). The remaining particles are mainly electrons and nuclei of heavier atoms. The intensity of incident primaries at the top of the atmosphere is given approximately by eq. (3.1).

$$I_N(E) \approx 1.8E^{-2.7}\,\frac{nucleons}{cm^2\ sr\ s\ GeV} \quad (3.1)$$

in which E is the energy per nucleon [36].

This expression is valid for energies above a few GeV up to about 100 TeV. Some primaries have much higher energy; ongoing research collaborations seek to determine the energy spectrum for these “ultra high energy” cosmic rays.

In the case of charged particles, being the trajectories strongly influenced by the Earth's magnetic field and the interplanetary magnetic field, most of those detected near the Earth have residual kinetic energies of about 1 GeV. This energy corresponds to a speed greater than about 87 % the speed of light. The number of detected particles drops rapidly with increasing energy, but individual particles with energies as high as 10^{20} eV have been detected.

After deflection due to magnetic fields, primary GCRs follow convoluted paths and arrive at the top of the Earth's atmosphere nearly uniformly from all directions. Consequently, identification of cosmic-ray sources cannot be based on their directions of arrival, but rather must be inferred from their abundances. It is possible by comparing cosmic-ray abundances with those deduced for stars and interstellar regions by spectroscopy. The relative abundances of different elements among cosmic-ray nuclei have been deeply studied for particles with energies from about 100 MeV to several tens of GeV. At the same time, isotopic abundances have been measured for the more abundant elements. From such studies, it has been possible to reconstruct much of the history of cosmic-ray particles journey through the Milky Way Galaxy. The light elements such as lithium, beryllium and boron are rare throughout the universe but are surprisingly abundant among the primary GCRs. It is accepted that these light nuclei are produced when heavier primaries (e.g. carbon and oxygen) are fragmented during collisions with the thin interstellar gas composed mostly of hydrogen. The GCRs would travel for about 10 million years to produce enough interstellar collisions to yield the observed number of light nuclei. The time scale for this travel is based in part on the observation of such radioactive fragments as beryllium-10. This radionuclide has a half-life of 1.6 million years, and the number of such particles that can be survived and then detected on Earth depends on their total travel time.

Making all the corrections for interstellar fragmentation, it’s possible to claim that the composition of the inferred source is similar in some ways to general Solar-System matter; however, hydrogen and helium are less abundant and additional differences exist among certain isotopes. The conclusion is that the cosmic rays represent a mixture of interstellar material enriched with matter from evolved stars, such as supernovas stars.

From the early 1930s to the 1950s, cosmic rays played a critical role in the scientific study of the atomic nucleus and its components, because they were the only source of high-energy particles. Short-lived subatomic particles were discovered through cosmic-ray collisions. In fact, the research field of particle physics was established as a result of such discoveries, beginning with those of the positron and the muon [37]. Even with the advent of powerful particle accelerators in the 1950s, researchers in the field have continued to study cosmic rays, albeit on a more limited scale, because they contain particles with energies far beyond those attainable under laboratory conditions.

It is possible to detect cosmic rays by direct observations by high-altitude balloons (typically reaching altitudes of 37 km). Rockets can reach greater heights but with smaller payloads and for only a few minutes. Cosmic-ray observations also have been made from Earth-orbiting satellites and from long-range probes. In these cases the interval of interest in the spectrum is below the so called “knee”, which is around 3-

$4x10^{15}$ eV. In the knee, the flux falls steepens than before it, although not by very much [38]. Pioneering studies were conducted on top mountains where only secondary particles were detectable.

Most energetic showers of particles produce subsequently an air shower covering a large volume in the atmosphere, the *Extensive Air Showers* (EAS). Hence, they are detectable by means of large-area telescope array on the Earth surface, such as the Pierre Auger Observatory in Argentina [39] or the *High Resolution Fly's Eye* (HiRes) detector (realized between 1994-2000) that was an ultra-high-energy cosmic ray observatory operating in the western Utah [40].

Nowadays, cosmic ray research has been an active field; there are many ongoing efforts to measure the composition, flux and *energy spectrum* of cosmic rays.

The spectrum (flux vs energy) reported in Figure 3.1 is realized thanks to results obtained from different experiments. The *Akeno Giant Air Shower Array* (AGASA) detector in Japan [41] like the HiRes in Utah estimated the energy of high energy primaries by studying air showers generated by cosmic ray interactions within the atmosphere. Both claimed to observe cosmic rays with energies above 5×10^{19} eV, much higher than any energy attainable in an existing particle accelerator.

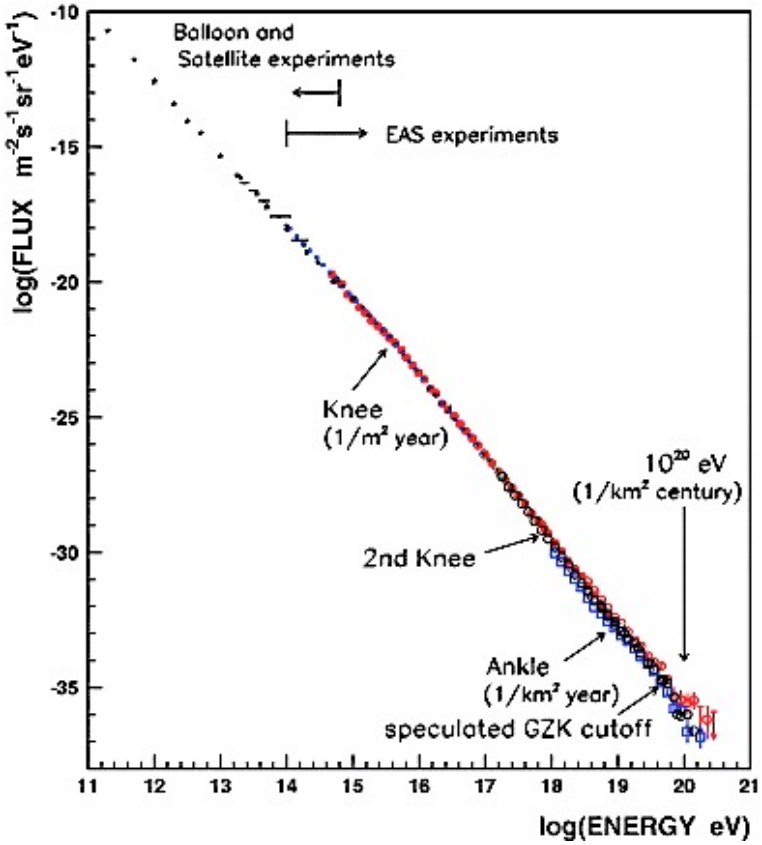

Figure 3.1 - Energy spectrum of primary cosmic rays. AGASA results covering the widest energy range ($10^{15}\div10^{20}$ eV) are shown by red closed and open circles. Direct observations with balloon and satellite-borne detectors are plotted as dots below the knee, around 10^{15} eV. The Tibet experiment (an air shower observation array in Yangbajing, Tibet) results [44], which cover the energy region just below and above the knee, are plotted as blue circles. In the highest energy region, new results from HiRes and Auger experiments are shown as open black circles and open blue squares, respectively. The overall spectrum is expressed by a power law from 10^{11} to 10^{20} eV with only small changes of slope around $10^{15.5}$ eV (the knee), $10^{17.8}$ eV (the second knee) and 10^{19} eV (the ankle) [45].

The spectrum reported in Figure 3.1 shows three different zones in which there is a sudden change in the flux slope: the knee, the second knee and the ankle. They are related to the composition, the source and the mechanism of acceleration of cosmic rays [42-43].

Energetic particles emerge from solar flares, where they have been accelerated by strong magnetic fields. Most of these particles are mainly protons, with a minor number of helium and heavier nuclei. Observations of the helium-oxygen ratio among energetic solar particles have contributed significantly to solar studies, because the Sun's helium abundance is difficult to estimate by means of conventional spectroscopy. The energy spectrum of solar particles, as compared with that of galactic cosmic rays, generally decreases more rapidly with increasing energy, but there is great variability in the shape of the spectrum from one solar-flare event to another, and the energy spectrum rarely extends above about 10 GeV.

With a lifetime of 10 million years, GCRs must be replenished at an average power level of about 10^{41} ergs per second. Supernova explosions can supply this much power as they occur about every 50 years in the galaxy. Details of the processes involved in cosmic-ray production and acceleration remain unclear, but it appears that particle acceleration could be generated from expanding shock waves from supernovas explosion.

A small anisotropy has been detected among the highest energy particles, i.e. those with energies above about 10^{18} eV. The galactic magnetic field is not strong enough to confine such energetic primary particles within the galaxy, and the main theory supposes that they are the only significant extragalactic component among cosmic rays [46]. These extremely high-energy particles are so rare that they can be detected only through the EAS that they produce in the atmosphere. An extensive air shower may consist of billions of secondary particles (mostly electrons and muons) that arrive at ground level over areas of many square kilometers.

The production of secondary muons from cosmic ray interactions is of particular interest for our research. *Muons* (μ^+/μ^-) are created in a cosmic ray shower from the decay of hadronic secondary particles; the most prevalent decay products of charged pions and kaons (composite particles, classified as mesons, consisting of a quark-antiquark pair) as shown in eq. (3.2) and (3.3).

$$\pi^+/K^+ \rightarrow \mu^+ \upsilon_\mu \quad (3.2)$$
$$\pi^-/K^- \rightarrow \mu^- \bar{\upsilon}_\mu \quad (3.3)$$

Pions (π) and *kaons* (K) are produced as nucleons interact with nitrogen and oxygen nuclei in the atmosphere. These pions have half-lives of about two hundred-millionths of a second and decay through muons to produce electrons and neutrinos. The electrons travel along spiral paths in the galactic magnetic field and finally generate synchrotron radiation, which is detectable by radio telescopes. There is a general agreement between the radio observations and calculated intensities. Synchrotron radiation has been detected from supernova remnants such as the Crab Nebula, confirming their identification as potential cosmic-ray sources [37]. Interstellar cosmic-

ray collisions also yield neutral pions, which decay quickly to produce high-energy gamma rays. Gamma-ray surveys (conducted by Earth-orbiting satellites) indicate that cosmic rays are strongly concentrated in the disk of the Milky Way Galaxy with a much smaller percentage in the surrounding halo. The measured intensity of the gamma rays is in general agreement with calculated values.

Figure 3.2 shows a schematic of a typical cosmic-ray shower, with charged meson production feeding the creation of muons.

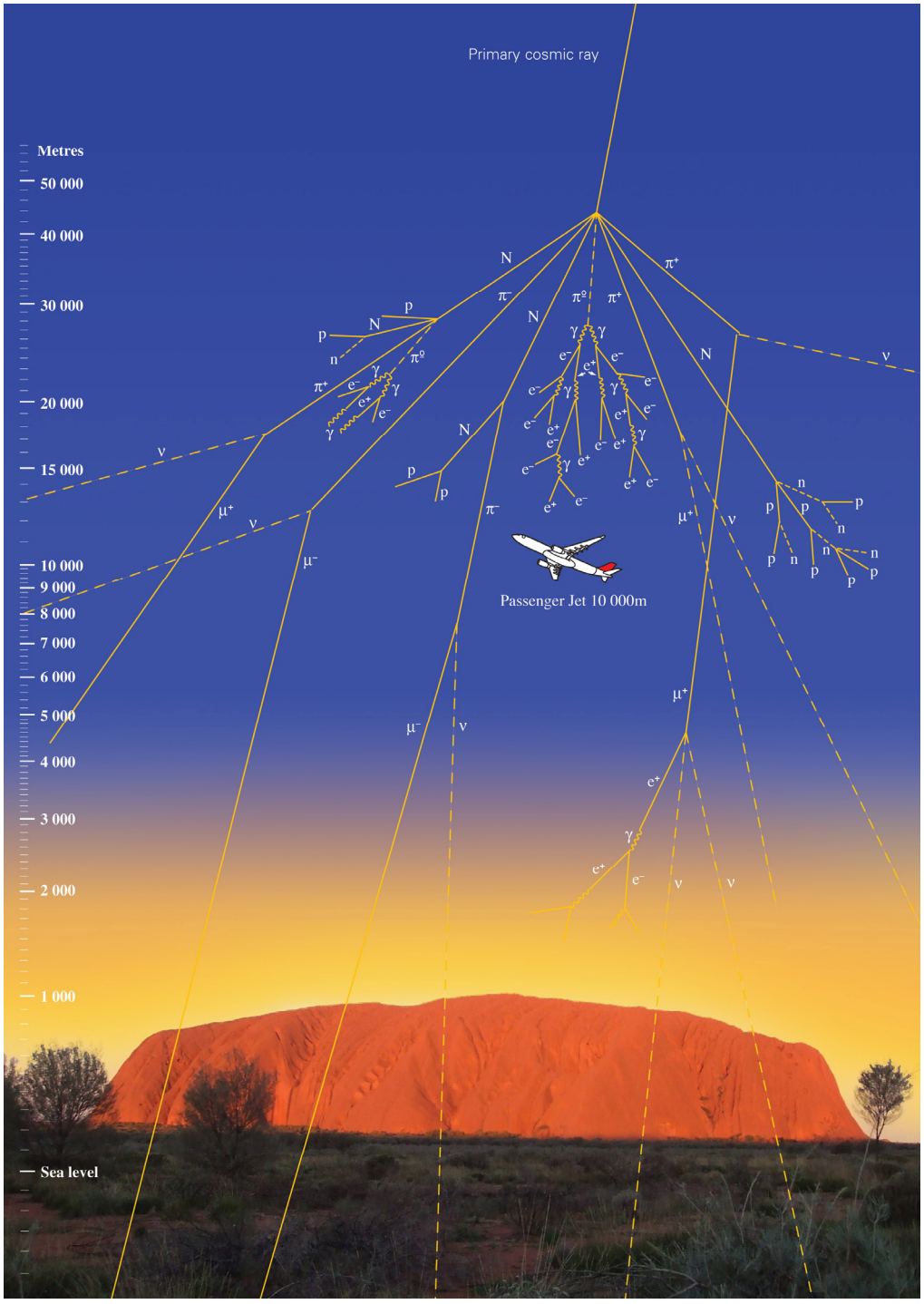

Figure 3.2 - Cosmic ray shower. The primary particle originating the shower is represented on the top and the secondary particles are displayed below [47].

Charged pions with energies greater than about 100 GeV can interact with nitrogen and oxygen in the atmosphere, producing additional cascades of secondary particles before decaying. However, lower energy charged pions would most likely undergo to a weak force and they decay before they can interact with the atmosphere. This is due to the fact that charged pions have a mean proper lifetime of 26 ns, which implies a mean free path before decay of about 55 meters for a 1 GeV charged pion. The pion travels through a very small fraction of the atmosphere; thus, interactions are unlikely.

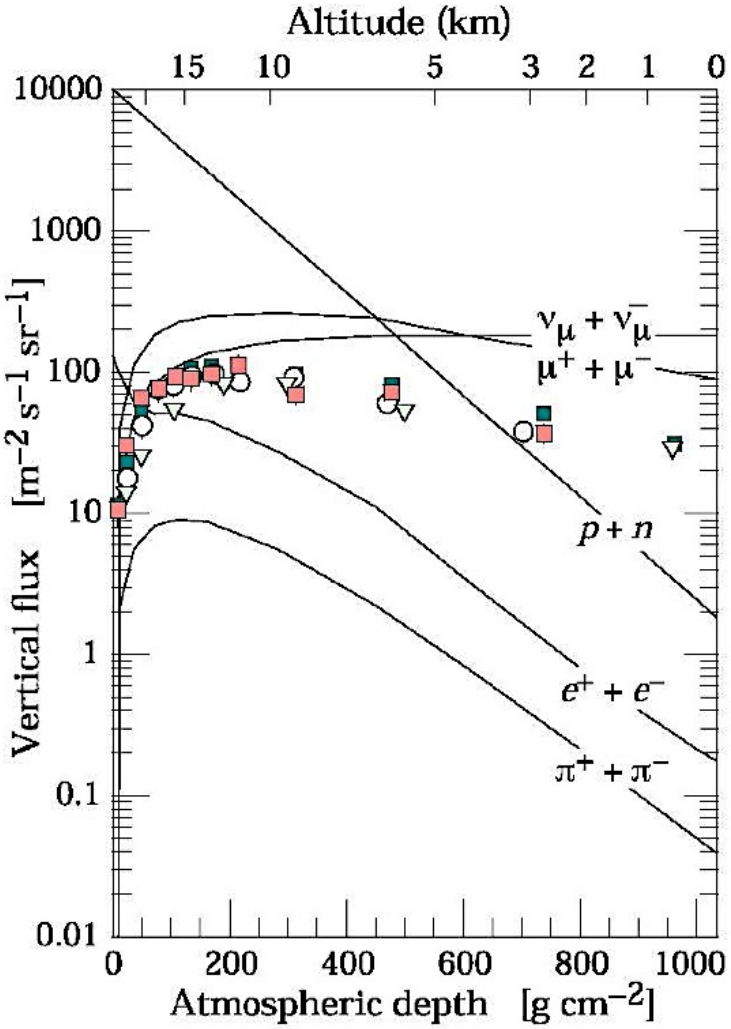

Figure 3.3 - Vertical fluxes of cosmic rays in the atmosphere with energy greater than 1 GeV. The points show measurements of negative muons with energy greater than 1 GeV [36].

Figure 3.3 shows the flux of various components of cosmic ray showers as a function of atmospheric depth. Lower energy charged pions tend to decay to muons/neutrinos around 10 to 15 km above the earth. Muons, having a mean proper lifetime of 2200 ns, tend to penetrate deeply into the atmosphere; those with energies above 5 GeV can reach far underground before decaying. The implications of data shown in Figure 3.3 are clear: muons will be the most readily measurable products of cosmic rays near the surface of the earth.

Continuously, Muons strike the Earth surface, measuring an average flux at sea level of 1 particle per cm^2 per minute. The overall angular distribution of muons at sea level is proportional to $\cos^2\theta$, where θ is the zenith angle. This implies that more total muons are detected per unit surface area at low zenith angles.

Figure 3.4 shows the energy spectrum of muons measured at two different zenith angles by a horizontal detector at sea level per unit surface area. At large zenith angles, low energy muons decay before reaching the ground and high energy pions decay before they can interact with the atmosphere. The result is a higher average muon energy at large zenith angles.

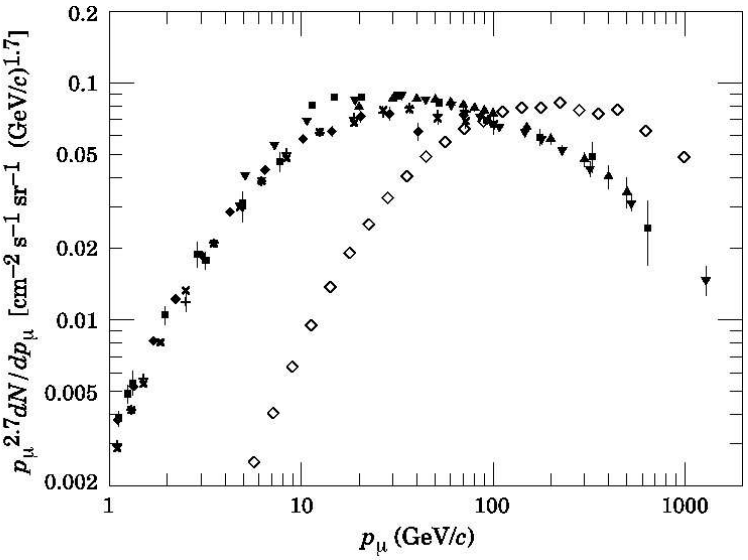

Figure 3.4 - Spectrum of muons measured from sea level. The dark points are at 0° zenith, while the hollow points are at 75° zenith [48].

3.3 Principles of Muon Tomography

Muon Tomography was developed by L.W. Alvarez et al. in the 1960s in order to study the inside of the Chephren's Second Pyramid in Egypt [49].

Indeed, to perform radiography of the pyramid, Alvarez exploited the natural flux of cosmic ray muons as primary source. The final goal was to find evidence for undiscovered tunnels or hidden chambers inside the pyramid. By setting up scintillating particle detectors into a cavity underneath the base of the pyramid (Belzoni chamber), he was able to measure muon flux as a function of zenith angle. By comparing his measurements of muon flux under the pyramid against the natural background of muons, Alvarez was able to distinguish at meter-scale the limestone caps on the outside of the pyramid. He did not find evidence for hidden chambers or tunnels, but the experiment showed the validity of muon tomography as a way to probe the bulk structure of matter.

The scanning method is based on the same principle of a common radiography: regions of low density material will allow more muons to pass through and reach the

detector than regions of high density material. These differences can be assembled using methods of computer-assisted tomography into a 3D image of the overburden. An image of a location of interest is constructed as follows:

- Each image is obtained measuring the muon flux for a chosen angle and location over the target volume;
- By varying the flux for different angles and directions it is possible to reproduce a 3D image of the target volume using standard techniques of computer-assisted tomography.

In order to optimize the resolution of the images, it is important to take into account the possible scattering of muons inside the target, due to the ionization of the solid material and consequent delivery of energy inside it.

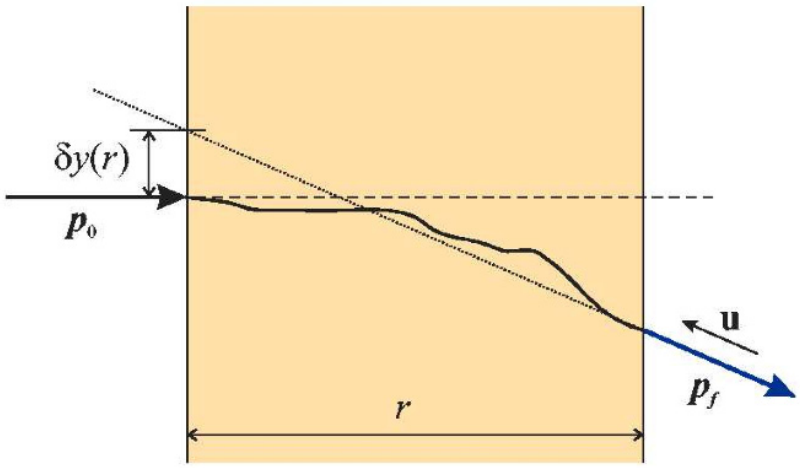

Figure 3.5 - Scheme of a muon undergoing multiple-Coulomb scattering in a dense medium. The final detected muon momentum is p_f, while the muon momentum before entering into the medium is p_0 [50].

Figure 3.5 illustrates the uncertainty in a muon track due to multiple-Coulomb scattering. The probability of scattering decreases as the muon energy increases. Therefore, the solution for minimizing tracking errors associated with scattering is to consider only muons with energy big enough to have a low probability of scattering through the crossed material. Muons lose approximately 2.2 MeV for every g/cm^2 of matter they travel through [36]. Using this basic energy loss formula [51], it can be shown that for a material with density $\rho = 2.3$ g/cm^3, the cutoff in muon energy should be around 2.5 GeV. This ensures that the muon spectrum is "hardened" at the detector. Alvarez accomplished this by surrounding his detector with iron blocks. This way, lower energy muons were absorbed into the iron and not considered in the flux measurements.

Today, the muon tomography has found new interesting application in addition to pyramids imaging, such as volcano tomography, nuclear reactors and fossil fuel

monitoring and also in order to localize high-Z dangerous materials hidden inside cargo containers.

Several Monte Carlo simulations have been performed in order to well modeling the variation of muon energy and flux to probe the internal structure of very large objects such as large industrial structures [52].

3.4 Localization of high Z hidden materials

3.4.1 Motivations

One of the most critical challenges remaining to the international security establishment is related with the effective detection of nuclear materials, also properly shielded. In 2008, the following note was written in a report by the US General Accounting Office: "*we found that a cargo container containing a radioactive source was not detected as it passed through radiation detection equipment that the Departments of Energy had installed at a foreign seaport because the radiation emitted from the container was shielded by a large amount of scrap metal. Additionally, detecting actual cases of illicit trafficking in weapons-usable nuclear material is complicated: one of the materials of greatest concern in terms of proliferation—highly enriched uranium—is among the most difficult materials to detect because of its relatively low level of radioactivity*". In this context there is a clear necessity for a specific solution to overcome this highly dangerous threat.

The requirements for a screening system are:

- Distinguish broad range of contraband cargo containers;
- Provide density, shape and composition images;
- Scan consolidated cargo without unpacking;
- Rapid scans (a few minutes/container) and short turn-round time;
- Minimum number of false indications;
- Comply with strict radiation safety requirements for both operating staff and cargo irradiation;
- Readily integrated with existing port/airport systems;
- Reasonable capital and operating costs;

In this context there is a clear strong necessity for a specific solution to discover this highly dangerous threat. Cargo scanning or non-intrusive inspection refers to non-destructive methods of inspecting and identifying goods in transportation systems. It is possible to distinguish between radiography technique and passive radiation detectors in order to scan the container.

The work described in this thesis is focused on Muon Tomography that is the technique used for the Muon Portal Project.

3.4.2 Muon Tomography

Worldwide, many researchers involved in different experiments have begun investigations onto the use of passive muon tomography systems for cosmic rays as a way of addressing the shortcomings of other technologies to detect the smuggling of Special Nuclear Materials (SNMs) in cargo. The detection technique is based on the tracking of individual muons as they enter and exit a structure subject of study. Most current efforts have been geared toward demonstrating the potential for muon tomography [53]. In the UK, the Sellafield facility, placed in the North-West of England at the current site of CalderHall, is the main nuclear waste reprocessing facility. In this contest, muon tomography is applied in order to recognize *Intermediate Level Waste* (ILW) and *High-Level Waste* (HLW) products stored within nuclear waste containers. At the University of Glasgow, a prototype muon tomography system, consisting of four scintillating-fibre tracker modules, has been constructed to assess the potential of this technology in the identification and characterization of high-Z materials stored within legacy nuclear waste containers (Figure 3.6). In each module there are two orthogonal planes of 128 Saint Gobains plastic scintillating fibers, with 2 mm pitch and 97% active cross-sectional area for each.

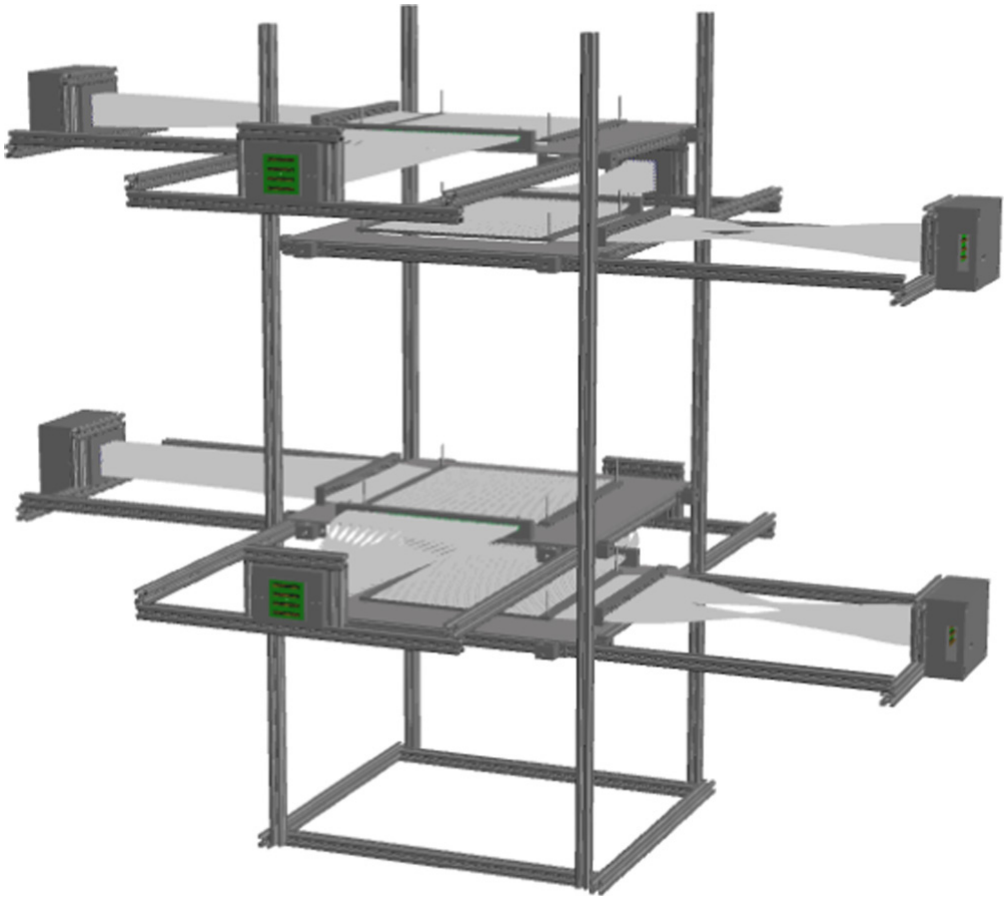

Figure 3.6 - CAD model of the prototype Glasgow muon tomography detector. The four tracking modules consisting of two orthogonal layers of scintillating fibres each connected to a PhotoMultiplier (PM) are shown. The PMs are fed through customized built *PolyOxyMethylene* (POM) distribution blocks that provide further support and maintain a constant tension across the fiber set. The four modules are assembled in an aluminium profile support frame [54].

Muon detection and analysis is continuously developed in high-energy physics laboratories in response to find new particles or decay mechanisms, and also became important in the characterization of cosmic rays. Through the 1970s to the mid-80s, the importance of muon analysis grew: from one of the oldest sentences: 'Some outside chambers to also detect muons, the interest for muons is changed, as is clear from the following sentence: 'The need for accurate and complete muon detection by charge and momentum [55]. Work has continued in this field until now and these advances, funded as part of pure research projects, are at a point of maturity where field deployable systems are within reach through modest research and development programs. *Passive Muon Tomography* (P-M-T) systems are a relative newcomer into the arsenal of nuclear material detection in security applications; however, P-M-T technology specifically addresses the limitations of other existing technologies by being able to use the pervasive cosmic ray background on Earth to "look through" vehicles and containers to detect the presence high-Z nuclear materials or shielding that might mask the radioactive signatures of other materials of concern. Although muons are unstable charged particles, those generated from cosmic ray showers have sufficient lifetime and momentum to survive the trip to the surface of the Earth, even if they are slowed somewhat interacting with the atmosphere. Furthermore, since they are not subject to the strong interaction force, they do not lose momentum through nuclear interactions but rather much more slowly through the Coulomb force due to their charge. Where gamma rays imaging systems can penetrate roughly 1-2 cm of lead shielding and 15 cm of steel, muons that reach the Earth's surface from cosmic ray interactions in the upper atmosphere can penetrate roughly 2 m of lead and more steel than could be used inside a shipping container or a truck.

The generic architecture of the detector has to enclose the target object on at least the top and bottom and require multiple layers to determine the trajectories of each crossing muon incoming and outgoing the target. Further layers of detectors are required to possibly determine the momenta of the muons useful in the data analysis. Because of the required size (several meters on a side), convenient construction and careful calibration techniques must be employed. The main limitation is that, unlike a x-ray tomography system which will rotate around the object of interest, the passive muon tomography system relies on cosmic ray muons which naturally penetrate the object from multiple angles and allow a tomographic image by employing statistical analysis of the multiple-scattering of the muons off the nuclei that compose the object. Besides the general complexity of a muon tomographic system, one final limitation needs to be addressed: the density of the muon flux at the Earth's surface. Since there is roughly only one muon event per square centimeter per minute, the resolution requirements for detection have a profound impact on the exposure time required for a full "scan" (note that the size of the object does not affect the scan time as the number of muon events scales with the size of the detector surface area). Many of the challenges of using this new technology are compensated by the relative sensitivity of muon tomography to the detection of high-Z materials such as uranium, plutonium, and lead because those nuclei have relatively large effect on muon paths. An example of a graphic interface to control a muon tomography system is reported in Figure 3.7.

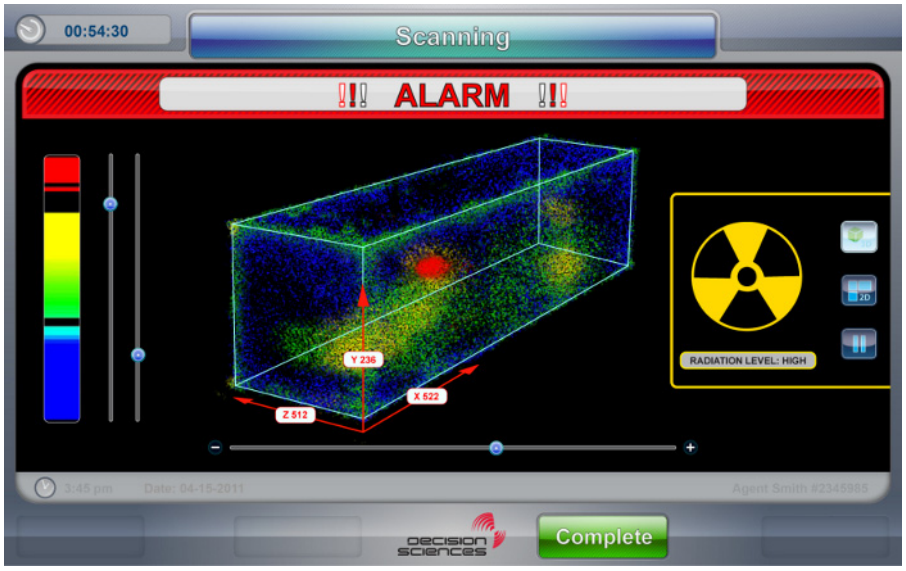

Figure 3.7 - Interface of a scanning container system from Los Alamos National Laboratory [56].

3.4.3 Alternative techniques

A. X-rays or γ-ray Radiography

High energy X-ray or γ-ray radiography and tomography are the most commonly used screening techniques, providing high resolution images of shape and density. Also from the point of view of international security, these techniques could provide an excellent tool to non-intrusively verify the contents of cargo traffic moving across borders such as ports, airports and across transit hubs [57].

X-ray radiography employs a high-energy Bremsstrahlung radiation source with energy in the 5-10 MeV range created by a *linear particle accelerator* (LINAC). Such X-ray systems can penetrate up to 30–40 cm of steel in vehicles moving with velocities up to 13 km/h. They provide higher penetration but also cost more to buy and operate. They are more suitable for the detection of special nuclear materials than gamma-ray systems. They also deliver about 1000 times higher dose of radiation to potential hidden passengers.

Many commercial systems (fixed, mobile, LINAC, radioisotope sources) are available in the market.

One of the limitations related to these systems is the complexity in order to produce the tomographic imaging. Generally, there is the necessity to move the radiation source and imaging units around the scanning target (although advances have allowed to develop systems with fewer or no needed moving parts, but the issue remain the same). The amount of time and the amount of radiation exposure required to produce the tomography are relatively significant compared to 2D imaging techniques,

and for people in the environment could cause health concerns. Moreover, even gamma radiation with energy in the low MeV range provides only minimal improvements in the detection ability of nuclear materials or for shielding materials needed to smuggle radioactive materials with respect the use of x-ray. It is difficult to distinguish organic materials and experienced operators are required for complex, cluttered images.

Figure 3.8 shows a schematic drawing of an X-ray inspection system for cargos and containers widely use in air, rail and marine transportation.

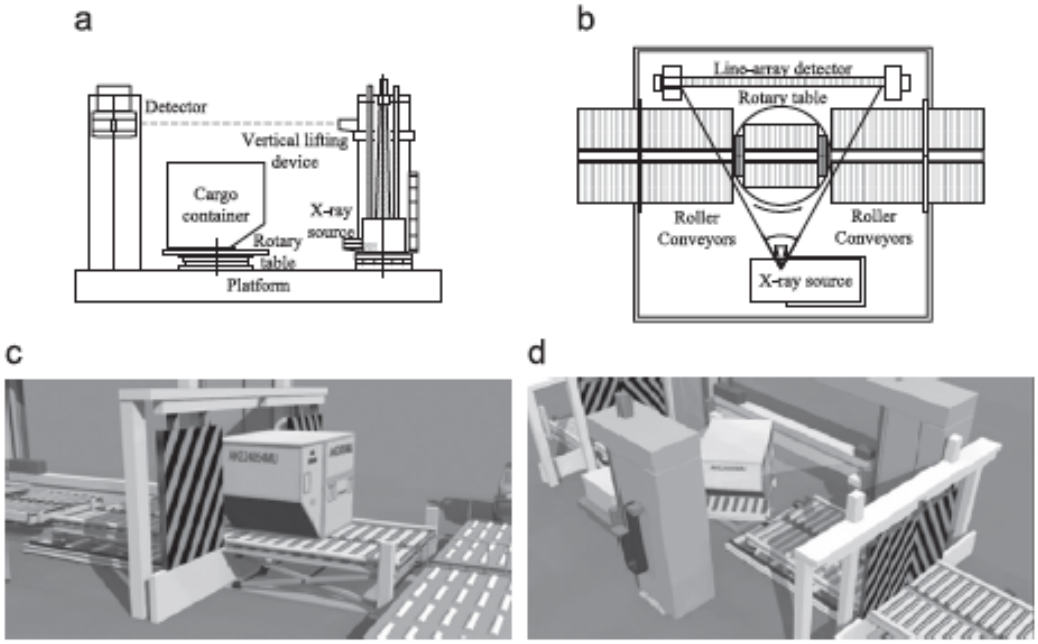

Figure 3.8 - A schematic drawing of an inspection system. The major parts include: an X-ray source, a line-array detector, data acquisition and processing, scanning control and radiation protection subsystems. (a) Side view. (b) Top view. (c) and (d) Demonstrations of the transmission and scanning process of an air container, respectively [58].

A variety of X-ray systems have been developed including cargo/vehicle inspection systems and industrial CT for practical applications in a comprehensive range of fields.

Most X-ray imaging systems contain two types of imaging methods: *digital radiography* (DR) and CT imaging. DR imaging is most widely used because of its simplicity and quickness. It emphasizes high throughput, but images acquired a real ways with objects overlapped so that it is difficult or impossible to distinguish these objects. On the other hand, tomographic imaging provides across-section image of the scanned object so that each object is clearly separated from each other. However, CT imaging usually requires a considerable number of projection data to reconstruct an accurate cross-section image.

Data acquisition is time-consuming. Few-view imaging can be regarded as a special type of CT with sparse angular projection data, a mode in between DR and CT. The advantage of few-view imaging lies in quickly scanning and a lower radiation dose than common CT. *Cargo Inspection Systems* (CISs) take the advantage of fast scanning

to efficiently locating suspicious cargo. Radiographic images obtained with the listed scanning techniques are reported in Figure 3.9.

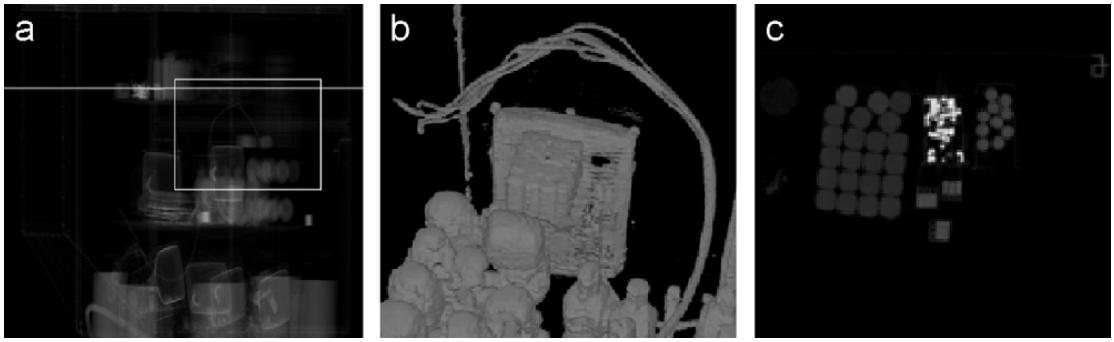

Figure 3.9 - A cooperative work manner of three modalities: DR, few-view and CT imaging. (a) DR image of an air container. (b) 3D image from 18-view few-view imaging with a view window of the white rectangle in (a). (c) CT image taken in the height as marked by the horizontal white line in (a) [58].

In literature, there are two main approaches overcoming a bad reconstruction due to data insufficiency. The first approach is the analytic reconstruction: missing data are estimated from a measured dataset so that an image is reconstructed using analytic algorithms. This method may be useful in specific situations, but it is difficult to make general conclusions on the implementation of this approach. The second approach reconstructs an image from available measurements in an iterative form. The algorithms of this approach differ in their mathematical models for reconstruction and numeric process of iterative schemes. This approach has achieved varying degrees of success for tomographic reconstruction from incomplete data. The reconstruction algorithm used in the study of Figure 3.9 is of this type. In Figure 3.10 X-ray radiography of a human phantom into a container is shown.

Figure 3.10 - X-ray scan image of a human phantom into a container [59].

Gamma-ray radiography uses radioactive particle sources of ^{60}Co or ^{137}Cs for the cargo inspection and a vertical tower of gamma detectors to reconstruct the final image that is able to produce one column of an image. The horizontal dimension of the image is produced moving either the object of interest or the scanning device. The ^{60}Co

units use gamma photons (1.17 MeV and 1.33 MeV), which can penetrate up to a depth of 15–18 cm of steel. The systems provide good quality images that can be used for identifying cargo and comparing it with the cargo manifest, in an attempt to detect anomalies. It can also identify high-density regions too thick to penetrate, which would be the most likely to hide nuclear threats.

B. Neutron Activation Techniques

Neutron activation techniques are mainly divided into two classes: Radiography and Secondary Radiation. Both of them present some advantages. It is possible to determine elemental composition in addition to density.

Successfully neutron techniques must meet the industry requirements and have significant advantages over the established and developing X-ray and gamma-ray systems.

Examples of neutron activation systems include: *Pulsed Fast Neutron Analysis* (PFNA), *Fast Neutron Analysis* (FNA) and *Thermal Neutron Analysis* (TNA). All three systems are based on neutron interactions with the inspected items examining the resultant gamma rays to determine the elements being radiated. TNA uses thermal-neutron capture to generate the gamma rays. FNA and PFNA use fast-neutron scattering to generate the gamma rays. Additionally, PFNA uses a pulsed neutron beam to generate a 3D elemental image of the inspected item.

Among the passive radiation detectors, there are the gamma radiation detectors.

Radiological materials emit gamma photons. Efficient gamma radiation detectors are the Radiation Portal Monitors (RPM). These systems are currently used in US ports (and steel mills). They consist of several large *PolyVinylToluene* (PVT) panels (usually 4) as scintillators and can be used on vehicles moving up to 16 km/h [60].

However, RPM are incapable to distinguish gammas originating from nuclear sources from gammas originating from a large variety of benign cargo types that naturally emit radioactivity, including bananas, cat litter, granite, porcelain, stoneware and so on.

Radiation originating from Earth is also a major contributor to the background radiation.

Another limitation of radiation detectors is that gamma photons can be easily suppressed by high-density shields made of lead or steel that prevent detection of nuclear sources. However, those types of shields do not stop fission neutrons produced by plutonium sources. As a result, radiation detectors usually combine gamma and neutron detectors, making shielding effective only for certain uranium sources.

Neutron radiation detectors use neutrons emitted by fissile materials such as ^{239}Pu. Radiation Portal Monitors often use ^{3}He-based detectors to search neutron signatures. However, a global supply shortage of ^{3}He has led to the search of other technologies for neutron detection [61].

C. Dual-Beam Radiography

Developments and applications of *Dual-Beam Radiography* (DBR) for cargo

inspection have been recently developed [62]. DBR techniques use various combinations of high-energy x-rays and neutrons and they are attractive techniques for screening bulk cargo for contraband such as narcotics and explosives. DBR is an important enhancement to conventional single-beam X-ray radiography systems. It provides additional information on the composition of the object being imaged. By comparing the attenuations of transmitted dual high-energy beams, it is possible to build a 2D image, colour coded to indicate material.

Only high-energy x-rays (4-10 MeV), gamma-rays (average energy of 1.25MeV) and fast neutrons (few hundred keV or larger energies) have the required penetration to screen cargo containers [62].

These recent developed systems include dual high-energy X-ray techniques as well as fast neutron and gamma-ray (or X-ray) radiography systems. High-energy X-ray systems have the advantage of a better penetration than neutron systems, depending on the material being interrogated.

However, neutron systems have the advantage of much better sensitivity to material composition compared to dual high-energy X-ray techniques. In particular, fast neutron radiography offers the potential to discriminate between various classes of organic material, unlike dual energy X-ray techniques that realistically only offer the ability to discriminate between organic and metal objects.

3.5 Other applications of Muon Tomography

3.5.1 Pyramids Imaging

The Maya Muon Group of the University of Texas at Austin performed Imaging of the Maya Pyramids, in Mexico. A sketch of the experimental set up is reported in Figure 3.11 [63].

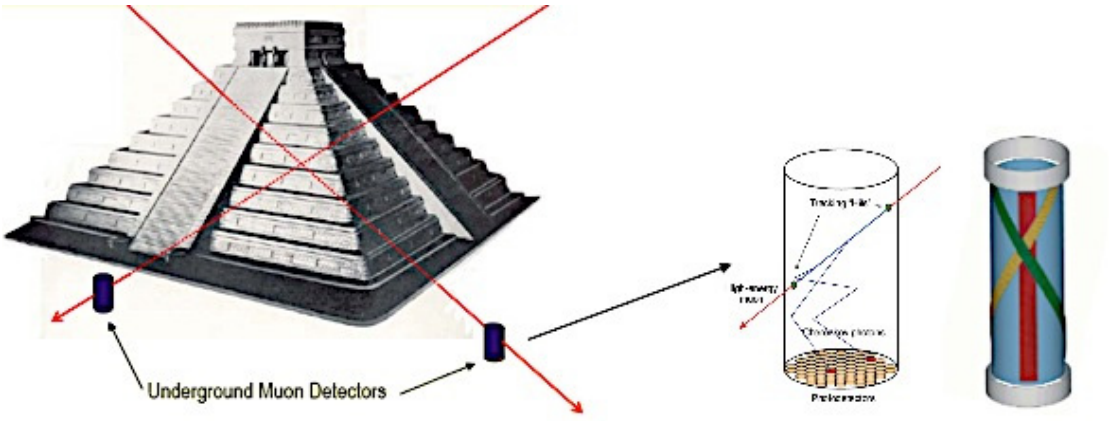

Figure 3.11- Sketch of the experimental set up for the Imaging of the Maya Pyramids.

Using improved technology and standard techniques in particle physics it is possible to detect underground muons and to measure their trajectories with sufficient accuracy to highlight at meter-scale structures as far as 50-80 meters away from the detector. To achieve muon detection rates large enough to reconstruct an image, with exposure times measured in weeks to months, the detector system must have a sensitive area of several square meters. A system of moderate complexity (of order a thousand channels of information) is needed to track the muons with sufficient pointing accuracy. Even if it is large in comparison to traditional monitoring equipment, this scale detector is modest by contemporary standards in particle physics.

3.5.2 Volcano Tomography

Another rising application field is the volcano tomography.

In general, the ability of monitoring natural events such as earthquakes, landslides, tsunamis and volcanic eruptions has great importance, both in scientific and societal fields [64]. At first, during the last decades, in Japan the interest of volcano radiography has arisen [65-69], as a consequence of the presence of large volcanic and seismic activities, like other places in the world such as Italy and Iceland in Europe or the Antilles belt in the Atlantic ocean. An example is the test measurement on Mt. Tsukuba [70]. It was made clear that nearly horizontal cosmic-ray muons can be used to explore the inner-structure of a gigantic geophysical substance, such as the top region of a volcano. The time dependent measurement as well as an extension to three-dimensional tomography would contribute to the identification of any anomaly, suggesting a powerful new prediction method of a volcanic eruption. Because of the possible proximity with populated areas, volcanoes require careful monitoring of their activity and precise modeling of their geophysical evolution.

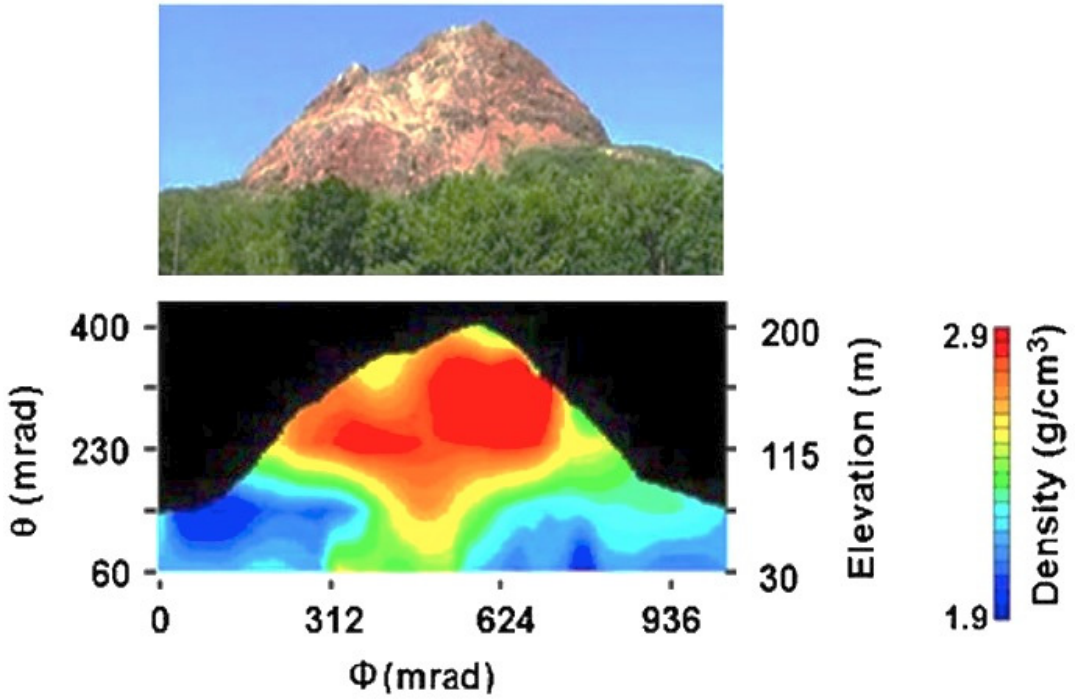

Figure 3.12 - Top: view of the Showa-Shinzan lava dome. Bottom: average density distribution projected onto the detector's plane [62].

In detail, it is necessary an accurate imaging of the volcano's inner structure and quantitative estimates of the related parameters (variations of volume, density, strain or pressure) associated with fluid transports (magma, gas or water) or physical and chemical evolution of the volcanic materials. La Soufrière of Guadeloupe, an andesitic volcano whose lava dome is about five hundred years old, is particularly relevant since it presents a diversified number of hazards including phreatic eruption, flank collapse and explosive magmatic eruption. Its dome is very heterogeneous, with massive lava volumes embedded in more or less hydrothermalized materials. Given the constant erosion of the volcano due to the tropical intensive rain activity, the evolution of such a lacunar structure may be rapid, with formation of cavities, that may be filled with pressurized and likely very acid fluids, resulting in flank destabilization. On the top, present structural models show that the dome sits on a 15° N–S inclined plane, leading to an overall very unstable structure (see Figure 3.12). This particular example shows that a precise knowledge of the dome's internal structure is a key issue for the global modeling and understanding of the volcanoes. For this reason, La Soufrière has been chosen as priority target for muon imaging [64], which constitutes one of the most promising tools to obtain direct information on the density distribution inside geological objects.

The application of muon tomography gives access to the opacity ϱ of the geological structures by comparing the muons flux Φ after crossing the target to the incident open sky flux Φ_o. Various models give analytical expressions of the muon flux from the two-body decays of pions and kaons and assuming a primary proton flux spectrum roughly following a power law $E_p^{-2.7}$ [71]. The opacity is converted to density ϱ by inverting the integral eq. (4):

$$\varrho(kg\ m^{-2}) = \int_L \varrho(\mathcal{E})d\mathcal{E} \quad (3.4)$$

where L denotes particles trajectory with local coordinate $\mathcal{E}$. The muons energy loss (and potential absorption) on their way through rock accounts for the standard bremsstrahlung, nuclear interactions, and e−e+ pair production physical processes, taken as:

$$-\frac{dE}{d\varrho}(MeV\ g^{-1}\ cm^2) = a(E)b(E)E \quad (3.5)$$

in eq. 3.5 the functions *a* and *b* depend on the crossed material properties. The flux of muons emerging from the target is the integral of Φ over the energy, ranging from $E_{min}(\varrho)$, the minimum initial energy necessary to cross a given opacity ϱ, to infinite (Figure 3.13). This flux is influenced by various environmental parameters such as the altitude, geomagnetic cut-off, solar modulation, atmospheric variations and all of them should be accounted in the simulation models. Finally the number of detected muons is the convolution of the muons flux crossing the target, the data taking duration and the telescope acceptance, which is the key experimental parameter that one may evaluate from the simulation and/or from the data themselves.

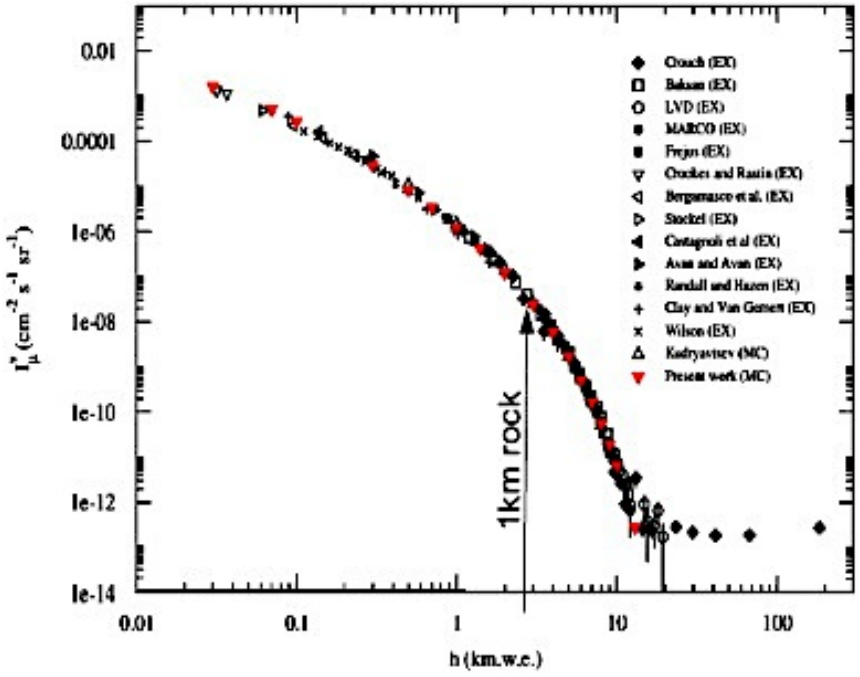

Figure 3.13 - Integrated flux computed as a function of the standard rock thickness L in metres-water-equivalent compared to experimental points.

Another project with the same goal is the Mu-Ray project was funded by the *Italian National Institute for Nuclear Physics* (INFN) and the *Italian National Institute for Geophysics and Volcanology* (INGV) in order to map the inside of volcano Vesuvius, located in Naples, Italy. The last time this volcano erupted was in 1872.

The project aims at the construction of muon telescopes and the development of new analysis tools for muon radiography. The detector consists of muon telescopes, required to be able to work in harsh environment and to have good angular and time resolutions, large active area and modularity with low power consumption. Each telescope is made of two X–Y planes of 2x2 m^2 area of plastic scintillator strips. Each strip has a triangular cross-section and is read by a fast *Wave-Length Shifting* (WLS) fiber coupled to a silicon photomultiplier. The readout electronics is based on the SPIROC chip [72].

3.5.3 Nuclear Reactors Monitoring

An additional application is related with the monitoring of nuclear reactors. With this purpose, in the summer of 2011 a reactor model was monitored by a *Muon Mini Tracker* (MMT) at Los Alamos. The MMT consists of two muon trackers made up of isolated drift tubes. In the demonstration, cosmic-ray muons passing through a physical arrangement of concrete and lead materials similar to a reactor were measured. The mockup consisted of two layers of concrete shielding blocks, and a lead assembly in between; one tracker was installed at 2.5 m height, and another tracker was installed on the ground level at the other side. Lead with a conical void similar in shape to the melted core of the Three Mile Island reactor imaged through the concrete walls. It took 3 weeks to accumulate 8×10^4 muon events. The analysis was based on finding the point of closest approach, where the track pairs were projected to the mid-plane of the target, and the scattered angle was plotted at the intersection. This test object was successfully imaged, even though it was significantly smaller than expected at Fukushima Daiichi for the proposed *Fukushima Daiichi Tracker* (FMT) [73].

3.5.4 Fossil fuel Monitoring

Fossil fuels are the predominant energy source in many world Countries. However, scientific reports showed that emission of CO_2 might cause climate changes [74] and acidification of sea water. Both phenomena are seriously affecting the ecosystem, which could possibly cause extinction of various species of animals and plants. In order to avoid it, it is still possible to reduce CO_2 emission satisfying, at the same time, the energy demand by using fossil fuel with *Carbon Capture and Sequestration/Storage* (CCS) method. CCS technologies consist in removing CO_2 either before or after combustion, then storing it by either mechanical or chemical methods. Typically, for geological storage, CO_2 could be compressed into liquid and than injected into the porous storage layer, about 1000 to 2000 meters underground below a layer of cap rock, which is an impermeable rock layer that forms a physical barrier above the storage location. In order to ensure that the CO_2 stored remains in the reservoir and to understand what happens to the CO_2 after injection, it is essential to monitor the

reservoir with suitable devices. Because the principle of muon tomography is based on changes in density, therefore it could be applied for monitoring a CCS storage site: in case of leak or CO_2 migration, density of reservoir will decrease, which could be signified by an increase of muon intensity at the bottom of the reservoir. Calculations are done in order to assure the effectiveness of using muon tomography as a carbon storage monitoring method. Results show that, at specific conditions, muon tomography could become an effective monitoring method. For example, there is a correlation between the detector dimension and the sensitivity to CO_2 loss as reported in Tab. 3.1. However, more calculations should be done in order to optimize the detector's design.

Dimensions of Detectors and their sensitivity in terms of %CO_2 loss				
	Original Design	Design 1	Design 2	Design 3
Dimension (m×m×m)	1×1×1	5×0.2×0.2	10×0.2×0.2	20×0.2×0.2
Top Surface Area (m^2)	1	1	2	4
Sensitivity	75%	84%	62%	44%

Table 3.1 - The summarized results of a set calculation on the correlation between detector dimension and its sensitivity to CO_2 loss.

3.6 The Muon Portal Project

Each year, more than 120 million vehicles are in transit to and from the United States borders. Many of them, could illegally transport nuclear weapons or material hidden inside containers. As explained in the previous Sections of this chapter, deployed x-ray or gamma-ray radiography systems present many limitations, i.e. the impossibility to be employed on occupied vehicles and the possible danger for the operators.

The *Muon Portal detector* (*PORTAL*) overcomes these limitations providing tomographic images measuring the scattering of natural cosmic radiation as it crosses each cargo container. The information provided by our scintillating detection after muon interrogation permits to identify and localize illicit material, even in the presence of screens designed to mask its existence. Muon Tomography could represent a valid solution to safe and robust border protection against the contraband of radioactive devices all over the World. The detection principle is based on the detection of the deflected muons as a result of crossing a high-Z material (both nuclear material and high-Z shielding materials) by the reconstruction of the incoming and outgoing tracks.

The muon flux at sea level is about 1 muon/(cm^2·min) in an energy and angular range useful for tomography. The trajectory of a charged particle through any material is the result of the convolution of many small contributes due to Coulomb scattering

from the charge of the atomic nuclei in the traversed medium. The angular and position deflection of the trajectory are very sensitive to the Z of the atomic nuclei.

The architecture of the *PORTAL* tracker includes 8-position sensitive planes, 6 m long and 3 m wide, large enough for the inspection of standard containers. Each plane is made of strips of plastic scintillators coupled with a very sensitive photon detector, the Silicon Photomultiplier (SiPM) widely discussed in Chapter 1. For the reconstruction of tomographic images, a tracking algorithms and suitable imaging software were specifically developed. Details on the detection architecture are reported in Cap. 4.

Muon tomography provides a method that is effective at detecting high-Z material in liter-sized volumes. A preliminary study consisting of a considerable amount of theoretical analysis, supported by GEANT simulation has been conduct. Simulation results demonstrate the possibility of reaching detection times of few minutes.

The research program for the Project includes the development of simulation procedures, the choice of detectors to be used, the characteristics of photosensors used for the detection apparatus, the readout electronics and data acquisition and control software and visualization [75].

CHAPTER 4
FROM THE OFFSET3 TO THE PORTAL: KNOW HOW TRANSMISSION

4.1 Introduction

The design and construction of the detector *OFFSET3* has been of great assistance for the construction of the *PORTAL* tomograph. Firstly, both detectors are highly segmented, with sensitive areas consisting of scintillating materials: Saint Gobain Sci-Fis in *PORTAL* and extruded plastic scintillator strips in *OFFSET3*. In the Muon Portal detector, light collection is optimized by adding two WLS fibers inside each strip, in order to collect the blue scintillation light emitted by the strip and convert it to the most appropriate wavelength for the photo-sensor. Secondly, the reduction channels strategy is applied to both described detectors, but in different ways: in the first case an optical reduction technique is used by properly grouping the fibers, while in the *PORTAL* the reduction is applied to the analogue signals. Lastly, both detectors take advantage of modular front-end and acquisition electronics, scalable and available as complete products in the selected market. In addition, it is programmable by LabVIEW software and the data acquisition is real-time (the average particle rate is lower than the acquisition rate).

Obviously, even if the ideas on their working functionality is common, properly specifications of each detector fit with the required performances. For example, SiPMs is preferred rather than PMTs as photosensors due to the amount of read-out channels for the Muon Portal. Indeed, high voltage supplies are not required because for SiPMs.

Since the Muon Portal detector is a double tracker able to reconstruct ingoing and outgoing muon tracks after the particle crosses the material to be inspected, we could consider the Muon Portal an *OFFSET3*-like double tracker.

The motivations on which the Muon Portal Project, hereafter named “Project”, is based are described in Chapter 3.

In this chapter, the descriptions of the detector architecture, the individual components characterization, experimental tests and construction phase are reported.

Details for each detector component will be analysed in the following sections. They were chosen after the evaluation of appropriated test and simulation results. In particular, scintillation detectors are widely used in physical research, i.e. high energy physics, spectroscopy, neutron detection, calorimetry, residual range measurements, PET and others [76-77]. The suitable scintillator can be selected for a desired application, as is reported in Tab. 4.1.

As already discussed in Chapter 1, several scintillating materials could be chosen for our purpose, but plastic scintillators are the best in terms of costs and variety of shapes and sizes required.

Materials	Important Properties	Major Applications
NaI(Tl)	Very high light output, good energy resolution	General scintillation counting, Health Physics, environmental monitoring, high temperature use
CsI(Tl)	Non-hygroscopic, rugged	Particle and high energy physics, general radiation detection, photo diode readout, phoswiches
CsI(Na)	High light output, rugged	Geophysical, general radiation detection
CsI(undoped)	Fast, non-hygroscopic	Physics (calorimetry)
CaF_2(Eu)	LowZ, high light output	p detectors, a/p phoswiches
$LaCl_3$:Ce(0.9)	Very high light output, very good energy resolution	High resolution scintillation spectroscopy, Health Physics environmental monitoring
$CeBr_3$	Very high light output, very good energy resolution, low background	High resolution spectroscopy, low background applications
^{6}LiI(Eu)	High neutron cross-section, high light output	Thermal neutron detection and spectroscopy
^{6}Li-glass	High neutron cross section, non-hygroscopic	Thermal neutral detection
BaF_2	Ultra-fast sub-ns UV emission	Positron life time studies, physics research, fast timing
YAP(Ce)	High light output, low Z, fast	MHz-X-ray spectroscopy, synchrotron physics
LYSO	High density and Z, fast	Physics research, PET, High Energy Physics
BGO	High density and Z	Particle physics, geophysical research PET, anti-Compton spectrometers.
$CdW0_4$	Very high density, low afterglow Slow decay times	DC measurement of X-rays (high intensity), readout with photodiodes, Computerized Tomography (CT)
$PbW0_4$	Fast, high density, low afterglow	Physics research (calorimetry)
Plastics	Fast, low density and Z high light output	General counting, particle and neutron detection.

Table 4.1 - Material, properties and applications of the principle types of scintillators [78].

4.2 Muon Portal Project: Detector Architecture

4.2.1 Overall sensitive volume

A schematic picture of the detector is shown in Figure 4.1. It includes four logic X-Y planes with dimensions 3x6 m^2 corresponding to eight physical planes, one for each direction. The detection planes of each tracker are spaced 140 cm, while the inner planes are separated by 280 cm; in this manner a standard container can be easily inserted (dimensions 244×259×610 cm^3 or Twenty-foot Equivalent Units, named TEU). In this way, the spatial resolution of the order of a few mm is suitable to provide a good tracking capability for each muon, allowing the reconstruction of the incoming and outgoing muon tracks and, consequently, the scattering angle with a geometrical angular resolution of about 0.2 degrees [79].

The detection planes are supported by an iron-steel mechanical structure, in order to minimize the material budget crossed by the charged particles.

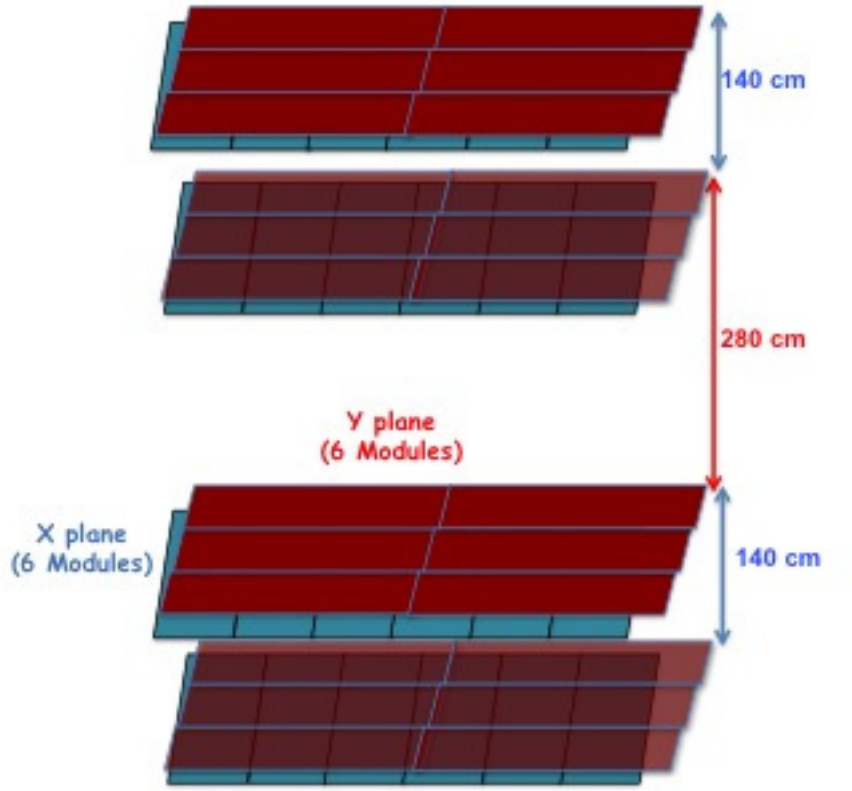

Figure 4.1 - Sketch of the detector layout. The two trackers consist of eight *X* or *Y* planes in total, with 6 modules for each are visible.

4.2.2 Modules

For each of the eight detection planes, there are six identical modules, which cover both the *X* and *Y* coordinates with a modular structure. They are placed in a crossed configuration as represented in Figure 4.1 with blue and red colours. In turn, this configuration can minimize the dead area, which is in the order of 0.1% of the total sensitive area. Each module of 1x3 m^2 size consists of 100 extruded plastic scintillator strips.

Several considerations motivated the choice of a modular structure. Module length is equal to strip and assembly table lengths. 3 m strips have a higher efficiency than those of 6 m, due to the light attenuation. Moreover they are more handy.

A unique coincidence signal between two fibers of the same strip, instead of two signals from each sensor coupled to a fiber, allows reducing the number of photo-devices required. Having 4800 strips in total, 4800 double SiPMs in a single package may be used instead of 9600, each with an individual package. As a consequence, the required front-end and read-out electronics is also reduced and it has a modular architecture, as will be explained in Section 4.3.

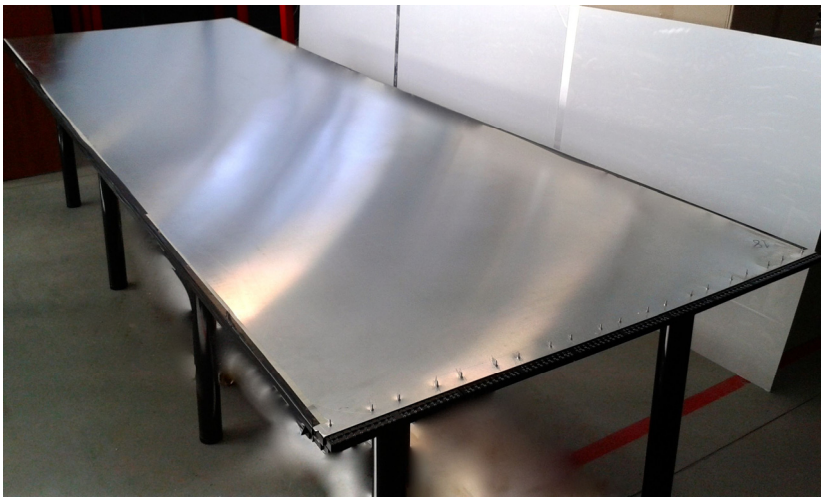

Figure 4.2 - Picture of a complete module.

Figure 4.2 shows a picture of a complete module placed on a supporting table. One of the two aluminum covers, 3020x1000 mm^2 size and 1 mm thick, is clearly visible. One side is coated with a bi-adhesive film, to which 100 strips 3003 mm long are glued. Two WLS fibers are inserted into two grooves of the strip so that they protrude by a few mm from both sides.

At one end, the strips protrude by a couple of millimeters, while at the other end the aluminum cover protrudes by about 2 cm. In this 2 cm gap between the aluminum covers, a plastic cookie like the one shown in Figure 4.3 is inserted, in order to guide the fibers exactly in front of the SiPMs. For each module ten cookies are needed, one for 10 strips, with a total of 20 WLS fibers of 1 mm thick. The fibers are fixed to the strip and to the cookie with optical glue. In this way, it is possible to polish both ends of each fiber, along the entire 100 cm width of the module. The mirror polishing is performed with a diamond milling head spinning at high speed that is moved along the entire width of the module. The opposite side of the module, where there are no cookies, is covered with a reflective Mylar layer to improve the efficiency of light collection.

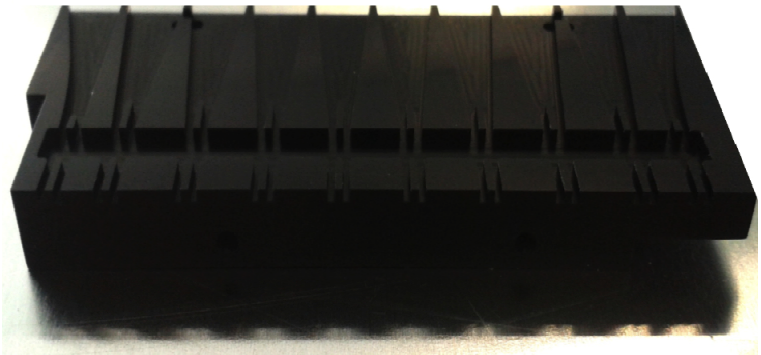

Figure 4.3 - Picture of a cookie that guide the WLS fibers to the SiPMs.

4.2.3 Scintillating strips

The chosen 1x1x300 cm^3 strips are coated with a reflective material (TiO_2). In each one, two WLS fibers are inserted into two grooves. The fibers are optically and mechanically coupled to the photo-sensor placed at one of the fibers ends. A strip designed with a single fiber to be read from both ends would halve the amount of WLS fibers, but it would not produce greater benefits over our solution.

Differences between strip models are related to different physical properties such as the extrusion technique, the bulk chemical composition, the nature and concentration of the fluorescent dopant, the number, position and dimension of the fibers grooves and also the technology used to coat the strips with diffusive reflective materials. Another important aspect for the optimization of light collection is transparency and reflectivity maximization and the matching between the scintillation light emission spectrum with the fiber absorption spectrum. The two fibers transport part of the light produced in the strip by the crossing particles and it is re-emitted at their ends at a wavelength close to the photo-sensor absorption peak.

The reduced number of photosensors is in favour of the front-end and read-out electronics costs and sizes. In fact, there are 48 front-end boxes instead of 96. They accommodate and cool SiPMs without the introduction of additional dead space between modules.

The choice of strips dimensions is mainly due to spatial resolution desired for our detector. GEANT4 [80] simulations have shown that a spatial resolution of about 3 mm is required in order to identify high-Z materials of at least 1 dm^3. This resolution can be obtained by the *PORTAL* detector, taking into account that X-Y layers of a same plane are separated by two layers of aluminium about 1 mm thick, each other.

4.3 Conversion of the scintillating light by Silicon photo-multipliers

4.3.1 Optimization of light collection

The use of WLS fibers to transport the light produced in the scintillating strips greatly reduces the light absorption along the strip and allows to adapt the emitted light wavelength at more appropriate values close to the region of the photo-sensors maximal sensitivity. In order to choose the best configuration for the final design of the detector and to optimize the light collection at one end of the strip taking into account the working conditions, a series of experimental tests supported by proper simulations have been conducted on several prototypes of scintillator strips and WLS fibers from different suppliers. The results are shown in Figure 4.4. Among 1 cm^2 cross-section strip prototypes, we have selected the following possible configurations: Amcrys

Fermilab National Accelerator Laboratory (FNAL) strips with a centred 3 mm hole able to accommodate two 1 mm WLS, as well as FNAL or Uniplast strips [81-82] with two 1 mm grooves located on the same side. This last one is the final configuration chosen.

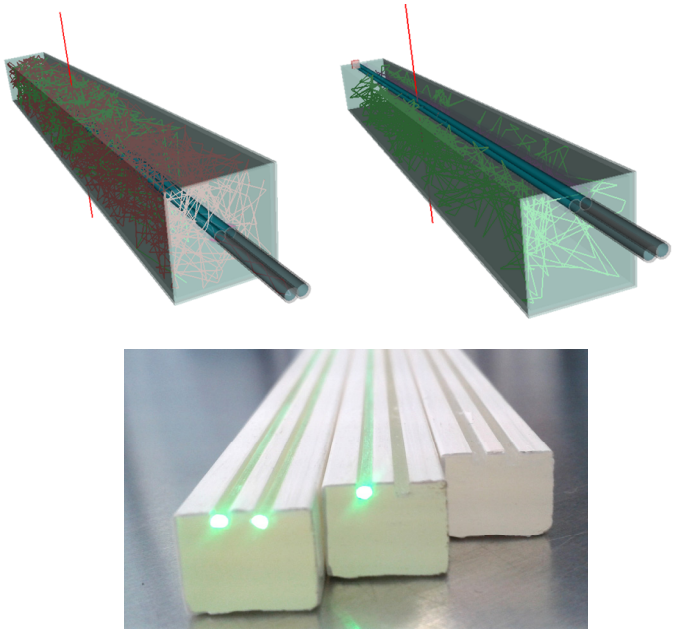

Figure 4.4 - (Top) Sketch of possible designs of extruded scintillator strips with two WLS housed into two groves. (Bottom) Picture of the final configuration chosen, including Amcrys strips.

For the choice of the fibers, we have selected those with the most suitable emission spectrum matched to the PDE of the SiPMs and have the highest attenuation length for the spectrum of light to be transmitted.

Obviously, also the light passing through the fiber is attenuated and it is important to know how this happens. As already mentioned in eq. 2.1 of Chap 2, the light intensity *I(x)* that reaches the SiPMs depends on the distance *x* with respect to the point where the light was produced:

$$I(x) = I_0\left(ae^{-\frac{x}{\lambda_s}} + be^{-\frac{x}{\lambda_l}}\right). \qquad (4.1)$$

For WLS fibers, λ_s is of a few tens of cm, and its effect can be neglected at distances of 50 cm. In this case, the above expression reduces to

$$I(x) \approx I_0 e^{-\frac{x}{\lambda_l}}. \qquad (4.2)$$

Tests and simulations were performed on the Amcrys FNAL and Uniplast strips accommodating BCF91A Bycron or Y11 Kuraray fibers [83-84].

The tests were performed with different strips and fibers placed inside a dark box of dimensions 50x50x100 cm^3, varying O_V and Th_{pe} of the photo-sensor [85]. Fibers into the groove were fixed without using glue, which is not indispensable for the optical coupling.

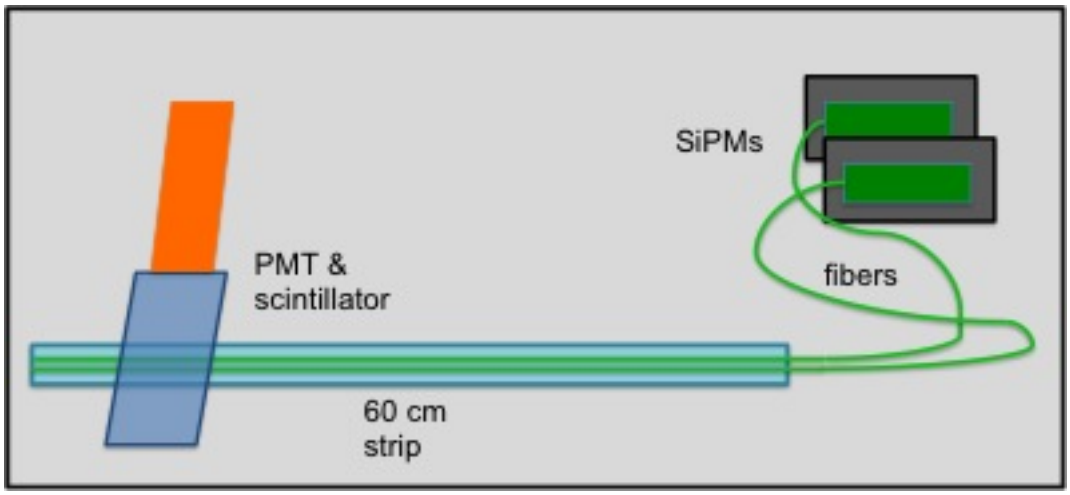

Figure 4.5 - Sketch of the experimental set-up. A 60 cm long scintillating strip, with two WLS fibers inserted (3.5 m long) read at one end by SiPMs. An additional scintillator, operating in coincidence with the two SiPMs was used as a muon trigger.

A scheme of the experimental set-up is shown in Figure 4.5. It includes a 60 cm long strip, which lodges two fibers read by as many SiPMs, together with a 12x12x1 cm^3 muon scintillator placed above the central part of the strip to select only particle detected in coincidence, in order to reduce the noise due to the SiPM dark count rate. We used 60 cm long strips with two fibers about 3.5 m long. The electronics chain used for the read-out of the SiPMs consists of an amplifier module (ORTEC FTA 820, gain A_0 = 20 and Gain-Bandwidth GBW_0 =7 GHz) followed by an analog fan-in/fan-out (Lecroy 428F, gain A_L = 1 and GBW_L = 140 MHz). Than the signals are recorded by a digital oscilloscope (LeCroy Wave Runner 610Zi). A logic coincidence unit (Lecroy Mod 465) provided the coincidence signal with the outputs of a leading edge discriminator (CAEN N428, BW = 20 MHz). The coincidence unit gave the possibility to select single, two-fold or three-fold coincidences and its output was also used for counting the events. We considered only the amplitude of the signals produced by the SiPM, because the electronic chain of the final *PORTAL* detector needs voltage signals and not charge.

Figure 4.6 shows the cosmic muons rate detected by SiPMs (made by STMicroelectronics), that will be described in the section 4.2.3, placed at one end of a 60 cm Uniplast strip (Vladimir in Russia), as a function of the distance crossed by photons into the fiber setting two different SiPM thresholds. The strip has 1 cm^2 cross-section with two 1 mm grooves along the same side. The power supply voltage for the SiPMs is around 30 V [86].

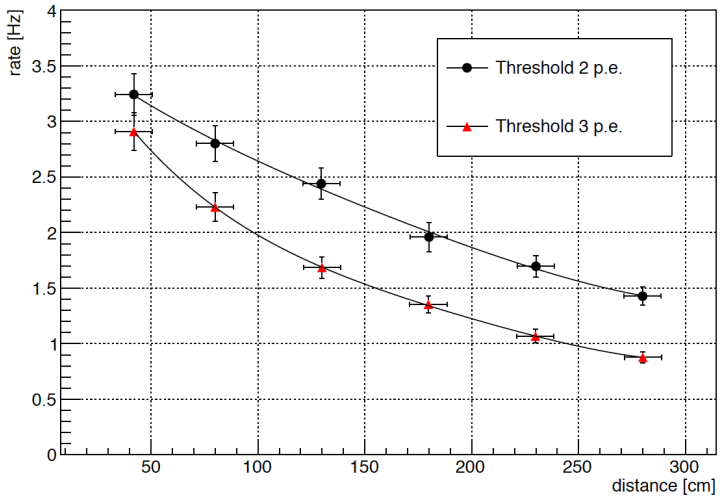

Figure 4.6 - Cosmic muons rate versus the distance from the SiPMs, detected employing Uniplast strip sample with Kuraray Y11 (200) fibers embedded. The data are reported for two different acquisition thresholds (given in terms of photoelectrons number).

As follows from the curves in Figure 4.6, the choice of the threshold (reported in number of photoelectrons) influences the uniformity of the detection efficiency along the length of the strip. It is important to underline that, even if each individual SiPM is quite noisy at low thresholds, the 8-fold coincidence between the detection planes allows minimizing the spurious coincidence rate. The results in Figure 4.6 joint with detailed GEANT4 simulation studies on the light transport inside the strip, suggested the use of thicker strips (at least 1 cm thick, instead of 0.7 cm) in order to preserve the detection efficiency along the strip above 90%.

The evaluation of the optimal fibers is based on home made simulations and tests, in addition to the results obtained from previous well-known experiments.

The graph in Figure 4.7 shows the comparison between Kuraray and Bicron light emission yields as a function of the traversed length. Figure 4.7 was realized by the OPERA experiment staff [87-88].

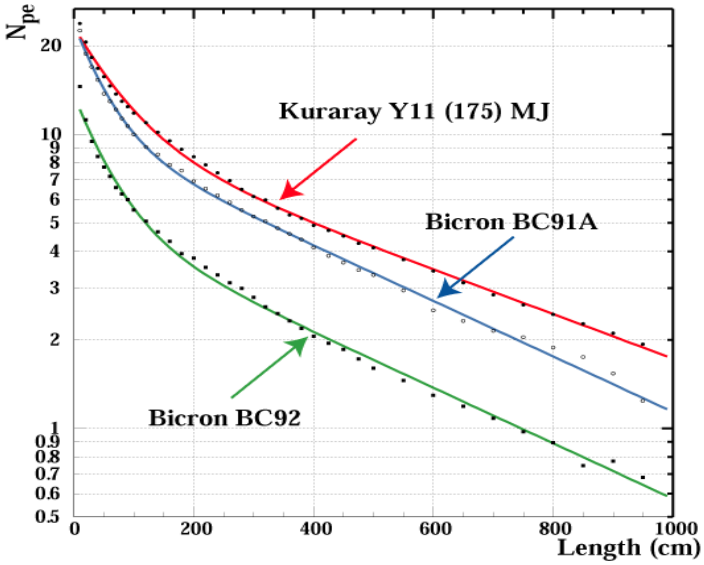

Figure 4.7 - Comparison between Kuraray and Bicron light emission yields, as a function of the length crossed by light inside the fibers. These tests were conducted by the OPERA experiment [87-88].

The graph in Figure 4.8 reports the Kuraray fibers light response for three possible configurations by irradiating fibers (not covered by an external scintillator) with a blue LED light (blue light is the wavelength emitted by the plastic scintillator in response to crossing muons) and by using an external scintillator irradiated with a UV LED or with a 90Sr sources. For all of the considered set up, the fibers are sensitive to the radiations and they follow the exponential trend of eq. (4.2). This test is useful to study the light yield variation of Kuraray fibers with respect to the distance from the photosensor.

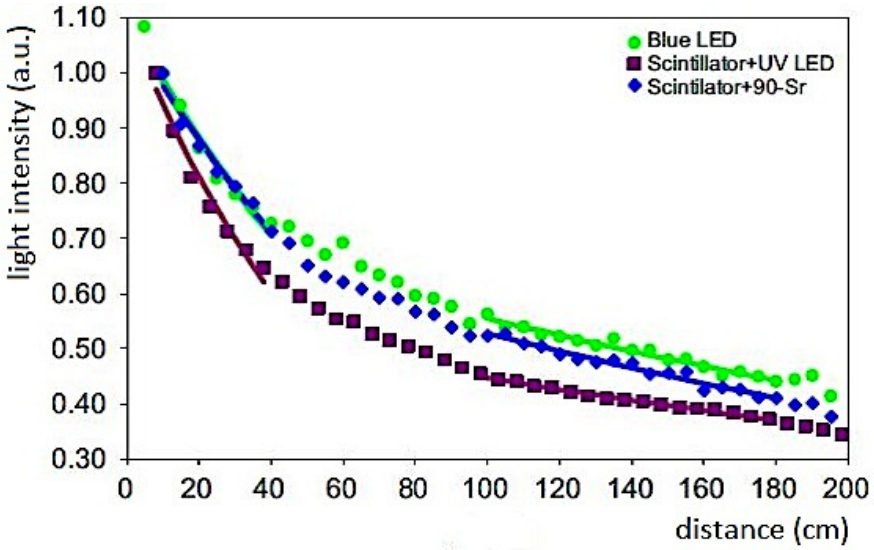

Figure 4.8 - Kuraray Y11 (200) response to different sources, with or without the external scintillator.

The evaluation of the tests results suggests using the Kuraray Y11 (200) fibers for the *PORTAL*, because they have shown the best performances in terms of number of photoelectrons detected by a suitable photo-sensor, varying the distance from it.

4.3.2 Optical glue and reflective layer

At first, it was evaluated the possibility to fix the fibers into the strip grooves with optical glue. For this purpose, a test was carried out with the 26x10 mm^2 Amcrys strips and an improvement in the collection of light of the order of 35% was recorded.

However, the final solution chosen does not foresee the use of optical glue for several reasons. The main motivation is that light yield is enough to record all *good events* (muons crossing all detection planes). In addition to the costs, the operation with optical glue would also require extra manpower and would therefore only be used if absolutely essential.

The read-out of the scintillation light only at one end of the strip reduces the collection efficiency for the points away from the light sensor. In order to collect a part of the light that travels in the opposite side to the SiPM, we placed on the open-end of the strip a reflective aluminized Mylar layer. As a result, there was an improvement in the collection efficiency of the strip, up to 35% for distances close to 3 m from the SiPM. In particular, setting a threshold Th_{pe2}, the efficiency is practically constant along the strip. This solution was already used by other experiments [89].

4.3.3 SiPMs characterization

Characterization of custom designed SiPMs to convert the scintillating light into an electrical signal is described in this section. Different SiPM prototypes, both with the P-on-*N* and *N*-on-*P* technologies were produced and tested by *STMicroelectronics* in Catania (Italy) [90] in order to maximize the photon detection efficiency (PDE), the fill factor with a low cross-talk and dark count rate. STMicroelectronics designed and supplied also the cookies chosen for the Project already shown in Figure 4.3.

Figure 4.9 shows the comparison between PDE measurements carried out at two values of O_V on a SiPM device similar to the one that will be used for the Project.

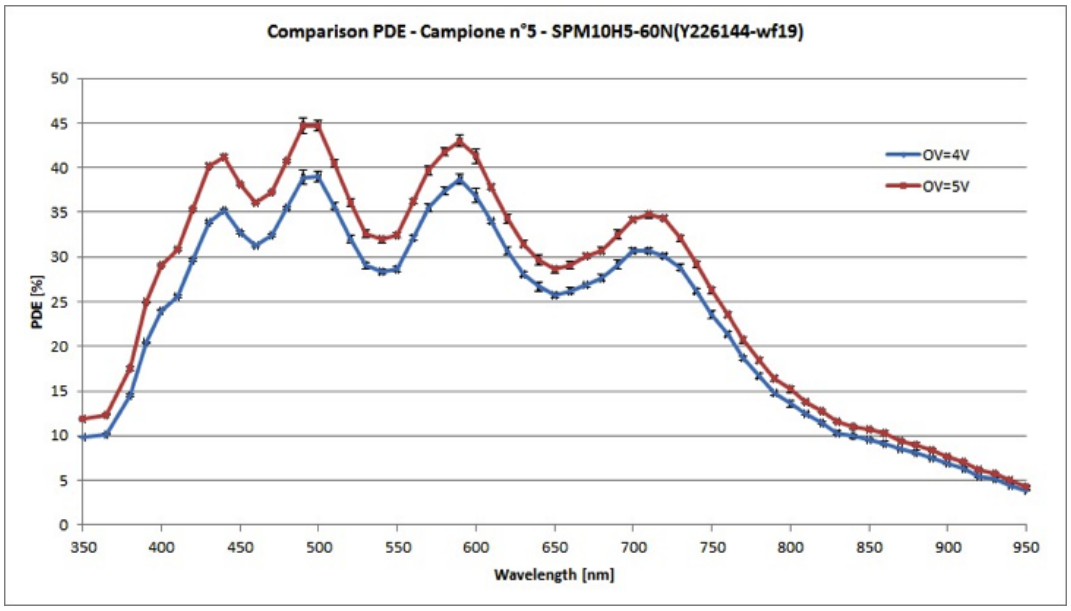

Figure 4.9 - PDE measurement comparison at O_V=4V and O_V=5V and temperature T=28°C.

It is a *N*-on-*P* sensor chip with 4 SiPMs: two couples respectively with pixel size 60 μm and 75 μm. The PDE is about 40% and the fill factor 67%. The main characteristics of the package are reported in Tab. 4.2.

Parameter	Unit	Value
SiPM array size	μm^2	3968 x 4464
Array dimension	number	64 x 72
Cell in one SiPM pixel	number	1145
Geometrical fill factor	%	47
Cell size	μm^2	62 x 62
Total geiger cell area	μm^2	124 x 124

Table 4.2 - Main characteristics of the Silicon photomultipliers employed in the present investigation (STMicroelectronics Mod. 4SPM20-62N).

All the measurements reported in this chapter were made by using the same two identical devices 4SPM20-62N. The photo-sensor to be employed in the Muon Portal Detector requires performances more appropriate to adapt both the mechanical requirements and the optical properties of the strips and the WLS fibers. Therefore, the SiPMs have been planned with a higher fill-factor, smaller cells and a larger gain. The size of the SiPM will be circular with a diameter of about 1.5 mm, with a reduction factor of about 2.5 than the area of the device used in the tests. The centre-to-centre distance of the two SiPMs is chosen to optimize the coupling with the two fibers. In comparison with the tested SiPM prototype, we expect a lower dark current and a higher PDE, but the same spectrum sensitivity. In the meantime, we have started with their

characterization. The results obtained with the preliminary described prototypes will be improved with the final chip.

The layout of the final chip designed for the Project is shown in Figure 4.10.

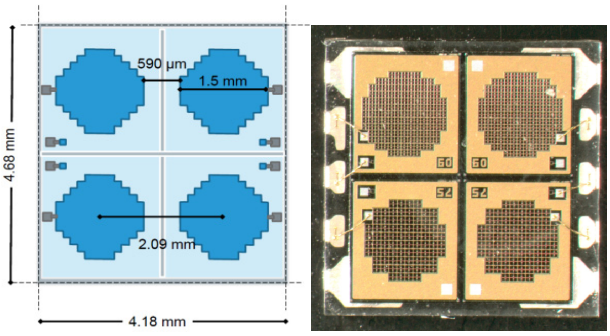

Figure 4.10 - Layout (left) and picture (right) of the SiPM chip MUON-60 (60 µmx60 µm is the single cell size, while the diameter of the total circular sensitive is 1.5 mm), foreseen for the Muon Portal Detector, designed by STMicroelectronics. Just two of the four SiPMs will be used for each strip.

By using the electronics chain reported in Figure 4.5.the amplitude spectra of the signals from the SiPM were measured [85]. The SiPM was further darkened with a layer of black tape. The measurements were performed at various bias, with O_V values of 2.4, 3.4, 4.2 and 5 V.

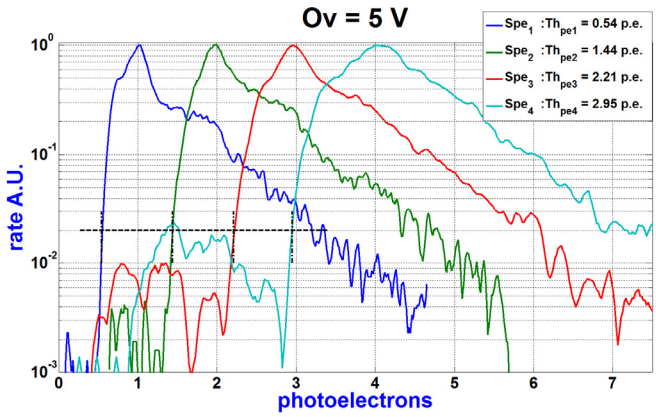

Figure 4.11 - Normalized amplitude spectra obtained for different discriminator thresholds.

Figure 4.11 shows the spectra Spe_1, Spe_2, Spe_3 and Spe_4 in a semi-logarithmic scale at O_V = 5 V. Spe_i is the spectrum obtained setting the comparator threshold at a level equivalent to *i* photoelectrons [85]. Each spectrum is normalized respect to its maximum. The horizontal axis is expressed in number of photoelectrons. From the peak of each spectrum it is possible to obtain a threshold value Th_{pei}, in photoelectrons number (p.e.), defined as one fiftieth of the maximum (marked with black dotted lines in Figure 4.11).

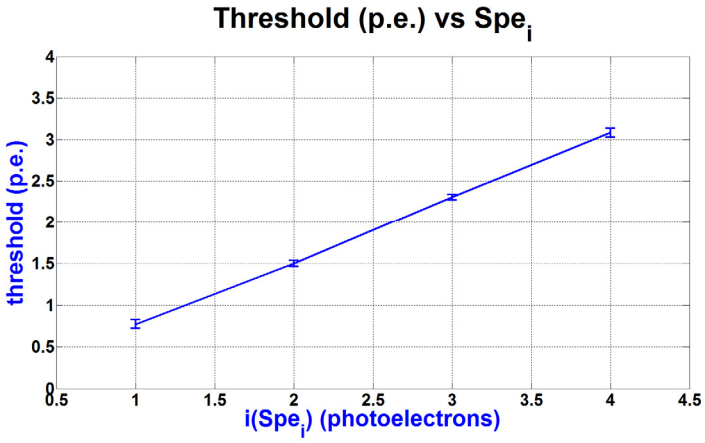

Figure 4.12 - Threshold vs Spei peak in p.e. unit.

The plot in Figure 4.12 shows the threshold Th_{pei} in p.e. unit as a function of the S_{pei}.

In addition, tests shown that by setting the comparator level, i.e. at 1.5 p.e., the threshold is fixed at 2 p.e., just with small dispersions by a few %, despite of the variations in the Ov.

Other measurement results are reported in Figure 4.13; the spectra Spe_3 is obtained at various voltages and two different distances *d* between the center of the strip and the fiber end where the SiPM is placed (50 or 250 cm) [85]. For each spectrum, O_v (in volts), the Centre of Mass (CoM) and the threshold Th_{pe} (both in p.e.) are given.

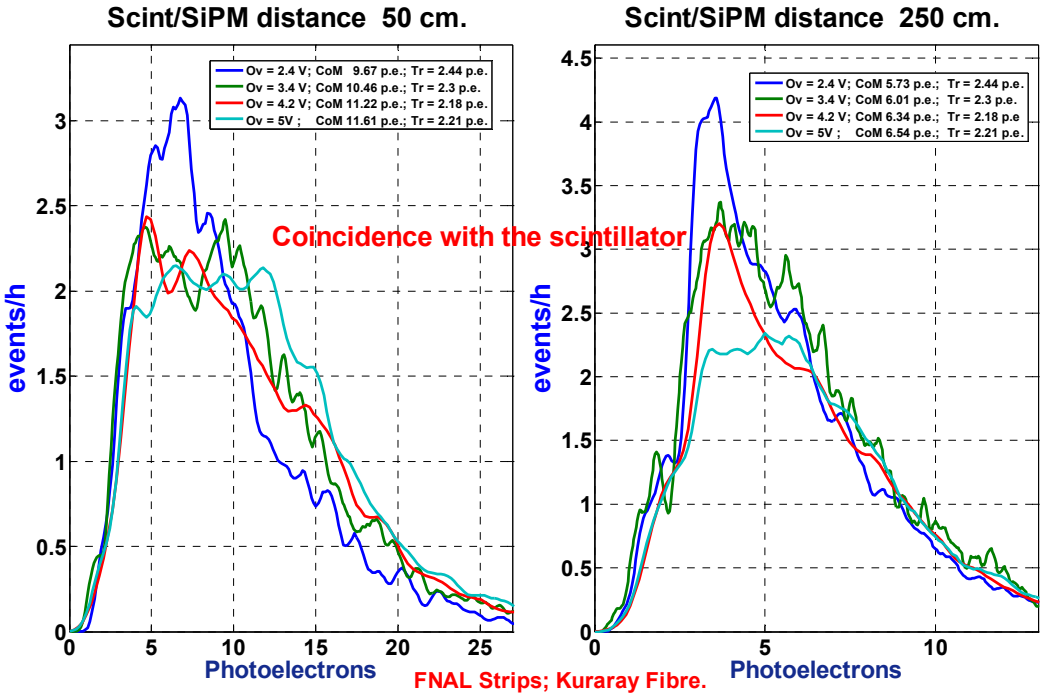

Figure 4.13 - Spe3 at 50 cm (left) and at 250 cm (right).

4.4 Measurements of the SiPMs Breakdown Voltage (BV)

A batch of 5000 SiPMs was produced and encapsulated in a surface mount optical package (SMD) by STMicroelectronics. A custom procedure has been implemented for the characterization of such devices. Placing the device to be tested with its proper socket inside a black box, it was biased by a Keithley 6514 picoammeter/voltage source [85]. The Keithley was also used to read the current from the SiPM and to transmit data to a data acquisition PC. In order to measure the complete I-V curve in an automatic way by setting the bias voltage and reading the corresponding current in the device, a LabVIEW program has been developed. It runs on the PC communicating with the Keithley device by an USB port. Starting from a bias voltage of 25 V up to 35 V in steps of 0.1 V, the program is able to find the Breakdown Voltage *BV* value for each SiPM under test by reading the corresponding current I_{BV}. *BV* is defined as the voltage at the knee of the I-V curve when the device is reverse biased and is calculated as the intercept of the low current fit line with the zero current axis, as indicated in Figure 4.14.

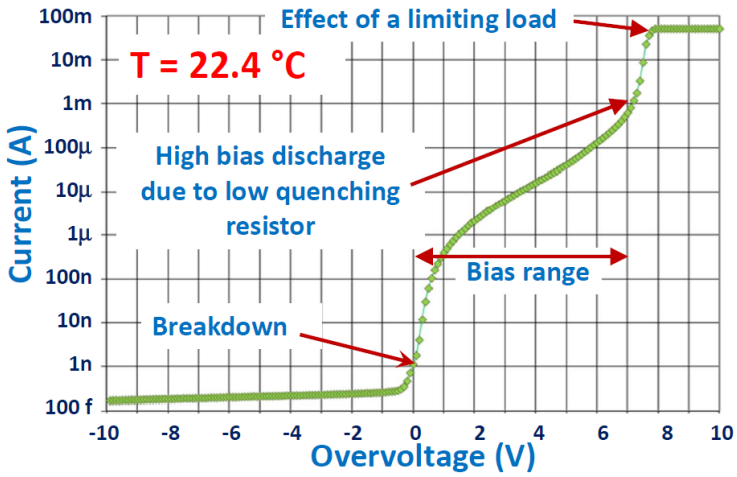

Figure 4.14 - Typical reverse characteristic curve for the SiPM Mod. 4SMP20-62.

After the construction of the I-V curve, the SiPMs that do not satisfy stringent criteria on the *BV* are rejected (i.e. a good compromise is $27 < BV < 29$).

Other testing criteria are applied to the current values corresponding of $BV + 5$ V and $BV - 2$V and the effectiveness of a device is evaluated in a simple way, thanks to the switching of appropriate signalling LEDs [86].

The reverse I-V characteristics curve for one of the SiPMs under test is shown in Figure 4.15a. For the device under test it was found a *BV* of 27.4V. The *BV* distribution

of the 1622 devices already tested is reported in Figure 4.14b. The mean value is 27.4 V with a standard deviation of 205 mV.

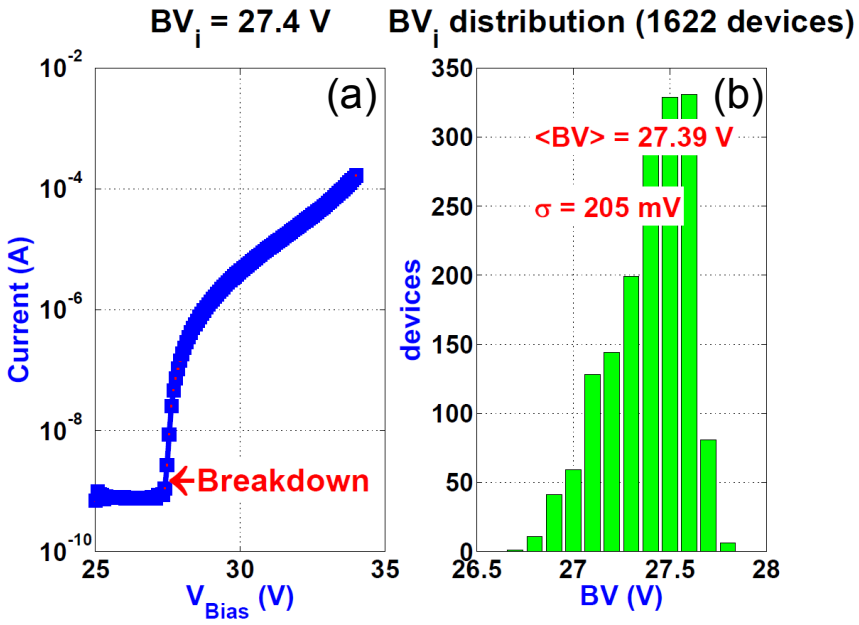

Figure 4.15 - (a) I-V characteristics curve for a tested MUON60 device. (b) *BV* distribution for the 1622 devices already tested.

However, it must be remembered that *BV* depends on the temperature and it raises approximately by 28 ± 3 mV/°C. In the present tests, the *BV* was measured at temperatures of T = 22.4 ± 0.3 °C.

Some alternative methods have been used for the measurement of *BV*. For example, it was performed a measurement by using a pulsed laser that illuminated the SiPMs in the dark box. The SiPM signal was amplified with ORTEC FTA 820 amplifier (gain A_o = 20) and then recorded by a digital oscilloscope that measured the SiPM amplitude in a gate triggered by the laser. The resulting spectrum is pulse height, with many equally spaced peaks. We can calculate the best amplitude value of the pulse V_{S1} produced by one p.e. as the average value $\langle V_{S1} \rangle$ between the amplitude differences among the amplitude V_{Sn+1} produced by n+1 p.e. and the amplitude V_{Sn} produced by n p.e.. *BV* can be determined by gradually decreasing V_{bias} and measuring $\langle V_{S1} \rangle$ each time, because the SiPM stops working when the voltage V_{bias} is lowered down to *BV*. The graph of $\langle V_{S1} \rangle$ versus V_{bias} intercepts the axis for $V_{bias} = BV$.

Figure 4.16 shows the peaks ranging from 4 to 13 p.e. for a bias voltage of 29 V. Each peak corresponds to an integer number of p.e., so, even if the intensity of the laser light is varied, the location of the peaks is the same.

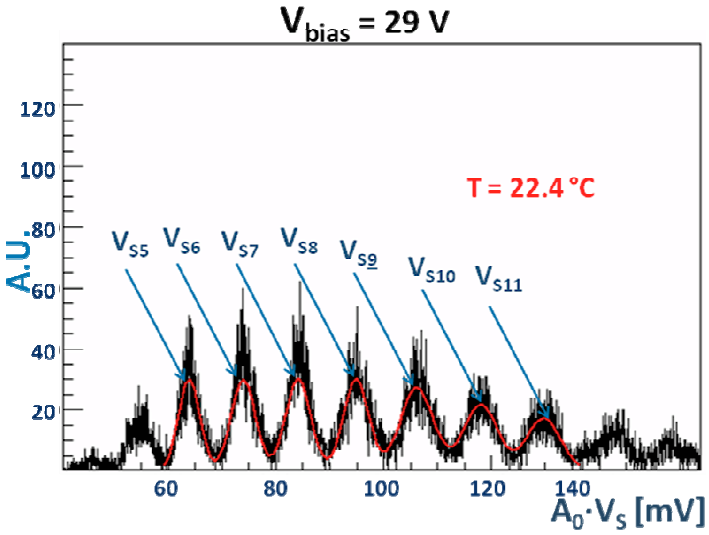

Figure 4.16 - VS3-VS13 pulse height spectra at T=22.4 °C.

Figure 4.17 shows the average value $\langle V_{S1} \rangle$ as a function of V_{Bias}. The intercept with the horizontal axis gives a value $BV = 27.6 \pm 0.2$ V at 22.4 ± 0.5 °C, a result very similar to that obtained using the Keithley generator.

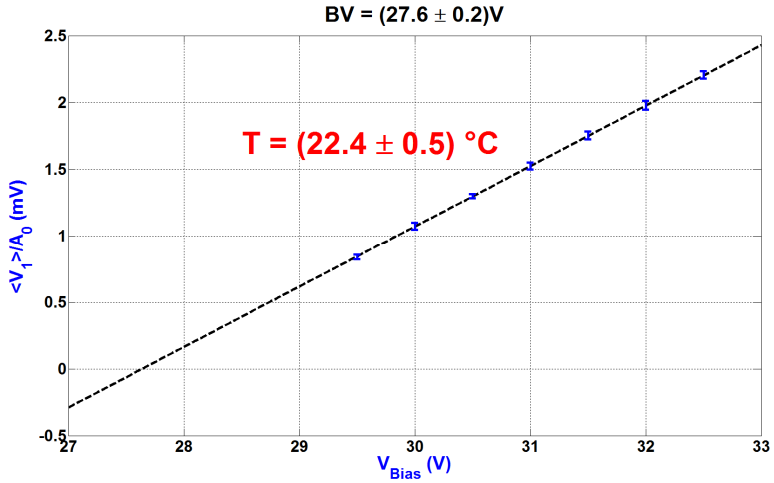

Figure 4.17 - BV determination by using laser pulses.

However, the latter method is more expensive in terms of time required and electronics costs. As a consequence, in order to test the 5000 SiPMs of the Muon Portal project, the first method will be used to characterize the remaining devices.

4.5 Front-end and read-out electronics

The basic considerations from which our detector was designed are the achievement of required performances with reasonable costs, manpower requirement, timing assembly and easily replaceable components.

These needs have been met by providing a modular architecture, as already mentioned in section 4.1.2, including front-end and read-out electronics. The number of read-out channels is lower than the number of initial signals, thanks to the use of compression strategy: starting from 9600 channels they are reduced up to 960. This contributes to a significant reduction in cost and size of electronics, without compromising the performance of the detector. The strips sizes are selected in order to get the desired angular and spatial resolutions. The application of the reduction strategy does not produce any lost of information due to the relatively very low rate of cosmic rays with respect to the acquisition rate.

From the results of simulations, applying cuts to reduce the noise of photosensors, it has been estimated that the rate of muons expected for each plan is 8.1 KHz. In order to require the coincidence to the eight detecting planes, the muon rate is reduced by up to 320 Hz.

In this section, the front-end and read-out electronics components are described.

The read-out electronics is made of Data Acquisition DAQ boards based on programmable logic FPGA, housed into a PXI-bus crate. The chassis is equipped with a real-time module, for correlating signals from all the planes and data flow towards the data acquisition system, and a GPS module for time synchronization.

4.5.1 Application of the smart read-out strategy

In this section, the application of the reduction channels strategy (already explained in Sections 1.2.3 and 2.2.2) to the Muon Portal detector is described.

Each detection module has one hundred strips with two WLS fibers inside, for a total of 200 signals. The 200 signals are seen by as many SiPMs housed into ten Front-End Cards (FECs). The 20 signals arriving to a FEC, sorted two by two in correspondence of each strip, are amplified of about 30 times by a very fast operational amplifier, the THS3201 (1.8 GHz GBW). The resulting single photoelectron signal is about 27 mV in amplitude and 20 ns wide (at O_V of about 2.4 V). All FECs are connected to a main board, unique for each module. There, the reduction channel strategy is applied. Indeed, 10 neighboring analog signals of a FEC, one signal for each strip, are summed and amplified 3 times by another THS3201. The analogue outputs of the other remaining SiPMs of the FEC are then summed to signals of the same order (1^{st}, 2^{nd}, etc…) coming from the other FECs and amplified by a factor 3. After the application of the reduction strategy, the analog signals are then compared to a remotely settable threshold for binary conversion. Thanks to the application of the channel reduction strategy in the proposed system, it is possible to reduce the number of read-out channels by a factor 10, for a total of $2\sqrt{100} = 20$ output signals for each module.

4.5.2 Electronics architecture

The SiPMs are read by a suitable front-end electronics. A dark front-end box is provided, with a long slot where the module is wedged (see Figure 4.18). It accommodates the final part of the Sci-Fis, the front-end boards housing the SiPMs with their power supply, amplificators, fast comparators, monostables. The connection to the acquisition electronics is provided using a suitable 15 m cable. On top of the dark front-end box, it is possible to see the fans for the air cooling of four Peltier cells that are used to control the temperature of the box.

The front-end boards consist in 10 FECs housing the SiPMs, which are inserted and screwed to the cookies from the back and in the main board. The latter is able to process the signals (amplification, application of reduction strategy, comparison with a threshold and stretching of the signals) to be transmitted to the read-out system. Each of the FECs is connected to the main board by mean of a flat cable.

Figure 4.18 - Dark front-end box.

A remote adjustable power supply is required to use SiPM sensors as collectors of the signals coming from the fibers. The power supply is able to compensate the variations of the intrinsic characteristics (gain, PDE, dark current) caused by the environment.

The power supply section and the temperature controller are able to stabilize the working points of the SiPMs, which were suitably selected to have almost identical characteristics.

The temperature conditioning (sensors and actuators), power supply, control and communication (Gbs Ethernet) systems are managed by an unique Semi-Custom Front-end chip (FPGA Front-end). ADAM 4570 modules [91] are devoted to the control of the temperature, voltage and current parameters of the front -end.

It is possible to summarize the working principle of a read-out system as follows. For each detector module, the 200 channels are read by many SIPMs. Thanks to a smart read-out strategy (section 4.3.1), the output channels are reduced by a factor of 10. After the application of the reduction scheme, there are 960 digital channels coming from a fully completed detector, 20 per each module, which produces flows of 20 bit words. Indeed, after the second amplification in the main board by the THS3201, the 20

analogical signals from each module are compared to user-defined thresholds. Then, they are stretched by monostables (50 ns). After passing the monostables, the 120 signals from a *X* or *Y* plane are sent by suitable cables to a NI PXI-7813R acquisition board with 160 Digital I/O (Figure 4.19). The 40 remaining lines are used to adjust the thresholds of the DAQ and to manage the voltage/current and temperature controls.

Figure 4.19 - National Instrument PXI- 7813R with 160 digital I/O.

An acquisition software for pre-analysis of data from the SiPM processes the output signals from the front-end boards and manages controls. The programmed logic VIRTEX-II FPGA Module 40 MHz, housed into each board, samples the outputs from the front-end module, decodes the hit strip and produces a label frame for each event. The data are pre-analysed and stored into a data acquisition PC. In total, for the read-out of the overall detector, eight National Instruments PXI-7813R boards are connected by PXI bus in DMA-access to a real-time module (NI PXIe-8135) in a crate to correlate the signals from all the detection planes. The read-out is performed in real-time with a module that calculates the entrance and exit tracks for each event. In addition, a GPS time-stamping unit (NI PXI-6682) housed into the crate, correlate the arrival of muons in the Muon Portal detector to additional detectors located around it. This will allow off-line correlation of the events measured in independent detectors, with a time precision of about 40 ns. The complete read-out and DAQ system, including the selected crate, the NI PXI Express 1065 18-Slot Chassis, which houses the controller in addition to the FPGA boards and GPS module is shown in Figure 4.20.

Figure 4.20 - A picture of the PXIe-1065, 18-Slot 3U PXIe/PXI Chassis, including the real-time module, the GPS timing module and the eight PXI-7813 digital sampling board.

Hardware data communication between each detector module and the corresponding acquisition board is performed by the selected MRJ21 shielded cable 15 m with 48 wires (Figure 4.21 on the left), already purchased and being tested. The cable carries 20 output logical signals from the front-end and 4 signals for the management of the comparators threshold of the front-end. The cable, on the other end is connected to an interface board front-end/read-out.

Figure 4.21 - MRJ21 cables 15 m long (on the left). National Instrument cables SHC68-68-RDIO (on the right).

The board, equipped with an input connector and an output connector, has the task of adapting the signals to the standard cables of National Instrument (NI) SHC68-68-RDIO (Figure 4.21 on the right) that carry signals to the acquisition boards NI PXI-7813R.

The board interfacing is currently being tested and the acquisition software is currently being processed. The entire electronics chain was already tested in response to the signal produced by muons in a single detection module. The next step will be the measurement of coincidences between multiple plans, employing the SiPM custom-designed for the project.

A sketch of the complete front-end and read-out electronics is shown in Figure 4.22.

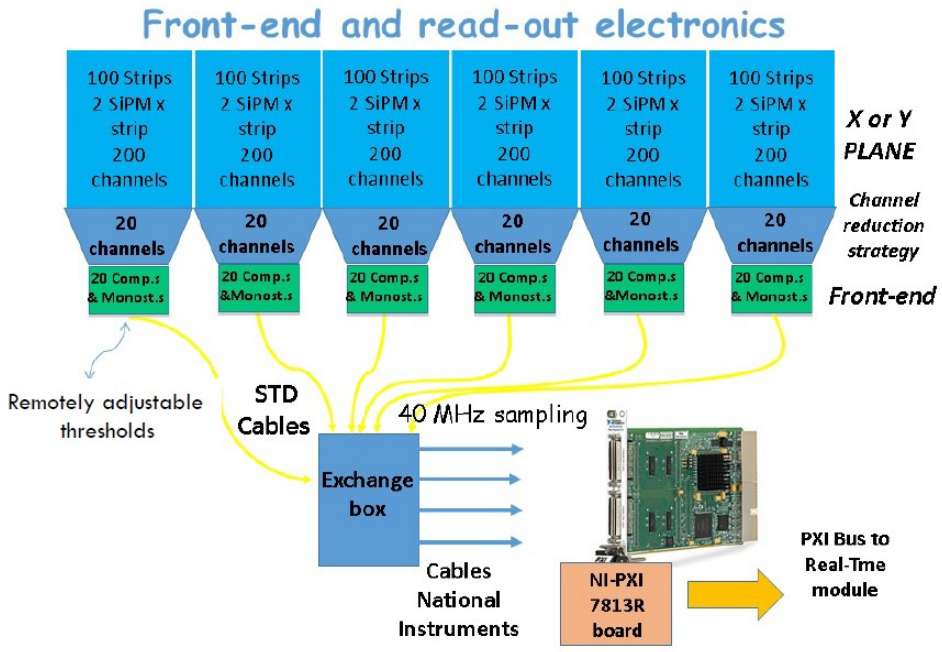

Figure 4.22 - Block diagram of the front-end and read-out electronics.

4.6 Detector simulation and cosmic rays generation

Accurate GEANT4 simulations [80] on the detector response have been implemented in order to well estimate the scattering angles for muons and electrons coming from air showers induced by primary protons as detected by the *PORTAL*, and with the aim to optimize the reconstruction algorithms applied to the tomographic image [92-93]. A picture from GEANT4 simulation is reported in Figure 4.23. Each simulation contains a realistic reconstruction of the Muon Portal detector, including its mechanical supporting structure, the detections planes and a real size container between the trackers. GEANT4 gives the possibility to simulate the transport of optical photons into scintillators and fibers. The resulting values are then parameterized to minimize CPU processing time, the reconstruction of hits and clusters, including those due to electromagnetic showers. Cosmic rays are generated by the CORSIKA (*COsmic Ray SImulations for KAscade*) code, that is a program for detailed simulations of extensive air showers [94]. Simulations are also able to take into account multiple hit events induced by electromagnetic showers of high-energy electrons into the surrounding environment.

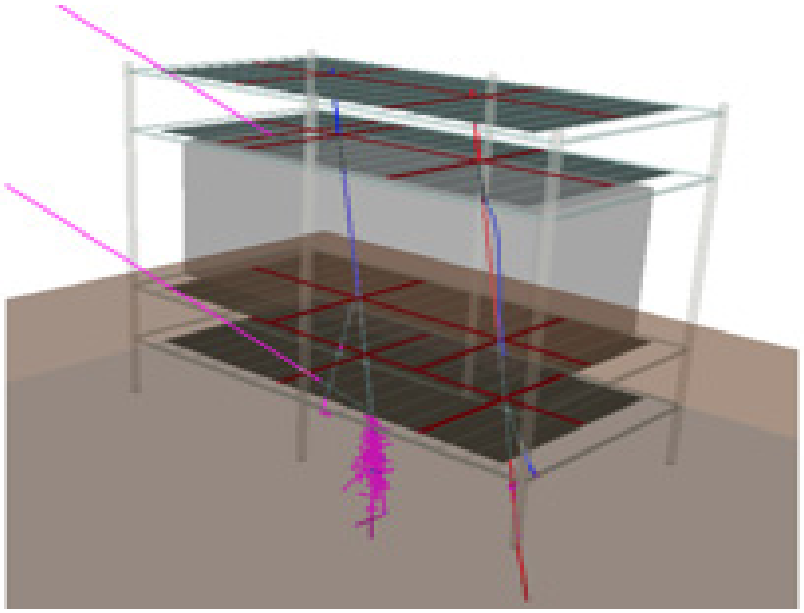

Figure 4.23 GEANT4 simulation of scattering events induced by primary muons, as revealed by a full replica of the detector. A simulated container is visible between the inner detector planes.

4.7 Reconstruction Algorithms

The resulting data from GEANT4 simulations has been used to implement several algorithms for the reconstruction of the tomographic image [95-96].

The simplest method to reconstruct the tomographic image is the POCA (Point Of Closest Approach) algorithm. Starting from the simplified assumption that the muons scattering occurs in a single point, it is able to geometrically find the point of closest approach between the reconstructed incoming and outgoing tracks directions of each muon crossing the inspected container. Consequently, it is easily implementable and provides fast results, useful as first-order approximation to the problem or as a starting approximation for more detailed algorithms. However, it is a purely geometric algorithm that neglects any underlying physics of scattering such as multiple scattering events. In addition, it is not very sensitive to the presence of shield materials surrounding the potential threat and is not able to well localize dangerous materials at the volume borders.

The POCA method images high-Z materials as more dense regions with respect to the background. As a consequence, density-based clustering methods can be exploited for our analysis as improvement of the POCA method.

After the definition of a minimum distance threshold *T* among the objects into a volume, they connect data points, which satisfy a density criterion, defined as the minimum number of objects within *T*.

Several clustering algorithms were tested for the imaging reconstruction of the *PORTAL*. In particular, the Friends-Of-Friends algorithm (FOF) has given the best simulation results.

The FOF method consists in groping all the particles separated by a distance smaller than a given length parameter l_{link}.

Then, the algorithm identifies all particles pairs, which have a mutual distance smaller than l_{link}, and these pairs are designated as friends.

Clusters consist of particles sets connected by one or more *"friendly relations",* so that they could be friends of friends. The linking length is related to the mean particle density number.

In order to reject spurious clusters, i.e. groups of friends who do not form persistent objects in the simulation, another parameter was defined in FOF algorithm: the minimum number of particles N_{min}, in a cluster.

The choice of a N_{min} value sufficiently large allows to eliminate spurious clusters, because they are at most due to noise, so they involve a small number of points.

Finally the EM-ML (*Expectation Maximization-Maximum Likelihood*) methods are iterative algorithms based on the subdivision of the entire volume to be inspected in *k* 3D pixels named voxels (each characterized by a density of scattering λ_k). Thanks to iterative procedures to maximize log-likelihood curve, the algorithms converge to the best set of the parameters λ_k. Even if the computation time is still prohibitive for a real application, a parallel implementation (applied both in the initialization and imaging step of the algorithm) will be applied to allow a real-time application of the method even with a modest number of computing machines.

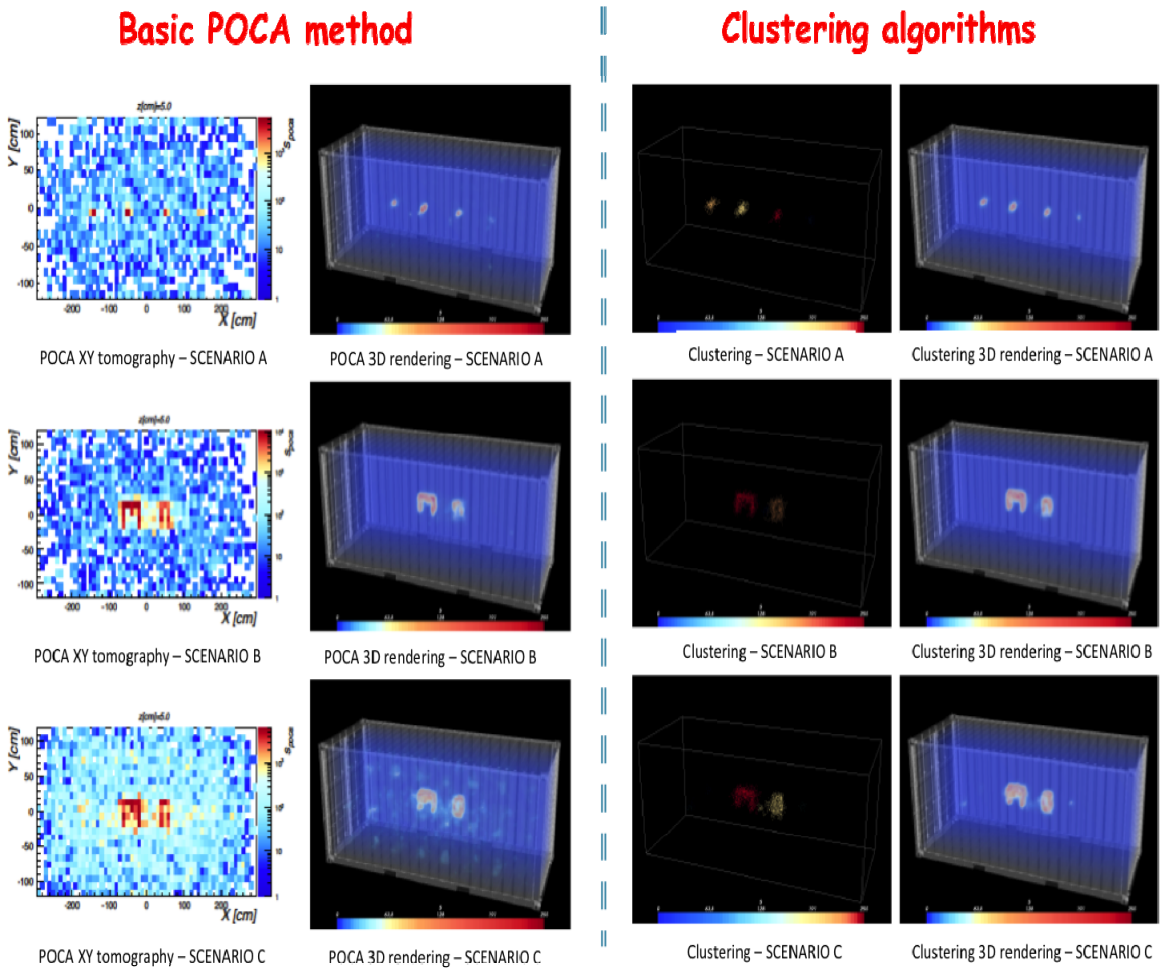

Figure 4.24 - GEANT4 simulation of POCA and clustering algorithms to reconstruct different scenarios: Scenario A: Four threat boxes of different materials (W, U, Pb, Sn) and size 10 cmx10cmx10 cm inserted at the centre of an empty container.
Scenario B: A "MUON " shape built with voxels of size 10 cmx10 cmx10 cm inserted into the centre of an empty container. Each letter is made of a different material: M = Uranium, U = Iron, O = Lead, N = Aluminium.
Scenario C: Same scenario of B. A denser environment is arranged inside the container volume, filled with layers of washing machine-like elements. These are made of an aluminium casing with an iron engine inside with relative support bars and a concrete block.

The algorithms have been tested and optimized over different simulation scenarios [86]. Figure 4.24 shows the GEANT4 simulations of POCA and clustering algorithms to reconstruct three different scenarios (simulation details are reported in the Figure caption). As an example, we supposed to scan a MUON shape inserted at the centre of a TEU empty container (Figure 4.24, scenario C). Each letter is built with voxels of size 10x10x10 cm^3 and is made of a different material: M = Uranium, U = Iron, O = Lead, N = Aluminium. The shape is surrounded by layers of washing machine-like elements, made of an aluminium casing and an iron engine inside, with relative support bars and a concrete block. Each tomographic reconstructed image supposes a statistics of 1 million of events (corresponding to 10 minutes of data taking).

As visible in the Figure 4.24, by using the Clustering and the EM-ML methods, it is clearly possible to distinguish the M and O letters, made by elements with high-Z atomic numbers (Uranium and Lead). On the contrary, by applying the POCA

reconstruction algorithm, a persistent halo slightly increases the size of the letters, especially along the vertical direction. It is a consequence of the basic assumptions of this algorithm. In every case, the EM-ML algorithm reconstructs the target objects with a considerably better resolution. However, the noise induced by the presence of the washing machines is present in both cases and can be reduced by implementing, for example, density-based algorithms.

4.8 Module Tests

4.8.1 Preliminary tests on a complete module

This section presents the first tests results concerning one of the complete modules of the Muon Portal detector. The module was placed on a suitable supporting table, at room temperature (23 °C). The signals coming from the SiPMs correlated to a selected strip (number 17) were considered for the test.

At first, several calibration measurements of the single photoelectron amplitude were performed varying the biasing voltage V_{bias}. The results are reported in Tab. 4.3

Bias Voltage (Volt)	Amplitude (mV)
29.5	20
30	30
31	50

Table 4.3 - Single photoelectron amplitudes at different biasing voltages.

Fixing the SiPMs power supply at V_{bias} = 30V, which corresponds to an Ov of 2.6 V (considering BV = 27.4 V as reported in section 4.3) the dark current rate at room temperature was measured. The result is shown in Figure 4.25. Dark current rate is of the order of 100 kHz for a threshold of 1 p.e.. At 2 p.e. it is reduced to a few Hz.

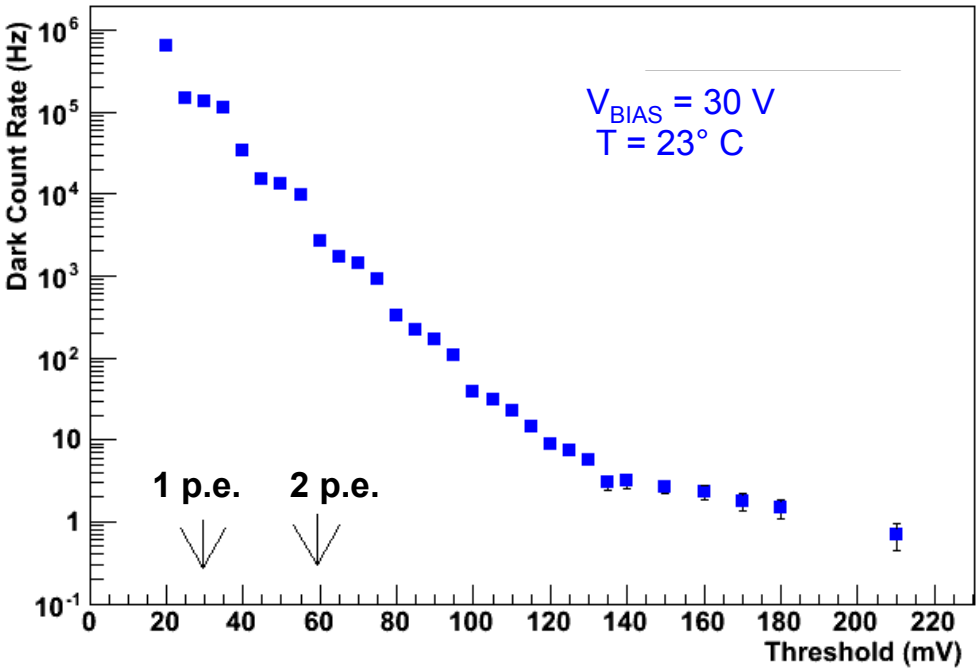

Figure 4.25 - SiPM dark rate @ V_{bias} =30V.

Subsequently, a plastic scintillator such as the one in Figure 4.5 (sensitive area 12x12x1 cm^3) was placed 4.5 cm above the module surface, 125 cm far from the SiPM. The rate of cosmic rays coincidences between SiPM and scintillator signals, in function of the set threshold was acquired, keeping V_{bias} = 30 V. In order to find the best configuration in terms of threshold and V_{bias}, the measurement was repeated at V_{bias} = 31 V. The related results are reported in the two plots of Figure 4.26.

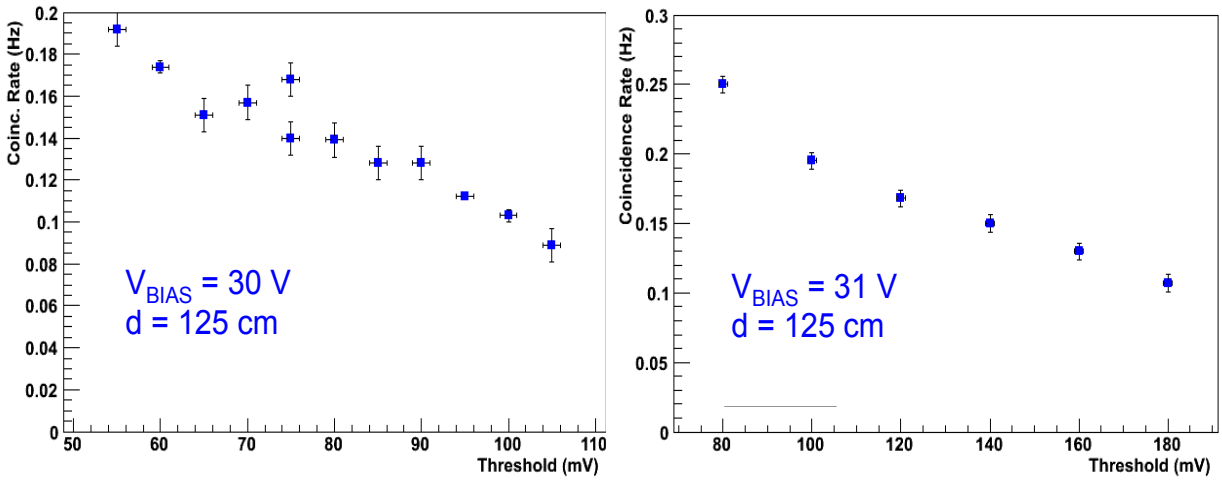

Figure 4.26 - Coincidence rate of a plastic scintillator and the module under test as a function of the SiPM threshold with supply voltage V_{bias} = 30 V (left) and V_{bias} = 31 V (right).

At the same V_{bias} = 31 V, the plot in Figure 4.27 was obtained. As it is clearly visible, the rate is quite uniform in the whole strip.

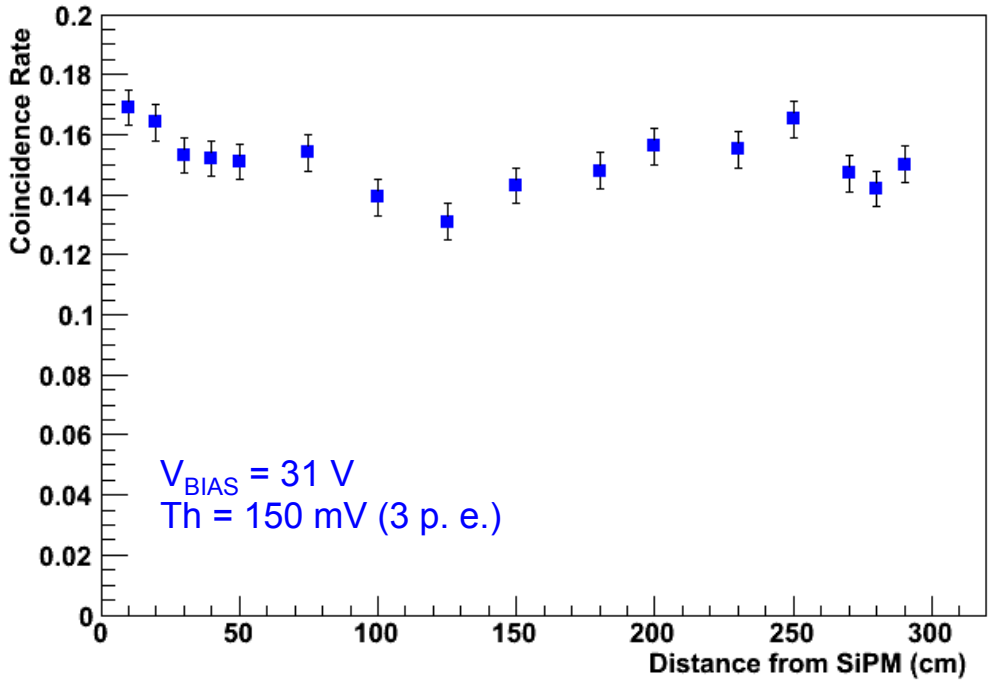

Figure 4.27 - Coincidence rate as a function of the distance from the SiPM at V_{bias} = 31 V for the strip number 17 of the tested module,

Additional measurements were also conducted at V_{bias} = 29.5 V, but after the evaluation of the overall results, the best solution seems to be V_{bias} = 30 V.

Hence, setting V_{bias} = 30 V, several measurements were performed, some of which are still on-going tests.

CONCLUSIONS

The work presented in this PhD thesis aims to show as technological advances and suitable technical solutions make *large-area, highly segmented trackers* of charged particles capable of being applied in two different research areas both of great importance for improving the quality of human life:

(1) **Medical diagnostics**, in particular before or during a tumour treatment with hadrons (hadrontherapy);

(2) **Tomography by cosmic ray radiation** (muon tomography) applied to cargo containers for the identification and localization of potential radioactive substances that are illegally transported.

In *medical physics,* these trackers can be applied as follows:

- Monitoring and imaging of a clinical beam;
- Positioning of a patient before a hadrontherapy treatment;
- Radiography and tomography of human tissues.

The advantage of exploiting charged particles such as proton or carbon ions for a cancer treatment is related to a better control of the amount of released dose compared to conventional radiotherapy without adversely affecting the surrounding healthy organs and tissues. Furthermore, the direct knowledge of the energy loss by a particle that interacts with the tissue, provides much more accurate information than the x-ray tomography, on the delivered dose and also allows to check the correct positioning of the patient. Starting from these considerations, the necessity to have a particle tracker able to provide real-time images of the area to be treated is clear.

For this reason the *OFFSET* Research Project started in the year 2010 with the aim to realize a detector made of *water equivalent material* for the real-time imaging and tracking of charged particles with high spatial resolution and low complexity to be applied in medical diagnostic.

The first prototype of the *OFFSET* tracker was designed with a single X-Y position plane having a sensitive area 20x20 cm^2. It has the great advantage of a read-out channel reduction system applied to a large-area detector with a high spatial resolution, employing sub-millimeter Sci-Fis and an appropriate functional architecture. A complete characterization was carried out and the results have been presented.

Subsequently a new version of the detector, the *OFFSET3* tracker, having two X-Y position planes was constructed in order to reduce the overall size and to improve imaging performances being able to acquire charged particles tracks and by extending the *field of view* to 28.8x28.8 cm^2. *OFFSET3* has the additional advantage of using the reduction channel technique combined with the Time Over Threshold analysis to reduce the number of read-out channels and the ribbons to be employed for the X-Y planes.

The tracker has the following specifications:

- 500 μm/$\sqrt{12}$ spatial resolution, calculated as for a segmented detector;
- About 1 ns time resolution;
- 2 mm water equivalent thickness;
- 5 MHz maximum acquisition rate;
- Real-time acquisition, processing and visualization.

The main results regarding the systems architecture have been used to demonstrate the technique, which has been patented by the Italian National Institute of Nuclear Physics (INFN) [97].

Both detectors were tested with cosmic rays, beta sources, 62 MeV proton beam at the LNS-INFN. In addition, the *OFFSET3* tracker was tested with 226 MeV proton beams and 400 MeV/A carbon beams at the CNAO hadrontherapy center. Complete characterizations were carried out and the results were presented.

A new front-end board is now under development allowing the individual regulation of thresholds for all comparators.

The use of Silicon photomultiplier replacing a multi-anode Position Sensitive Photo-Multiplier (PSPM) array is also under consideration.

The *OFFSET3* Tracker has currently been used for particle beam monitoring at the LNS-INFN.

Future perspectives concern the application of *OFFSET3* as particle tracker in the PREDATE project [98]. The *PREDATE (Particle Residual Energy And Tracker Enhancement)* project is aimed at developing a *real-time particle radiography system*, whose building blocks are two *OFFSET3* trackers and a *Residual Range Detector* (RRD) described in Appendix. The scheme of the apparatus is reported in Figure 1.

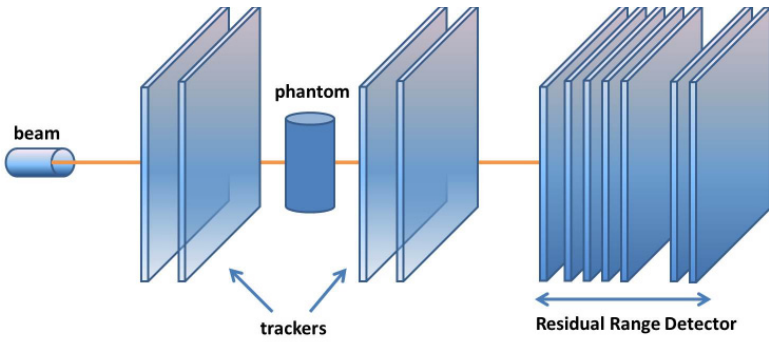

Figure 1 - Particle Radiography system which main blocks are two *OFFSET3* trackers and a Residual Range detector (RRD) [98].

This system will take advantages of large detection area (up to 30x30 cm^2), suitable for many medical physics applications, high spatial resolution (up to

approximately 100 μm rms) and time resolution (up to 1.5 ns rms), high energy resolution (about 0,7 % for 250 MeV protons) mainly employing scintillating optical fibers for the trackers and for the residual range measurement, suitably coupled to appropriate photo-sensors. Moreover, it will be a water equivalent detector with real-time acquisition performances.

GEANT4 simulations were conducted in order to reconstruct a radiographic image obtained by using the proposed radiography system.

A 4.7x4.7 cm^2 phantom in PVC divided into four areas of thickness 0.5 mm, 2 mm, 10 mm and 15 mm was considered in the simulation. The simulated radiography and its projections are shown in Figure 2 and Figure 3 respectively.

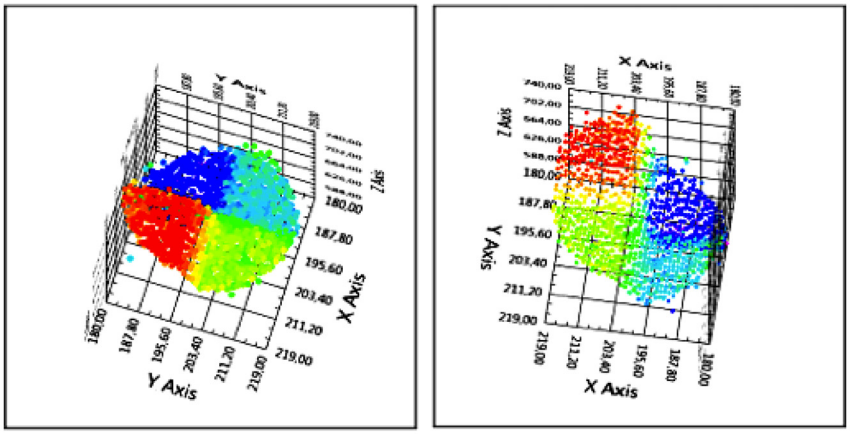

Figure 2 - Simulated radiographic images of a 4.7x4.7 cm^2 phantom in PVC, divided into four areas of thickness 0.5 mm, 2 mm, 10 mm and 15 mm.

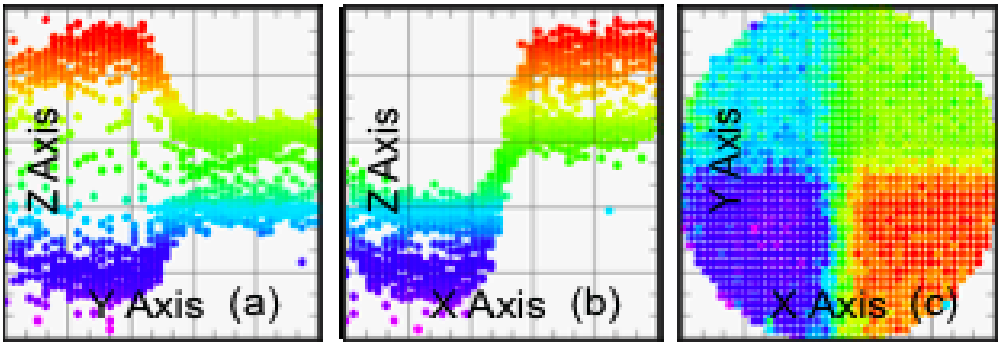

Figure 3 - Projections of the tomographic image obtained by GEANT4 simulation, on the three planes YZ (left), XZ (center) and XY (right) respectively.

The technological know-how acquired with the design, construction and characterization of the *OFFSET3* detector has been of great assistance for the construction of the *PORTAL detector* (sketched in Figure 4). The latter fits in the *muon tomography* for the safety transport of goods inside containers.

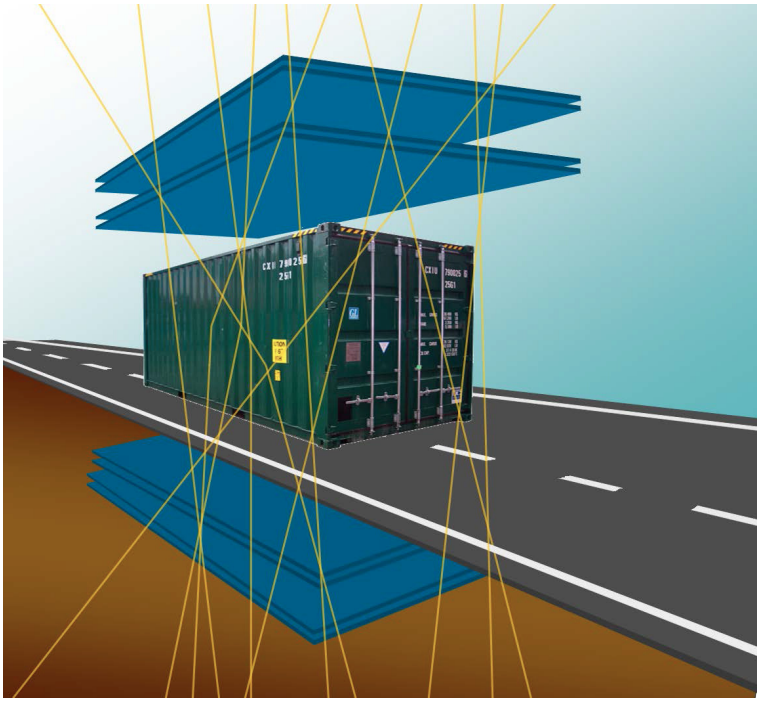

Figure 4 – Sketch of the *PORTAL* with a container between the inner tracking planes.

The detection principle is based on the determination of the scattering angle of each muon from cosmic ray radiation as a result of crossing a high-Z material (both nuclear material and high-Z shielding materials). Indeed, the angular deflection of the trajectory is very sensitive to the Z of the atomic nuclei. The scattering angle can be reconstructed by the incoming and outgoing tracks with respect to the scanned object.

Comparing the inspection techniques exploiting x-rays, γ-rays or other particle sources (neutron, ions) to muon tomography, the last presents some advantages as reported in the list below.

- Scan is not invasive. Not only the technique does not require opening the container, but also the cargo content is not damaged because muons are Minimum Ionizing Particles (MIP);
- Acquisition time required is of a few minutes for a complete 3D tomography, in contrast with the time required by x-ray radiography (about 60 s per a 2D slice, using the CT method);
- Muon radiation is a natural source so that it is not required to introduce an external source that could be dangerous for the environment and for the operators.

The second part of this thesis reports the results of work from the last two years on the *PORTAL detector*. The time was spent to define the technical details and choices connected with the construction phase. Evaluating tests and simulations

the following decisions were made on the final architecture.

- *PORTAL consists of eight 3x6 m^2 layers corresponding to four detection planes. In each layer there are six 1x3 m^2 identical modules, made of one hundred scintillating strips (10x10x3002 mm^3)* coated with reflective TiO_2. The modules have been constructed placing the strips between two 1 m wide aluminum sheets (1 mm thick) using 50 μm thick bi-adhesive film and aluminized Mylar.
- *The chosen strips* are the extruded *AMCRYS* (Kharkov, Ukraine) strips (10x10 mm^2 cross-section, 3 m long with 2 grooves along their surfaces). They *will be coupled to the Kuraray Y11 fibers* that have shown the best compromise in terms of light yield and costs;
- *Each strip is read by a double* circular *SiPM MUON60* by STMicroelectronics with a diameter of 1.5 mm. The SiPMs will be soldered on boards fixed to the cookies by STMicroelectronics. Ten of these boards are foreseen for each module. The SiPMs are currently being tested, individually, to classify them using their Breakdown Voltage.
- The ends of the module without the SiPM have been coated with aluminized Mylar;
- *The compression system is made by multiplexing the outputs of 10 SiPMs into groups*. *The multiplexed signals are amplified* in the front-end by THS3201 (1.8 GHz GBW). The front-end modules have a appropriate *temperature-controlled system*;
- *The discriminators outputs are sent to the acquisition system by suitable line drivers.* The acquisition system of a complete module, similar to that used for the described *OFFSET* detectors is currently being tested for a complete module;
- *Image reconstruction algorithms employing different methods are almost ready*.

Preliminary test results on different strips of a module are ready and additional tests on another module are in progress.

The first layer was already placed on the custom-designed mechanical support (an iron steel framework with a volume of 6x3x7 m^3).

In total, 20 modules were already assembled. The final large-scale prototype will be ready around mid-2015 and it will be used to inspect containers transiting in ports. Other future applications of the muon detector, such as in landfills and airports are also under study.

APPENDIX

The Residual Range detector (*RRD*), able to measure the energy delivered by a charged particle that crosses it, consists of a stack of closely-packed, optically-isolated scintillating layers coupled to a multi-anode photomultiplier and a read-out by a fast front-end module and high-speed DAQ boards. The sixty Polystyrene layers are 500 μm thick, with a sensitive area of 4x4 cm^2 and are separated by 4 mm air and enclosed in an aluminium frame for mechanical support. The detector is made of *water equivalent material*.

In each layer, there are ninety BCF-12 multi-clad square *Sci-Fis* and two *WLS* 1 mm size Kuraray Y11 fibers. A photo of the *RRD* including details on the *Sci-Fi* layer and *WLS* fibers is shown in Figure 5.

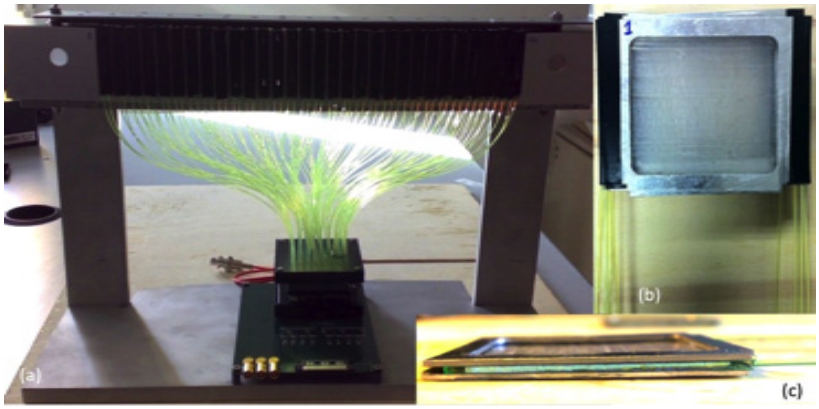

Figure 5 - Pictures of the residual range detector prototype (a), the Sci-Fi layer (b) and lateral view of a Sci-Fi layer with detail of the WLS fiber and Sci-Fi ribbon opto-mechanical coupling (c).

Each WLS fiber is coupled to a photocathode pixel of a Hamamatsu PSPM H8500. Starting from raw data, two different types of analyses were performed: Right-Most (RM) and Time Over Threshold (TOT). In the RM analysis, for each event the number of the deepest (compared to the beam line) layer turned on is stored and accumulated in a histogram. The RM layer corresponds, for each event, to the measured range of the particle, so it is correlated to Bragg peak.

In the TOT analysis, for each event the number of clock cycles for which the signal is over a suitable threshold is counted and stored for each channel. Since the light produced in a layer is proportional to the energy released by the particle in that layer, it is easy to understand that the information achieved with this analysis is the Bragg peak shape along the detector, particle by particle.

The front-end board is based on 64 channels of fast comparators, the MAX964 by Maxim-Dallas, followed by 100 ns monostables. The DAQ board is a National Instruments NI-5961 FLEX-RIO and a custom adapter module with 128 DIO at 200 MHz was designed. In order to have a real-time measure of the light produced in each

layer, proportional to the energy released by the crossing particle, to calculate the Bragg peak position, the right most layer and the time over threshold analyses are used (at a maximum rate of about 10 MHz).

A simulation campaign, employing the GEANT4 platform, was carried out in order to evaluate the performances of the prototype in terms of residual range resolution and to develop a calibration tool for the detector response. Each layer of the residual range detector is represented as a single plane of multi-cladding Sci-Fi. The entry energy of the proton beam was varied taking into account the use of the calibrated range shifters employed in the experimental setup at the LNS-CATANA facility (Table 1). The range was calculated as the depth at which the Bragg curve is 10% compared to the Bragg peak amplitude. For all the energies of interest agreement occurs within a tenth of a millimeter.

Range shifter	Range in Polyst. (mm)	RRD Layer with RM analisys (layer number)	RRD Layer with TOT analisys (layer number)
	27.7	55.4	53.78
A5	22	48.6	47.97
A10	17.3	38.2	38.06
A15	11.8	29.3	28.28
A20	6.1	19.6	18.94
A22	5.7	Not measured	Not measured
A20+ A5	3	7.5	5.61

Table 1 - The average values of the RRD layer number by Gaussian distributions, experimentally measured with the RM and TOT analysis, are indicated for each range shifter employed.

For range shifter employed with the 62 MeV proton beam, the input kinetic energies into the residual range prototype were calculated by means of GEANT4 and plotted in Figure 6 as a function of the simulated and experimental RM values (obtained by the *RRD*), which are also reported in Table 1.

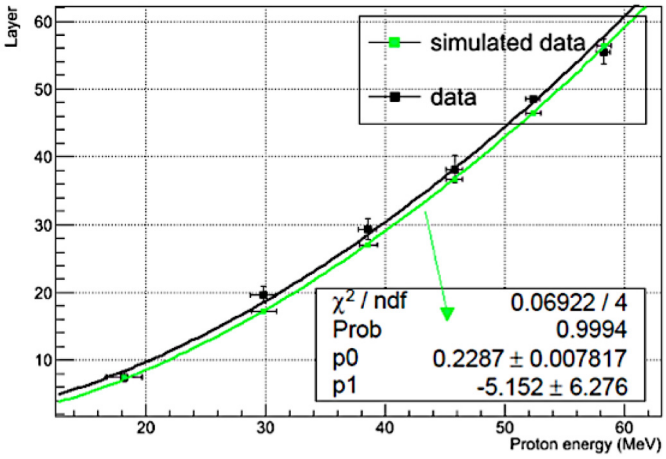

Figure 6 - Experimental (black points) and simulated (green points) RM values as a function of the residual range entrance kinetic energy. Also the experimental (red points) TOT values are included.

The data were fitted with the following relationship, with an exponential factor of the kinetic energy of 1.75: $R = p_1 + p_0 T^{1.75}$.

A good agreement of the two curves is clearly visible. The energetic resolution is $< 3\%$ at full range.

ACKNOWLEDGMENTS

The *OFFSET* project started in year 2010 is funded by the INFN National Scientific Committee V (technological and inter-disciplinary research).

The Muon Portal project (2011-2015) [99] is founded by National Operative Programme (PON) for Research and Competitiveness [100].

The partners of the Muon Portal Collaboration are:

- Dep. of Physics & Astronomy, University of Catania
- INAF – Astrophysical Observatory of Catania
- STMicroelectronics S.r.l. Catania
- Meridionale Impianti Welding Technology
- Insirio SPA

A special thanks to my research group, which has greatly contributed to my education during these three years of PhD.

REFERENCES

[1] R. K. Bock, The Particle Detector BriefBook, English language, Springer (2010).

[2] G. F. Knoll, Radiation Detection and Measurement. John Wiley & Sons Inc; 4 edition (2010) English language.

[3] W. Blum et al,, Particle Detection with Drift Chambers, 2008 Springer-Verlag Berlin Heidelberg.

[4] The Pierre Auger Collaboration, Atmospheric effects on extensive air showers observed with the surface detector of the Pierre Auger observatory, Astroparticle Physics, Volume 32, Issue 2, September 2009, Pages 89-99.

[5] M. Descovich, Improving the position resolution of Highly Segmented HPGe detectors using pulse shape analysis methods, Thesis at the University of Liverpool, Oliver Lodge Laboratory, 2002.

[6] D. Lo Presti et al., "OFFSET: Optical Fiber Folded Scintillating Extended Tracker", 2014 Nucl. Instr. and Meth. A 737 (2014) 195-202.

[7] Istituto Nazionale di Fisica Nucleare (Italian name) http://www.infn.it.

[8] I. B. Berlman, Handbook of fluorescence spectra of aromatic molecules. Academic Press-New York and London, 1971.

[9] M. Perani, STUDIO DI FOTOMOLTIPLICATORI AL SILICIO (SiPM), 2008-2009, Alma Mater Studiorum · Università di Bologna.

[10] R. Ruchti, Tracking with scintillating fibers. Nucl. Instr. and Meth. B (Proc. Suppl.), 44:308.319, 1995.

[11] Kuraray factory website: http://kuraraypsf.jp/psf/.

[12] F. Longhitano, OFFSET: NUOVO RIVELATORE DI PARTICELLE BASATO SU FIBRE OTTICHE SCINTILLANTI, Degree Thesis, University of Catania, 2009/10.

[13] L. Neri et al., Design and characterization of single photon avalanche diodes arrays, Nucl. Instr. and Meth. A Volume 617, Issues 1–3, 11–21 May 2010, Pages 432–433.

[14] A. Vacheretc, Characterization and simulation of the response of Multi-Pixel Photon Counters to low light levels, Nucl. Instr. and Meth. A, Volume 656, Issue 1, 11 November 2011, Pages 69–83.

[15] Chernov et al., 1993; James, 1983.

[16] D. Lo Presti et al., Design and characterization of a real time, large-area, high spatial resolution particle tracker based on scintillating fibers, Biomedical Engineering Research; 2 (4): 159-174. DOI: 10.5963/BER0204002, 2013.

[17] Laboratori Nazionali del Sud (Italian name) website: http://www.lns.infn.it.

[18] Centro Nazionale di Adronterapia Oncologica (Italian name) website: http://www.cnao.it/index.php/en/.

[19] Saint Gobain Crystals - Scintillating optical fibers brochure: http://www.detectors.saint-gobain.com.

[20] K.Lang for the MINOS Collaboration, Nucl. Instr. and Meth. A 461 (2001) 290–292.

[21] A.Gomes et al., Nuclear Physics B (Proc. Suppl.) 61B (1998), 106-111.

[22] D. Lo Presti et al., Characterization technique of sub-millimeter scintillating fibers. IEEE Nuclear Science Symposium/Medical Imaging Conference (NSS/MIC)/18th International Workshop on

Room-Temperature Semiconductor X-Ray and Gamma-Ray Detectors, Valencia, Spain, Oct. 23{29, 2011.

[23] Hamamatsu web page: www.hamamatsu.com.

[24] Maxim-Dallas web page: www.maximintegrated.com/.

[25] D. Lo Presti, L. Caponetto, N. Randazzo (2009). Low power multi-dynamics front-end architecture for the optical module of a neutrino underwater telescope. Nuclear Instruments and Methods in Physics Research A Vol. 602, pp. 126{128, doi:10.1016/j.nima.2008.12.029.

[26] National Instruments web page: www.national.com.

[27] LabVIEW website: http://www.ni.com/labview/i/.

[28] Son V. Cao et al., Cosmic Ray Veto for Water Cherenkov Detectors with Shallow Overburdens, University of Texas at Austin, full document: http://www-hep.physics.wm.edu/~vahle/enumi/may2013/CHIPS-CR-rate-v1.pdf.

[29] EBT gafchromic film website: www.harpell.ca/manufacturer/isp/gafchromic-ebt.

[30] MUON PORTAL Collaboration, F. Riggi et al., The Muon Portal Project: Development of an Innovative Scanning Portal Based on Muon Tomography, proceedings of the ANIMMA 2013 conference, Marseille, 23–27 June, 2013.

[31] K.R. Borozdin, Radiographic imaging with cosmic ray muons, Nature 422 (2003) 277.

[32] W. Priedhorsky et al., Detection of high-Z objects using multiple scattering of cosmic ray muons, Rev. Sci. Instrum. 74 (2003) 4294.

[33] K. Gnanvo et al., Imaging of High-Z Material for Nuclear Contraband Detection with a Minimal Prototype of a Muon Tomography Station Based on GEM Detectors, Nucl. Instrum. Meth. A 652 (2011) 16. – 9 –2014 JINST 9 C05029.

[34] S. Pesente et al., First results on material identification and imaging.

[35] Y. Liu et al., Comparison of neutron and high-energy X-ray dual-beam radiography for air cargo inspection, Applied Radiation and Isotopes 66 (2008) 463–473.

[36] E.T.Wrigh, A Detector for Muon Tomography: Data Acquisition and Preliminary Results, 2007.

[37] Encyclopedia BRITANNICA, Web page: http://www.britannica.com/EBchecked/topic/139234/cosmic-ray/302389/Electrons-in-cosmic-rays.

[38] A. M. Hillas, The cosmic-ray knee and ensuing spectrum seen as a consequence of Bell's self-magnetized SNR shock acceleration process, Journal of Physics: Conference Series Volume 47, 2006 J. Phys.: Conf. Ser. 47 168 doi:10.1088/1742-6596/47/1/021.

[39] P. Auger experiment website: http://www.auger.org.

[40] Hires experiment website: http://hires.physics.utah.edu.

[41] AGASA experiment website: http://www-akeno.icrr.u-tokyo.ac.jp/AGASA/.

[42] A.D. Erlykin, Structures in the cosmic ray energy spectra, Astroparticle Physics
Volumes 50–52, December 2013, Pages 47–50.

[43] P. Auger Collaboration, Measurement of the energy spectrum of cosmic rays above 10^{18} eV using the Pierre Auger Observatory, Elsevier, Physics Letters B, Volume 685, Issues 4–5, 8 March 2010, Pages 239–246.

[44] Tibet experiment web page: http://www.icrr.u-tokyo.ac.jp/em.

[45] M. Nagano et al., Search for the end of the energy spectrum of primary cosmic rays, New J. Phys. 11 (2009) 065012, doi:10.1088/1367-2630/11/6/065012.

[46] R. Aloisio et al., Transition from galactic to extragalactic cosmic rays, Astropart. Phys. 39-40 (2012) 129-143, DOI:10.1016/j.astropartphys.2012.09.007.

[47] "Red Chair blogs" web page: http://www.redchairblogs.com/starstruck/2013/06/14/is-interplanetary-space-too-hot-for-humans/.

[48] W.M. Yao, et al. Particle Data Group Review of Cosmic Rays Journal of Physics G33, 1. 2006.

[49] L.W. Alvarez, et al, Search for Hidden Chambers in the Pyramids Using Cosmic Rays, Science 167 (1970) 832.

[50] The Maya Muon Group A Detector for Muon Tomography Conceptual Design Report, June 2004.

[51] http://pdg.lbl.gov/2014/AtomicNuclearProperties/adndt.pdf.

[52] W.B. Gilboy et al., Muon radiography of large industrial structures, Nuclear Instruments and Methods in Physics Research B 263 (2007) 317–319.

[53] K. Gnanvo, Imaging of high-Z material for nuclear contraband detection with a minimal prototype of amount tomography station based on GEM detectors, Nuclear InstrumentsandMethodsinPhysicsResearchA652 (2011) 16–20.

[54] D.F. Mahon, A prototype scintillating-fibre tracker for the cosmic-ray muon tomography of legacy nuclear waste containers, Nuclear Instruments and Methods in Physics Research A 732 (2013) 408–41 & G. Jonkmans, Nuclear waste imaging and spent fuel verification by muon tomography, Annals of Nuclear Energy 53 (2013) 267–273.

[55] http://pheloniusfriar.dreamwidth.org/15339.html?thread=8427&style=light.

[56] Webpage: http://www.ridgeglobal.com/news/view/luke-ritter-discusses-the-latest-breakthrough-in-cargo-scanning-technology.

[57] http://pheloniusfriar.dreamwidth.org/15339.html.

[58] Xinhui Duan, X-ray cargo container inspection system with few-view projection imaging, Nuclear Instruments and Methods in Physics Research A 598(2009) 439–444.

[59] F.Y.Hsu, Ambient and personal dose assessment of a container inspection site using a mobile X-ray system, Applied Radiation and Isotopes 70(2012)456–461.

[60] Overview of Exploranium's AT-980 Radiation Portal Monitor (RPM). Retrieved Sep 2007.

[61] Wald, M. (November 22, 2009). "Shortage Slows a Program to Detect Nuclear Bombs", New York Times.

[62] Y. Liu, Comparison of neutron and high-energy X-ray dual beam radiography for air cargo inspection, Applied Radiation and Isotopes 66 (2008) 463–473.

[63] Maya Muon Group: http://www.hep.utexas.edu/mayamuon/about.html.

[64] J. Marteau et al., Muons tomography applied to geosciences and volcanology, Nuclear Instruments and Methods in Physics Research A 695(2012) 23–28.

[65] K.Nagamine, Journal of Geography 104(1995)998.

[66] H.K.M.Tanaka,K.Nagamine,N.Kawamura, S.N.Nakamura, K.Ishida, K. Shimomura, HyperfineInteractions 138 (2001) 521.

[67] H.K.M.Tanaka, K.Nagamine, N.Kawamura, S.N.Nakamura, K.Ishida, K. Shimomura, NuclearInstrumentsand Methods in Physics Research, Section A 507 (2003) 657.

[68] H.K.M. Tanaka e t al., Radiographic measurements of the internal structure of Mt. West Iwate with near-horizontal cosmic-ray muons and future developments, Nuclear Instruments and Methods in Physics Research A 555 (2005) 164–172.

[69] H.K.M. Tanaka e t al., Development of an emulsion imaging system for cosmic-ray muon radiography to explore the internal structure of a volcano, Mt. Asama, Nuclear Instruments and Methods in Physics Research A 575 (2007) 489–497.

[70] K. Nagamine et al., Method of probing inner-structure of geophysical substance with the horizontal cosmic-ray muons and possible application to volcanic eruption prediction, Nuclear Instruments and Methods in Physics Research A 3.56 (1995) 585-595.

[71] E.V.Bugaev, YuD.Kotov, I.L.Rosental, Cosmic Muons and Neutrinos, Atomizdat, Moscow.

[72] G. Ambrosi et al., The MU-RAY project: Volcano radiography with cosmic-ray muons, Nuclear Instruments and Methods in Physics Research A 628 (2011) 120–123.

[73] Wikipedia web page: http://en.wikipedia.org/wiki/Muon_tomography.

[74] Project Report on "Monitoring Carbon Capture in Deep Rock using Muon Tomography", (2011), web page: http://e-futures.group.shef.ac.uk/publications/pdf/99_4.%20Cora%20Fung%20summary.pdf.

[75] M. Bandieramonte, et al., Automated object recognition and visualization techniques for muon tomography data analysis. In Technologies for Homeland Security (HST), 2013 IEEE International Conference on, pages 517-522. IEEE, 2013.

[76] M. Tsutsumi, LaCl3(Ce) scintillation detector applications for environmental gamma-ray measurements of low to high dose rates , NIMA, Volume 557, Issue 2, 15 February 2006, Pages 554–560.

[77] V. Sipala et al., A proton Computed Tomography system for medical applications,
14th International Workshop on Radiation Imaging Detectors (IWORID2012), Figueira da Fox, Portugal, 1-5 July 2012. Journal of Instrumentation (JINST) 8 C02021, doi:10.1088/1748-0221/8/02/C02021 2013.

[78] Website on scintillator detectors: http://www.johncaunt.com/detectors/scintillation-detectors/applications-general-properties/.

[79] F. Riggi et al., (The Muon Portal Collaboration), Proceedings of the ANIMMA 2013 Conference, Marseille, 23-27 June, 2013.

[80] S. Agostinelli et al., Geant4—a simulation toolkit, Nuclear Instruments and Methods in Physics Research A 506 (2003) 250–303.

[81] Fermilab Nat. Lab, Batavi, Ill, USA.

[82] Uniplast Factory, Vladimir, Ul, Grande Tverskaya, 77, Russia.

[83] Bicron Corp., 12345 Kinsman Road, Newbury, Ohio 44065, U.S.A.

[84] Kuraray Co., Methacrylic Resin Division, 8F, Maruzen Building, 3–10, 2-Chrome, Hihonbashi, Chuo-ku, Tokyo, 103-0027, Japan.

[85] G.V. Russo et al., Strip Detectors for a Portal Monitor Application, Journal of Instrumentation (JINST) 9 P11008 doi:10.1088/1748-0221/9/11/P11008, November 2014.

[86] C. Pugliatti for the Muon Portal Collaboration, Design of a muonic tomographic detector to scan travelling containers, Part of 15th International Workshop on Radiation Imaging Detectors

(IWORID2013), Paris (France), Journal of Instrumentation (JINST) 9 C05029 doi:10.1088/1748-0221/9/05/C05029, 2014.

[87] OPERA experiment website: http://operaweb.lngs.infn.it/?lang=en.

[88] OPERA target tracker website: http://sbgopera.in2p3.fr/general/TDR/target_tracker.htm.

[89] B. C. Choudhary, NuMI-l-306, October 15, 1997.

[90] STMicroelectronics in Catania: http://www.st.com/web/en/about_st/careers/catania.html.

[91] ADAM-4571 Serial Device Servers User Manual: http://www.bb-elec.com/Products/Manuals/ADAM-4570_4571_Manual_Ed2.pdf.

[92] S. Riggi et al., (The Muon Portal Collaboration), Nuclear Instruments and Methods A 624 (2010) 583-590.

[93] S. Riggi et al., (The Muon Portal Collaboration), Proceedings of the ECRS 2012 Conference, Moscow, 3-7 July, 2012, J.Phys.G(Conf.Series)409(2012)012046.

[94] COsmic Ray SImulations for KAscade (CORSIKA) simulation code web page: https://web.ikp.kit.edu/corsika.

[95] F. Riggi et al., (The Muon Portal Collaboration), Proceedings of the ANIMMA 2013 Conference, Marseille, 23-27 June, 2013.

[96] S. Riggi et al., Muon tomography imaging algorithms for nuclear threat detection inside large volume containers with the Muon Portal detector, Nuclear Instruments and Methods A, DOI: 10.1016/j.nima.2013.06.040, 2013.

[97] Lo Presti D., INFN, patent n. WO2013186798 “Detector based on scintillating optical fibers for charged particle tracking with application in the realization of a residual range detector employing a read-out channels reduction and compression method”.

[98] D. Lo Presti et al., A real-time, large-area, high space resolution particle radiography system, Journal of Instrumentation (JINST) 9 C06012 doi:10.1088/1748-0221/9/06/C06012, 2014.

[99] Muon Portal project website: http://muoni.oact.inaf.it:8080.

[100] National Operative Programme (PON) Italian website: http://www.ponrec.it.

PUBLICATIONS

This PhD thesis is supported by the following publications:

- V. Sipala et al.

A proton Computed Tomography system for medical applications
14th International Workshop on Radiation Imaging Detectors (IWORID2012), Figueira da Fox, Portugal, 1-5 July 2012 Journal of Instrumentation (JINST) 8 C02021, doi:10.1088/1748-0221/8/02/C02021 2013.

- Pugliatti for the Muon Portal Collaboration

Elettronica di read-out per il portale muonico
Conference Record "XCVIII Congresso Nazionale della Società Italiana di Fisica (SIF)", Napoli, September 2012.

- Pugliatti et al.

Smart read-out di un calorimetro a cristalli scintillanti
Conference Record "XCVIII Congresso Nazionale SIF", Napoli, September 2012.

- S. Riggi et al.

A large-area cosmic ray detector for the inspection of hidden high-Z materials inside containers
Conf. Series J. Phys.: Conf. Ser. 409 012046, doi:10.1088/1742-6596/409/1/012046 2013.

- M. Bruzzi for the PRIMA (Proton IMAging) collaboration

Status of the development of a proton Computed Tomography Scanner (Conference Paper)
Nuclear Science Symposium and Medical Imaging Conference (NSS/MIC), 2012 IEEE.
2012, Article number 6551983, Pages 4314-4317
Anaheim, CA; United States; 10.1109/NSSMIC.2012.6551983, 2012.

- Vanzi the PRIMA collaboration

Preliminary results in FBP reconstruction of pCT data
Nuclear Instruments and Methods in Physics Research, Section A: Accelerators, Spectrometers, Detectors and Associated Equipment, DOI: 10.1016/j.nima.2013.05.193, 2013.

- Civinini for the PRIMA collaboration

Recent results on the development of a proton computed tomography system
Nuclear Instruments and Methods in Physics Research, Section A: Accelerators, Spectrometers, Detectors and Associated Equipment, DOI: 10.1016/j.nima.2013.05.147, 2013.

- Lo Presti et al.

A real-time, large-area, high spatial resolution tracker based on square scintillating fibers (Conference Paper)
Nuclear Science Symposium and Medical Imaging Conference (NSS/MIC), 2012 IEEE
2012, Article number 6551305, Pages 1244-1249
Anaheim, CA; United States; 10.1109/NSSMIC.2012.6551305, 2012.

- M. Scaringella for the PRIMA collaboration

The PRIMA (PRoton IMAging) collaboration: Development of a proton Computed Tomography apparatus
Nuclear Instruments and Methods in Physics Research, Section A: Accelerators, Spectrometers, Detectors and Associated Equipment, DOI: 10.1016/j.nima.2013.05.181, 2013.

- Civinini for the PRIMA collaboration

Development of a Proton Computed Tomography system for pre-clinical tests (Conference Paper)
Nuclear Science Symposium and Medical Imaging Conference (NSS/MIC), 2012 IEEE
Article number 6551313, Pages 1279-1283
Anaheim, CA; United States; 10.1109/NSSMIC.2012.6551313, 2012.

- Lo Presti et al.

Development of a scintillation-fiber detector for real-time particle tracking
Journal of Instrumentation (JINST); 8. DOI:http://dx.doi.org/10.1088/1748-0221/8/04/P04015, April 2013.

- F. Longhitano for the Muon Portal Collaboration

Test degli elementi base dei moduli di tracciamento per la realizzazione dei piani di rivelazione del Progetto "Muon Portal"
Conference Record "XCIX Congresso Nazionale SIF", Trieste 2013.

- M. Bandieramonte for the Muon Portal Collaboration

Tomographic images elaboration, visualization and monitoring system for the "Muon Portal" project
Conference Record "XCIX Congresso Nazionale SIF", Trieste 2013.

- V. Antonuccio for The Muon Portal Collaboration

The Muon Portal Project: Development of an Innovative Scanning Portal Based on Muon Tomography
Advancements in Nuclear Instrumentation Measurement Methods and their Applications (ANIMMA) Conference, Marseille (France), 10.1109/ANIMMA.2013.6727927, June 2013.

- Pugliatti for the Muon Portal Collaboration

Design of a muonic tomographic detector to scan travelling containers
Part of 15th International Workshop on Radiation Imaging Detectors (IWORID2013), Paris (France), Journal of Instrumentation (JINST) 9 C05029 doi:10.1088/1748-0221/9/05/C05029, 2014.

- Lo Presti et al.

A real-time, large-area, high space resolution particle radiography system
Part of 15th International Workshop on Radiation Imaging Detectors (IWORID2013), Paris (France), Journal of Instrumentation (JINST) 9 C06012 doi:10.1088/1748-0221/9/06/C06012, 2014.

- M. Bandieramonte for the Muon Portal Collaboration

Muon tomography: tracks reconstruction and visualization techniques
Il Nuovo Cimento C36, DOI: 10.1393/ncc/i2013-11553-y, 2013.

- Vanzi et al.

The PRIMA collaboration: Preliminary results in FBP reconstruction of pCT data
Nuclear Instruments and Methods in Physics Research Section A Accelerators Spectrometers Detectors and Associated Equipment; DOI: 10.1016/j.nima.2013.05.193, 2013.

- V. Antonuccio for the Muon Portal Collaboration

Design of a large-area tomograph to search for high-Z materials inside containers by cosmic muons
Nuclear Science Symposium and Medical Imaging Conference (NSS/MIC), 2012 IEEE
Anaheim, CA; United States; 10.1109/NSSMIC.2012.6551049, 2012.

- Leonora et al.

Noise Pulses in Large-area Optical Modules
Transactions on Nuclear Science (TNS)

Volume: 61, Issue: 4, Part: 2, Page(s): 2097 – 2104, DOI: 10.1109/TNS.2014.2322655, 2014.

- Lo Presti et al.

Development of a real-time, large-area, high spatial resolution particle tracker based on scintillating fibers
Hindawi Publishing Corporation, Advances in High Energy Physics, Volume 2014, Article ID 692908, http://dx.doi.org/10.1155/2014/692908, 2014.

- Lo Presti et al.

OFFSET: Optical Fiber Folded Scintillating Extended Tracker
Nuclear Instruments and Methods in Physics Research A; 737:195-202; DOI: 10.1016/j.nima.2013.11.049, January 2014.

- Lo Presti et al.

Design and characterization of a real time, large-area, high spatial resolution particle tracker based on scintillating fibers
Biomedical Engineering Research; 2(4):159-174. DOI: 10.5963/BER0204002, 2013.

- First Level degree thesis

Studio per la realizzazione di una radiografia con protoni in tempo reale
Author name: Giada Petringa
Supervisor: Domenico Lo Presti; Assistant supervisor: Cristina Pugliatti, 2013.

- First Level degree thesis

OFFSET3: Tracciatore in tempo reale di particelle basato su fibre ottiche scintillanti
Author name: Giulia Serio
Supervisor: Domenico Lo Presti; Assistant supervisor: Cristina Pugliatti, 2014.

- T. Chiarusi et al.

Status and first results of the NEMO Phase-2 tower
Journal of Instrumentation (JINST); 9:C03045. DOI: 10.1088/1748-0221/9/03/C03045, 2014.

- P. La Rocca et al.

Fabrication, characterization and testing of silicon photomultipliers for the Muon Portal Project
International Conference on New Developments in Photodetection Tours, France, June 30th to July 4th 2014 (in press for Nuclear Instruments and Methods in Physics Research A).

- G.V. Russo et al.

Strip Detectors for a Portal Monitor Application
Journal of Instrumentation (JINST) 9 P11008 doi:10.1088/1748-0221/9/11/P11008, November 2014.